Diagnostics and modelling of an inductively coupled RF low-pressure low-temperature plasma

Thesis

Diagnostics and Modelling of an Inductively Coupled RF Low-Pressure Low-temperature Plasma

A Thesis Submitted for the Degree of Doctor of Philosophy

by

Suidong Yang, BSc, MSc

The Physical Materials Group

Oxford Research Unit

The Open University

February, 1998

This thesis is dedicated to my mother-in-law in the eternal world, my wife, Liqun and six-years-old son, Dingji in United Kingdom, and our families, friends in China.

ACKNOWLEDGMENTS

I would particularly like to acknowledge the help and encouragement of my supervisor Dr. N St J Braithwaite, who always is holding a bright torch in front of me, when I drop in to darkness of life and scientific research.

Thanks also go to Dr Fred Haas and other members of the physical material group for many interesting and helpful discussions, since I came to this unit in 1992.

Moreover, I could not express my thanks enough for the help from technician Mr Ted Beaver, Mr Alan Knight, unit secretary Mrs Vivian Reynolds, and other people on the unit namelist, who made my time at this research unit so enjoyable in the past 6 years.

I should also thank Mr V S Law of the Cambridge Fluid Systems, for providing a stage to let me practise plasma diagnostics skills.

Dr S G Ingram formerly of the GEC Hirst Research Centre should be also mentioned here for his kind and valuable discussions in the design of the retarding energy analyser used in this work.

Finally, I acknowledge Mr Charles Mahoney, now at the Queens University of Belfast for his many private encouragments and wonderful introduction to the English life.

ABSTRACT

This thesis is a theoretical model and experimental study of the physics of a low pressure (5-50 mtorr), low electron temperature (1-10 eV), high density ($10^{17} - 10^{18} m^{-3}$) inductively coupled plasma. This type of plasma is similar to those much used in plasma etching, deposition, and other plasma aided materials processing of devices [1-5].

A two-dimensional, electromagnetic, finite-element model has been set up to simulate the operation of the inductively coupled plasma using the external coil configuration used in the experimental work. Given fixed external RF coil current and voltage and the measured plasma density profile, Maxwell's equations and magnetohydrodynamical (MHD) fluid equations are used to calculate the self-consistent electromagnetic field. A number of predictions are presented and compared with experiments.

A symmetric, cylindrical inductively coupled discharge system has been set up. A single turn loop magnetic probe has been used to measure electromagnetic (EM) field in the discharge chamber. A Langmuir double probe has been designed to measure the plasma density and electron temperature. An emissive probe was used to measure the time averaged plasma potential, while a capacitive probe was used to measure the RF component of the plasma potential. A retarding field energy analyser has been used to measure the total ion flux flowing to the vessel on the midplane. Experimental results show that (1) the inductively coupled plasma is well confined inside the induction coil in

the pressure range of 5-50 mtorr and RF power range of 10-400 W; (2) the measured electrostatic RF field (<1.0 V/cm) in the whole discharge chamber is negligible, compared with the large induction RF field, which is in the order of 10 V/cm; (3) the RF power is coupled into the discharge through the nonlinear electron motion and corresponding collision processes; (4) it has been shown that the induction-field-ionization, electrostatic-field-modulation and various collision processes together influence the velocity distribution function of ions at the boundary surfaces.

ABBREVIATIONS AND SYMBOLS

a the effective magnetic probe area

amu atomic mass unit

ADC analogue-to-digital converter

A the complex form of vetor potential

$\underline{A}$ electric vector potential

A_0 the boundary value of vector potential

B_0 amplitude of magnetic field

$\underline{B}$ magnetic field vector

c light speed

C_{wall} wall capacitance

C_{probe} capacitance of a capacitive probe

C_s plasma sheath capacitance near a probe tip

$c_{1,2,3}$ coefficients to determine ionization rate

$C_{1,2,3}$ capacitors in the matching unit

$\overline{C}_e$ averaged electron thermal speed

$\overline{C}_i$ averaged ion thermal speed

$\overline{C}_i$ the ion Bohm speed

CCP capacitively coupled plasma

dB decibel

DC direct current

e electron charge

$\underline{E}$ electric field vector

E_0 the amplitude of induction filed

EQP Hiden Mass/Energy analyser system

EVDF electron velocity distribution function

EEDF electron energy distribution function

EM electromagnetic field

ESA energy spectral analyser

E_{eff} the effective electron energy in a drift electron fluid in the ICP

f the electron velocity distribution function

FSD full scale division

F_i the ion velocity distribution funtion

$\underline{F}$ the Lorentz force on electron in EM field

G0, G1, G2 copper grids in a retarding energy analyser

ICP inductively coupled plasma

IEDFs ion energy distribution functions

IVDFs ion velocity distribution functions

I_i ion current collected by Langmuir probe tip

I_e electron current collected by Langmuir probe tip

I_0 the zeroth-order modified Bessel function of first kind

I_p plasma current

$\underline{J}$ the conduction current density vector

J_0 the zeroth order Bessel function of the first kind;

the poloidal electron drift velocity

J_1 the first order Bessel function of first kind

k Boltzmann's constant

K the amplitude of wave vector in vacuum

MHD magnetrohydrodynamics

m_e electron mass

m_i ion mass

n_0 the electron density where the effective electron energy equals zero

n_i ion density

n_e electron density

n_g neutral gas density; the density of collision parter

OES Optical emission spectrometer

p gas pressure

PMT photomultiplier tube

PIE plasma-induced emission

PGA programmable gain amplifier

P_t total RF power transferred into the RF coil

P_c power to create charged particles and excited particles in the plasma

P_d power dissipated in the plasma

P_{loss} power dissipated in the lossy inductor

$P_{optical}$ power of optical radiation

Q the effective electron collision cross section; the net charge on the wall

r_w the cylindrical chamber radius

RF radio frequency

RFI RF inductive plasmas

r radial position

R the scope impedance

S area of the Langmuir probe tip; radial component of the Poynting vetor

S_r the Poynting vetor in the radial direction

SOR successive-over-relaxation

t time

TCP transformed coupled plasmas

T_i ion temperature

T_e electron temperature

v electron velocity; ion velocity

u dimensionless ion drift velocity

V the RF electromotive force (emf) provided by the power supply;

DC voltage across Langmuir double probe tips

V_{er} electron radial drift speed

$V_{e\theta}$ electron poloidal drift speed

V_{RF} amplitude of RF voltage across Langmuir double probe tips

V_p the sheath potential difference (sometimes called plasma potential)

V_d electron drifting velocity

V_m minimum speed of electrons collected by a Langmuir probe

$\underline{V_e}$ electron drift velocity

V_{ir} ion radial drift velocity

V_{th} the averaged electron thermal speed, ie, $\overline{C_e}$

WFG waveform generator

x ion or electron

X normalized radial scale

Y_0 the zeroth order Bessel function of the second kind

z axial position

Z the complex impedance of electric equivalent circuit

Z_L the load impedance

Z_0 the RF source characteristic impedance

Z_0^* the conjugate of the characteristic impedance of the power supply

Z_m the matching unit impedance

Z_p the plasma impedance

ϕ electrostatic potential

ϕ_{DC} electrostatic DC potential

ϕ_p plasma potential

ϕ_w the amplitude of the wall potential

Φ_A the phase of vector potential

Φ_B the phase of magnetic field

Φ_E the phase of induction electric field

Υ_w the phase of the wall potential

v_i minimum speed of ions collected by a retarding energy analyser

Ω differential volume element

ω the RF angular frequency

ω_{pe} plasma electron oscillation frequency

ω_{pi} plasma ion oscillation frequency

μ_0 permeability in free space

ε the effective electron energy

ε_0 permittivity in free space

τ dimensionless time factor for ions

Γ particle flux flow to substrate; RF potential factor in probe I-V curves

λ_e electron mean-free-path

λ_D Debye length

υ_e the effective electron collision frequency

ν_{iz} ionization rate

σ plasma conductivity

ρ the space charge density

α, β constants from boundary conditions to determine the RF electrostatic potential

θ poloidal position

η dimensionless electron effective energy

$<E_r>$ the time averaged radial electrostatic ICP potential

$<S_r>$ the time averaged radial component of the Poynting vector in ICP

CONTENTS

Chaper 4 Modelling of an inductively coupled plasma

Chapter 5 Further considerations and conclusions

Appendices and references

Chapter 1 Introduction

1.1 Basic characteristics of plasma

The solid, liquid, and gaseous states of matter on earth are not typical of matter in the universe at large. Most matter in the universe occurs as a plasma that is an ionized gas. When neutral atoms or molecules are given enough energy by an external power source, such as a heater, an electromagnetic power supply, a photon source, or even an energetic particle beam, some of them will be ionized. In some cases this can be a thermodynamic equilibrium state but in most laboratory plasmas, equilibrium is not achieved.

The word plasma comes from the Greek, meaning "something molded". It was introduced by Tonks and Langmuir (1929), to describe the positive column region in a glowing ionized gas produced by an electric discharge. A plasma is a partially or fully ionized gas which is an assembly of charged particles (ions and electrons) and neutral atoms or molecules, interacting with each other through long range Coulomb forces and short range forces during elastic or inelastic collision processes.

The motion of plasma particles is governed by the above local interactions; meanwhile, the charged particles are also a source of electromagnetic fields. The properties of a plasma are therefore markedly dependent upon the particle-particle, particle-external-field interactions. To know what happens in different physical situations, one needs to find solutions which simultaneously satisfy the equations of particle motion and Maxwell's

equations. This leads to a self-consistent description of a plasma. The whole subject of plasma physics is a demonstration of the range and power of the following equations:

A set of Maxwell's equations

$$\nabla \times \underline{E} = -\frac{\partial}{\partial t}\underline{B} \tag{1.1}$$

$$\nabla \times \underline{B} = \mu_o \underline{J} + \mu_o \varepsilon_o \frac{\partial}{\partial t}\underline{E} \tag{1.2}$$

$$\nabla \bullet \underline{E} = \frac{\rho}{\varepsilon_o} \tag{1.3}$$

$$\nabla \bullet \underline{B} = 0 \tag{1.4}$$

where μ_0, ε_0 is the permeability and permittivity constant in free space, respectively. $\underline{B}$ is the magnetic field vector, $\underline{E}$ is the electric field vector, ρ is the net charge density, and $\underline{J}$ is the (electron) conduction current vector, which is defined for the electron component by

$$\underline{J} = -e\int_{-\infty}^{\infty} \underline{v} f d\underline{v} \tag{1.5}$$

where f is the number of electrons in the phase space of velocity v, position r, and time t. This is in turn determined through the Boltzmann equation for the evolution of the velocity distribution

$$\frac{\partial}{\partial t} f + \underline{v} \bullet \nabla f + \frac{\underline{F}}{m} \bullet \frac{\partial}{\partial \underline{v}} f = \left.\frac{df}{dt}\right|_{collisions} \tag{1.6}$$

where $\underline{F}$ is the force acting on the electron, which is equal to $-e(\underline{E} + \underline{v} \times \underline{B})$, the first term on LHS is the time rate of change of f, while the second one stands for the change of f

due to particle motion in space r, the third one represents external force influence on change of f, and the RHS of (1.6) stands for the time rate of change of f due to collisions (including source and sink terms). Ion motion is ignored in the above but it can be included through a parallel approach.

The set of equations describes the basic behaviour through which a plasma is able to exhibit fluid like properties, e.g. conforming with physical boundaries, and able to support waves and to flow. Some basic parameters in plasma physics and relevant to this thesis are listed as follows:

1.1.1 Particle density

Particle density is the number of particles per unit volume. The usual symbol is n_x where x implies a particular species, which could be i---ion, e---electron or n---neutral gas. In a glow discharge, only some fraction (typically 0.01-0.1%) of gas atom is ionizied. Note, in a spatially uniform plasma $n_i \approx n_e$, which implies there is no net charge in the bulk plasma, and therefore as it can be seen from equation (1.3), the derivative of local but macroscopic electric field tends to be zero, hence the electric field must tend to be a constant, which must be zero. This condition is termed plasma quasi-neutrality which is one of fundamental plasma properties. However, near a plasma boundary where $n_i \neq n_e$, owing to the presence of space charge, a large electromagnetic field is formed. It is in this region that ionization and other collision processes predominantly happen. There, electric charge carriers gain energy and transfer it to bulk plasma. On the other hand, energetic

particles are simultaneously driven (and eventually lost) to the boundary surface, after undergoing various elastic and inelastic collisions.

1.1.2 Particle temperature

Particle temperature is a measure of the averaged particle kinetic energy. It is defined by

$$T_x = \frac{2}{3}\frac{\langle E_x \rangle}{k} \tag{1.7}$$

where $\langle E_x \rangle$ represents the average particle kinetic energy. Strictly it should be restricted to isotropic components of energy. It is dependent on particle energy distributions (IEDF or EEDF for ions and electrons respectively) which will be addressed in section 1-2; k is Boltzmann' s constant, equal to $1.381 \times 10^{-23} J K^{-1}$. It is usual to express the particle temperature in units of electron volts: that is *kT/e*. Electrons are generally in near-thermal equilibrium at temperature T_e in discharge, whereas positive ions are almost never in thermal equilibrium. Neutral gas molecules may or may not be in the thermal equilibrium, depending on the generation and loss process. Typical electron temperatures in a glow discharge plasma are in the range of 1-10 eV, ion temperature and neutral gas temperature are relatively quite low, around 0.03 eV. However, the energy of ions bombarding the substrate can be as high as 10-1000 V in some circumstances, much exceeding T_e. This is due to the acceleration of low-temperature ions across plasma presheath and sheath region. The physics of the sheath is central to all the applications of plasma processing. We will describe this gradually later.

1.1.3 Debye length

The Debye length is a measure of the distance over which the influence of the electric field of an individual charged particle is felt by the other charged particles inside a plasma, and is given by

$$\lambda_D = \sqrt{\frac{\varepsilon_0 k T_e}{n_e e^2}} \tag{1.8}$$

where, ε_0 is vacuum permittivity 8.85×10^{-12} Fm^{-1}, and e is electron charge 1.6×10^{-19} C. The Debye length can used as a measure of the space charge scale, namely the plasma sheath thickness, as explained later on.

1.1.4 Plasma electron and ion frequencies

Characteristic frequencies of collective particles oscillations for electrons and ions respectively are determined by

$$\omega_{pe} = \sqrt{\frac{n_e e^2}{m_e \varepsilon_0}} \quad >> \quad \omega_{pi} = \sqrt{\frac{n_i e^2}{m_i \varepsilon_0}} \tag{1.9}$$

where m_e, m_i are electron mass and ion mass respectively. Typical values of plasma electron frequency concerned in this thesis are in the range around 10^{8-10} s^{-1}, while the plasma ion frequency is in the order of 10^{4-5} s^{-1}.

Spatially uniform plasma (without boundaries, which is an ideal theoretical case) can be classified as shown in figure 1.1, in terms of the above parameters. This thesis concerns an inductively coupled plasma (ICP) discharge, excited by a radio frequency (13.56 MHz) power supply. The plasma is maintained in a cylindrical chamber filled with a gas

at a pressure of around 10 mtorr. This sort of plasma has been recently shown to have a lot of advantages in modern semiconductor etching or plasma-enhanced chemical vapour deposition (PECVD) processes and other material surface modification applications [1-5]. A brief history of ICP will be given in next section 1-2 .

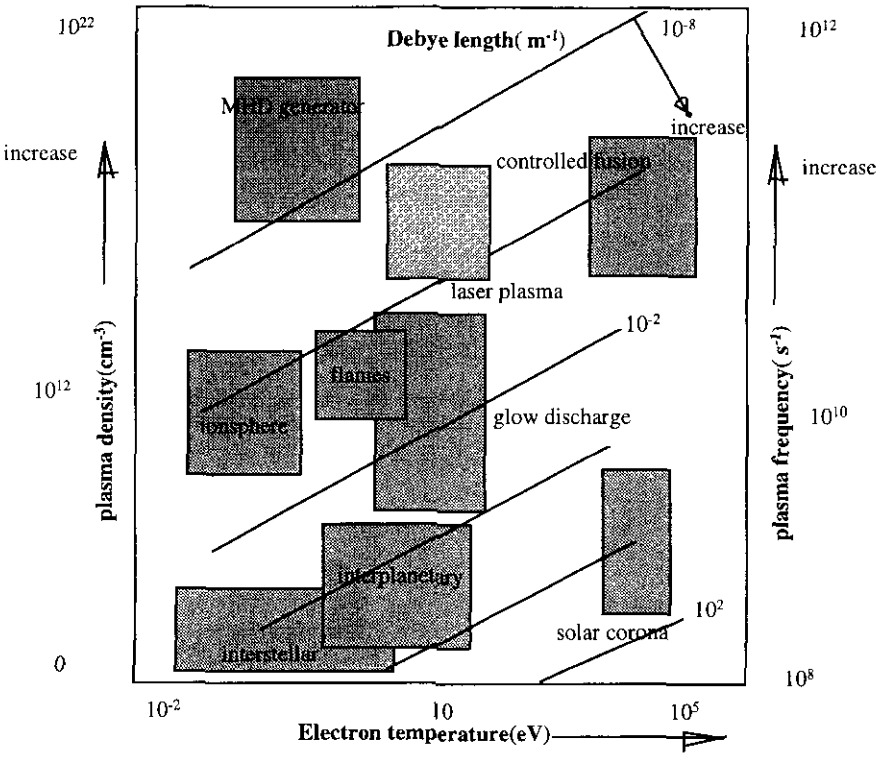

Figure 1.1 Classification of spatially uniform plasmas (see reference [5] for example)

1.1.5 Particle thermal speed

This speed is the average particle speed and is given by

$$\overline{C}_x = \sqrt{\frac{8kT_x}{\pi m_x}} \tag{1.10}$$

here x could indicate ions or electrons.

In weakly ionised gas discharge plasma, ion temperature remains the same as that of neutral gas, while electrons are considerably hotter, i.e., $T_i << T_e$. Moreover, taking argon gas as an example, $m_i \approx 40 \times 1836 m_e$, therefore, as it can be seen from (1.10), ions move much slowly than electrons. The higher mobility of the electrons results in a greater initial loss rate for negative charge from the discharge. This causes the plasma to acquire a net positive charge with respect to adjacent surfaces through self-consistent particle motion. In discharge plasmas, the resultant electrostatic field must behave in such a way, that it retards the electrons and drives the ion loss until at equilibrium, or at least steady state, there is no net time-averaged current flow from the plasma to isolated surfaces.

1.1.6 Plasma sheath and presheath

In a spatially uniform plasma $n_i \approx n_e$ and plasma quasi-neutrality ensures that the local electric field tends to zero according to equation (1.3). However, near a boundary, $n_i \neq n_e$, there must be some transitional space region where electric fields are not zero, which build up a bridge between bulk plasma and boundary surface. Those space charge regions, known as plasma sheaths, play an important role in all processing plasmas. A schematic illustration of the plasma sheath and presheath in contact with a substrate is shown in figure 1-2. The fast-moving electrons are not confined in the electric field-free bulk plasma region, and this negative charge mobility leads the electric potential down in the plasma presheath and sheath regions. Therefore, all the positive ions are accelerated into the sheath region where ion density is larger than that of the electrons and ion velocity is given by a quantity, $\overline{C}_s$, which is the averaged ion speed near the plasma-

sheath edge. It is also called the ion Bohm's speed and is determined by electron temperature and ion mass [5]:

$$\overline{C}_s = \sqrt{\frac{kT_e}{m_i}} \tag{1.11}$$

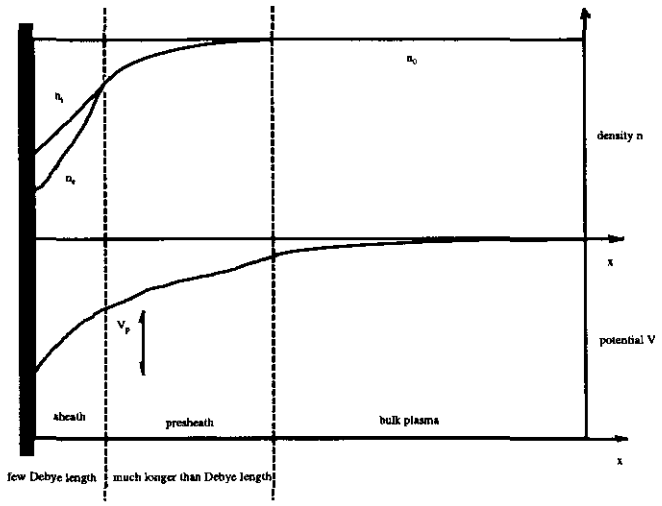

Figure 1.2 Qualitative behaviour of sheath and presheath in contact with a substrate

The well-known result that the ion flow speed must not less than the ion Bohm's speed at the plasma sheath edge is known as the Bohm criterion. To give the ions the Bohm velocity, there must be a finite electric field in the plasma presheath region. Furthermore, at the sheath-presheath interface there is a transition from slow ion flow to fast ion flow, where the condition of charge neutrality must break down. Putting in specific values of ionization mechanism, ion mean free path, and boundary conditions, the presheath and sheath can be theoretically described by use of equations (1.1-1.7) [6].

1.1.7 The sheath potential difference (plasma potential V_p)

The net positive space charge in the plasma sheath leads to potential profile that falls sharply to the local substrate potential near the boundary. This potential profile acts as a confining potential " valley" for electrons and a "hill" for ions because the electric field within the sheath points from the plasma to the substrate. The electrostatic potential difference between the sheath edge and the substrate potential is called sheath potential difference and sometimes is called plasma potential V_p. The directed ion kinetic power density flux to a substrate therefore can roughly be expressed by plasma potential and ion Bohm speed (see equation (1.11)) and it is an important feature of plasma based processing, such as etching, deposition and sputtering shown in figure 1.3,

$$\Gamma = en_i \overline{C}_s V_p \tag{1.12}$$

These losses (including electron-ion recombination near the wall and other particle-wall surface interaction) have to be compensated through ionization processes in the discharge. As it can be clearly seen from (1.11) and (1.12), the power carried by the bombarding ions could be controlled by modulating plasma density, electron temperature and plasma potential. The energetic particle fluxes from plasma can be used in the application of various material processing and surface modification, as explained in figure 1.3.

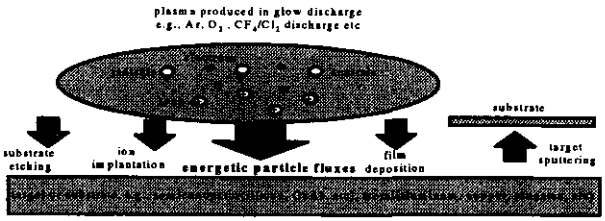

Figure 1.3 Schematic diagram of plasma processing of materials

1.1.7 Atomic collisions in a glow discharge

Atomic collisions can be classified as follows: (1) elastic collisions in which the energy exchanged during the collision is always kinetic; one example is the collision between identical electrons; (2) inelastic collisions in which some of the energy of the collision is transferred into potential energy of the particle struck, for example, excitation/deexcitation, ionization/recombination, attachment/detachment, and charge exchange processes are inelastic collisions. The main collisional processes in glow discharge plasma are between charged and neutral particles. Those processes take place at rate which depends on the density and nature of the gas and on the intensity of the electric field as well as on the charge on the particle. Their detailed treatment involves quantum mechanical treatment (see Electronics and Ionic Impact Phenomena, Massey and Burhop, 1955 [7] and Atomic and Molecular Processes, edited by D.R. Bates, 1962 [8]). For electrons at low energy and for ions scattering against neutrals, the dominant process is relatively short-range polarization scattering. At higher energies for electrons, the collision time is shorter and the atoms do not have time to polarize. It has been known that the electron collision cross section in glow discharge plasma approximately is inversely proportional to the electron speed and the collision frequency is independent of electron velocity [5].

1.1.8 The electron effective collision frequency υ_e and RF power dissipated in the plasma

It is well known that a free electron in a vacuum under the action of an RF field oscillates with velocity $\frac{\pi}{2}$ out of phase with the field, and thus takes no power, on the time average, from the applied field. The electron can gain net energy from the field only by suffering collisions with other objects (neutral atoms, ions, electrons, chamber wall, etc) and it does so by having its ordered oscillatory motion changed to random thermal motion on collision. The electron randomises energy on each collision until it is able to make an inelastic collision with an object. The fact that the average electron can continue to gain energy in the RF field, despite that it may move with or against the field, can be seen by showing that the energy absorbed is proportional to the square of the electric field and hence independent of electron motion direction [9, 10].

A fundamental quantity that characterizes electron collisions including all the elastic and inelastic processes, such as electron-electron, electron-neutral, electron-ion, electron-wall, and electron-electromagnetic field interactions (stochastic heating or cooling, see [5]), is its effective collision cross section Q, which is defined for a single electron as the probability of collision divided by the electron density at 1 torr and 0 K. The effective electron mean free path λ_e is defined by the average distance a particle travels between collisions and is related to the effective collision cross section Q, the density of collision partner n_g in the following form,

$$\lambda_e = \frac{l}{n_g Q} \tag{1.13}$$

The effective electron collision frequency is the number of interactions per second that an electron has with the target particle population and is determined by the electron speed and the effective electron mean free path as follows,

$$\upsilon_e = \frac{v_e}{\lambda_e} = n_g Q v_e \tag{1.14}$$

It has been generally agreed that the lower the gas pressure, the smaller the effective electron collision frequency; also the higher the RF frequency, the higher the electron collision frequency. The above collision frequency plays an important role in coupling electric power into the bulk plasma, as is explained in the following analysis based on use of the basic plasma equations (1.1-1.6):

First of all, the RF power dissipated in the plasma is given by

$$P_d = \iiint_{volume} Re\left\langle \underline{J} \bullet \underline{E} \right\rangle d\Omega \tag{1.15}$$

here *Re* means the real part and Ω is the differential plasma volume element. and the bracket denotes the time-average process, $\underline{J}$ is given by equation (1.5). To see how the dissipated power is related to the effective electron collision frequency, the Boltzmann equation of (1.6) has to be solved first, because it describes the effect of applied electromagnetic forces and effective collisions on the electron velocity distribution function f (EVDF). If we assume that there is no spatial variation in f, equation (1.6) can be simplified to be

$$\frac{\partial}{\partial t}f + \frac{eE}{m} \bullet \frac{\partial}{\partial v}f = \left.\frac{df}{dt}\right|_{collisions} \tag{1.16}$$

Writing the electric field as

$$E = E_0 + E_1(j\omega t) \tag{1.17}$$

where ω is the RF frequency, the first term on RHS of (1.17) represents the steady state electric field, and the second term denotes the RF field. During the transient analysis, we may write the total distribution function as the sum of the pseudo-stationary state distribution f_0, and a perturbation term f_1 contributed by the RF field E_1

$$f = f_0 + f_1 \tag{1.18}$$

where f_0 is considered to be the distribution function for small DC fields (in bulk and presheath regions), is spherically symmetrical and is nearly Maxwellian [5]

$$f_0(v) = n_0\left(\frac{m_e}{2\pi kT_e}\right)^{3/2} exp\left(-\frac{m_e v^2}{2kT_e}\right) \tag{1.19}$$

Rewriting equation (1.16) with the second-order terms eliminated, we find

$$\frac{\partial}{\partial t}f_1 + \frac{eE_0}{m_e}\frac{\partial}{\partial v}f_0 + \frac{eE_1}{m_e}\frac{\partial}{\partial v}f_0 = \left(\frac{\partial}{\partial t}f_0\right)_{collision} + \left(\frac{\partial}{\partial t}f_1\right)_{collision} \tag{1.20}$$

Separating this into two equations in E_0 and E_1, we have

$$\frac{eE_0}{m_e}\frac{\partial}{\partial v}f_0 = \left(\frac{\partial}{\partial t}f_0\right)_{collision}$$

$$\frac{\partial}{\partial t}f_1 + \frac{eE_1}{m_e}\frac{\partial}{\partial v}f_0 = \left(\frac{\partial}{\partial t}f_1\right)_{collision} = -\nu_e f_1$$

Turing our attention to the second of these equations and assuming f_1 has a time variation $e^{j\omega t}$, it is straightforward to derive

$$f_1 = \frac{eE_1(j\omega t)}{j\omega + \nu_e}\frac{\partial}{\partial v} f_0 \tag{1.21}$$

Combining equations (1.15), (1.5), (1.18), and (1.21) together, completing the time average process, the RF power dissipated in to the plasma is given by

$$P_d = \iiint_{volume} \frac{e^2 n_e}{m_e(\omega^2 + \nu_e^{\,2})} \nu_e |E_1|^2 \, d\Omega \tag{1.22}$$

here $n_e = \int_0^\infty f_0 dv$ denoting the average electron density, ω is the RF field frequency, $|E_1|$ represents the amplitude of the RF electric field, and υ_e is the effective electron collision frequency (it may consist of electron-neutral, electron-electron, electron-ion and electron-wall/electromagnetic field interactions), which has been already defined by equation (1.14) and assumed to be independent of single electron velocity in a weakly ionized plasma (where the polarization scattering collisions dominate the collisional processes [5]). In order to couple RF power effectively into a low pressure discharge plasma at fixed RF frequency, it can be seen from equation (1.22), that the plasma electron density, the effective electron collision frequency and the RF electric field distribution are the key factors to study.

Secondly, the plasma conductivity in a glow discharge can be introduced as follows

$$\sigma = \frac{e^2 n_e}{m_e(\omega^2 + \nu_e^{\,2})} \nu_e \tag{1.23}$$

so that the RF power dissipated in plasma can be simplified into

$$P_d = \iiint_{volume} \sigma |E_1|^2 \, d\Omega \tag{1.24}$$

This power is used in the plasma to create enough electron-ion pairs and excited particles, in order to compensate the particle flux lost to boundaries (see equation (1.12)) and to make the plasma continually "glow" (that is, some of the power is transferred into optical form by particle excitation and deexcitation processes and is the mechanism underlying gas lasers and discharge lamps). Hence, in a steady state, the power balance equation in the glow discharge plasma can be expressed as follows,

$$\iiint_{volume} \sigma |E_l|^2 \, d\Omega = P_c + \oiint_{surface} \Gamma ds + P_{optical} \qquad (1.25)$$

where the first term on RHS of (1.25) is the power to create charged particles and excited particles in the plasma through ionization collisions [5], the second term on the RHS of (1.25) is the loss power which can be decided from equation (1.12) and represents the power carried by particles bombarding boundaries which can be used to process material. The last term on the RHS denotes the optical radiation loss which could be used for other applications.

1.2 Background on low temperature low pressure plasma

A low temperature plasma is one in which the ions and neutral species have relatively little thermal energy compared with the electrons. It is generally created in glow gas discharge. The term 'low pressure' means that the gas pressure in the glow discharge chamber is roughly in the range of 1-100 mtorr, much lower than atmospheric pressure. At this range of pressure, the mean free path of an argon ion is the order of 1 cm, which is a little larger than the plasma sheath thickness, for an electron temperature of 1-10 eV,

and plasma density of $10^{17} - 10^{18} m^{-3}$; also the sheath thickness increases with the sheath potential difference. This condition ensures that directed energetic ion flux reaches the processing material surface from the plasma sheath edge without many collisions at least for low values of sheath potential difference. In this condition, the critical semiconductor material processing parameters such as anisotropy, selectivity and uniformity are readily controlled [5]. Normally, a glow discharge plasma is sustained by the input of energy through the passage of electrical current (DC or RF). The electrons gain energy from externally imposed electric fields and lose it to the gas atoms through collisions. Owing to the widely differing masses of electrons and gas atoms and the fact that only a small fraction of particles in the plasma are charged, thermal equilibrium between all species is not achieved. The electron population settles down with substantially more energy per particle than the heavy particle populations. The distribution of electron energy ε generally is similar to a Maxwellian EEDF with a mean around few electron volts (eV) or so [5].

$$EEDF = \frac{2}{\sqrt{\pi}} n_e T_e^{-3/2} \sqrt{\varepsilon} e^{-\varepsilon/T_e} \tag{1.23}$$

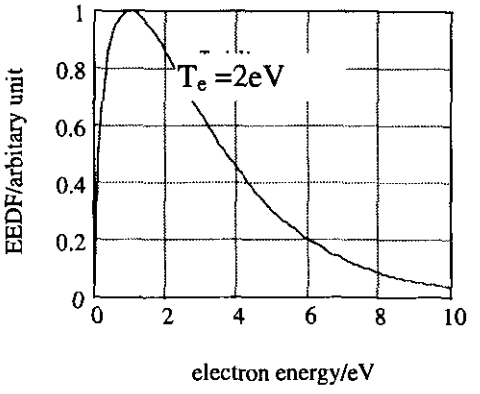

Fgiure 1.4 An example of a Maxwellian EEDF

Electrons in the tail of this energy distribution have sufficient energy (10-20 eV) to excite and ionize the gas which normally has an ionization level lower than 20 Volts [7] , and as a result it glows and is able to support the passage of electricity; hence the description 'glow discharge'. In molecular gases such electron energies are sufficient to fragment the gas into atoms and radicals, transforming it into a highly reactive "soup". The charged species are very much in the minority in a low temperature low pressure plasma but they nonetheless dominate the properties of the plasma because they are strongly coupled by the long range Coulomb force of electrostatics ($\propto r^{-2}$). In contrast the thermal energy of the gas remains close to the ambient at a fraction of an electron volt. The nonequibrium nature of low pressure, low temperature plasmas is characterized by electrons having substantially more energy than heavy particles. In molecular gases, owing to the presence of various rotational, transitional and vibrational energy levels, neutrals are also most likely to be not wholly in thermodymic nonequibrium.

1.3 Nature of RF glow discharge and history of ICP

Inductively coupled plasmas have been known for over a century. Many authors have analysed their operation [11-21]. It is worth listing some events in table 1-1, to see how the study of low temperature low pressure ICP has in recent years re-emerged owing to the need for high density plasmas for semiconductor manufacture and materials science [22-38].

In the DC-glow discharge, there is a continuous flow of ions and electrons to the cathode and anode respectively [8], so that these particles are continuously being removed from the discharge in this way as well as by ambipolar diffusion to the vessel wall. In the RF discharge, on the other hand, the continuous loss to the electrodes can be reduced to insignificance, as there is no uni-directional steady drift to the electrodes, if there are physical electrodes in the discharge chamber. The electrons gain energy from the RF field through various collisions and transfer energy to other particles until the average energy gain rate is equal to the loss rate just in the DC positive column.

It has been already known that in the steady maintained RF glow discharge there is no need for a generation process in order continually to supply electrons into the glow or plasma to compensate for those taken out by neutralization at the electrodes. An internal generation only is required just to compensate for the ambipolar loss (the energetic particle flux bombarding the wall or substrate) and thus there is no need for the mechanism represented by that of the cathode fall in DC-glow discharge where a considerable potential fall (100-1000 V) is needed to maintain the discharge. It follows that the RF glow discharge can be maintained at lower plasma potentials than are required for the similar glow of DC discharges [9, 10] and hence higher discharge efficiency can be achieved in RF glow discharge.

Types of RF discharges have been classified according to their mode of excitation [11, 12]:

(1) E-discharge, or capacitively coupled plasma (CCP), which is excited by the electrostatic electric field. The discharge conduction current is not closed in the E-discharge chamber.

(2) H-discharge, or inductively coupled plasma (ICP), which is excited by the electric induction field. The discharge conduction current forms a closed path in the gas in the H-discharge mode.

The conditions in which either of these modes can be excited have been previously investigated by [12-21]. It has been found that the basic processes with RF glow are the same as those in the DC glow, at RF frequency and medium gas pressure, the motion of charged particles is confined to the gas and volume losses due to diffusion, recombination and attachment must be balanced by ionization in the gas and the number of secondary production of electrons at boundaries is smaller than that of DC glow discharge. However, as the RF frequency and gas pressure is reduced, it is expected that the amplitude of the oscillatory motion of the electron cloud increases and loss to walls occurs, in which circumstances the properties of the boundaries affect the RF discharge, as is the case with the DC discharge [9, 10]. For given discharge chamber dimension and gas pressure/RF frequency, there is a cut-off RF frequency/gas pressure below which no discharge is obtained even with high fields (100 V/cm) [22]. Later work [23] indicated that in certain conditions a positive space charge could be set up which would reduce the amplitude of electron oscillation motion and hence reduces the operation pressure and RF frequency limit. Table 1.1 shows some events in low pressure low temperature ICPs.

1884	Hittorf.W	first report of a electrodeless ring discharge	to produce a sort of RF current induced discharge	developed a 50-year controversy of the criteria to judge CCP and ICP
1891	Thomson J	investigated different types of electrodeless discharge	to couple more external RF power and improve discharge efficiency	industrial application of electrodeless discharge became exciting issue
1947	G. I. Babat	presented the concepts of CCP & ICP (E-discharge and H-discharge)	to find the criteria of ICP	gave birth to ICP definition industrial use of ICP occurred at reality
1965	Stokes A D	theoretical description of EM field in a cylindrical ICP chamber	to solve Maxwell equations assuming electric conductivity profile	accelerated the development of high efficiency lighting industry
1989	J W Denneman	Determination of EM field of low pressure ICP in Ar-Hg discharge	to treat plasma as a secdonary turn of a transformer , simplified Babat & Stokes's theory.	intensified the theoretical study on ICP
1989	*Coultas D K and* Keller J H	*invented a new type of ICP,* the pancake device	*to obtain a uniform, high* density ICP source used in semiconductor processing industry	*renaissance of low temperature low* pressure plasma realized by material processing scientists
1991	G G Lister and M Cox	1-D Numerical modelling of ICP in internal and external coil devices	to Solve Maxwell's equations with different plasma conductivity profile	promoted the modelling of ICP maintained in a cylindrical chamber
1992	R B Piejak and VA Godyak , et al	A simple transformer model for analysis of ICP	to develop a practical model easily used in design and optimization tool for plasma processing source	promoted the modelling and experimental study of ICP
1992	J Hopwood et al	EM fields model in ICP maintained in flat coil discharge chamber (pancake)	to compare measured EM distribution with a finite element analysis code	stimulated the efforts to find an effective design tool for optimizing and understanding ICP source
1992	M. M. Turner	analysis electron heating process in ICP	to present new theory to explain the RF power coupling mechanism in ICP	introduced the concept of anomalous skin effect into low pressure ICP
1993	S.F.Durrant	the effects due to addition of other gases to argon ICP for mass spectrometry are reviewed	to use argon ICP into analysis of organic materials	indicated that mixed gas ICPs have a promising future in ICP-mass spectrometry
1993	V.Comello	point out the promising future *of ICP in semiconductor* etching business	to compare the characteristics *of ICP with conventional* electron cyclotron reactor	indicated that ICP etchers start to *challenge ECR*
1994	A.P. Paranjpe	theoretically and experimentally reported a discharge model for Ar ICP	to study electromagnetic field distribution in the ICP discharge	states that the induced electric field at substrate can cause substantial wafer heating at high RF power levels during semiconductor etching, deposition processes
1995	V.Vahedi & M.A.Liebermann	analytically shows the RF power dissipation process	to study power coupling mechanism in ICP	to review recent papers on power coupling theory in ICP
1996	J.A. Meyer, R.Mau, and A.E.Wendt	diagnostics of ICP by induction loop probe	to measure ICP electromagnetic parameters	electron drift motion is considered to account for observed EEDF
1997	H.M. Wu, et al	describes a systematic study of argon plasmas in a bell-jar inductively coupled plasma (ICP) source over the range of pressure 5-20 *mtorr and* power input 0.2-0.5 kW	to use the well-known the global model as well as two-dimensional (2-D) fluid model in the analysis of a argon ICP in a bell-jar-top discharge chamber	Bell-jar-top argon ICP has been studied theoretically and experimentally.

Table 1.1 some events in low pressure low temperature ICPs

This thesis is a theoretical and experimental study of the physics of a low pressure (5-50 *mtorr*), *low electron temperature* (1-10 eV), *high density* (10^{17-18} m^{-3}) *argon inductively* coupled plasma maintained in a cylindrical chamber. A two-dimensional electromagnetic, finite-element model has been set up to simulate the operation of the inductively coupled plasma using the external coil configuration used in the experimental work. Given the RF input power and the measured plasma density profile, Maxwell's equations and MHD theory are used to calculate the self-consistent electromagnetic field. A number of predictions are presented and compared with experiments. This sort of plasma has recently been widely used to sputter-deposit aluminium, tungsten, or high-temperature superconducting films [5].

1.4 Outline of this thesis

In the next chapter, the experimental set-up of the inductively coupled plasma used in this thesis is described, including the unit for RF power matching, the design of the electrostatic screen, the design of the RF inductor coil, the vacuum system and various diagnostics units. In chapter 3, experimental results are presented and discussed. Using basic plasma equations (1.1-1.6), the simulation of ICP is given in chapter 4. Further theoretical treatment and conclusions in this study are given in chapter 5.

Chapter 2 Experimental operation and diagnostics of an inductively coupled plasma

2.1 Introduction

As stated in the previous chapter, inductive discharges are nearly as old as the invention of electric power, with the first report of an "electrodeless ring discharge" by Hittorf in 1884. He wrapped an RF powered coil around an evacuated tube and observed a discharge. A subsequent 50-year controversy developed as to whether these discharges were capacitively driven by plasma coupling to the low- and high-voltage ends of the cylindrical coil, or were driven by the induced electric field inside the coil. This issue was resolved with the recognition that the discharge was capacitively driven at low plasma densities (E-mode discharge), with a transition to an inductive mode of operation at high densities (H-mode discharge). Succeeding developments led to the invention of the open air induction torch and its use for spectroscopy in the 1970s. Around the mid to late 1980s inductively coupled plasma devices operating at low pressure were proposed for plasma processing of semiconductor devices. The practical requirements such as anisotropy, selectivity, uniformity, etc, from the semiconductor processing industry, can be well achieved in the ICPs. Inductive discharges for materials processing are sometimes referred to as TCPs (transformer-coupled plasma), ICPs (inductively coupled plasmas), or RFI plasmas (RF inductive plasmas). The ICP notation is used in this study. There are many types of ICPs studied around the world, depending on their different applications. Two major types are shown in figure 2.1, where a DC magnetic field can be further

employed along the vertical axis, according to different applications [5] in order to have better plasma uniformity or higher plasma density.

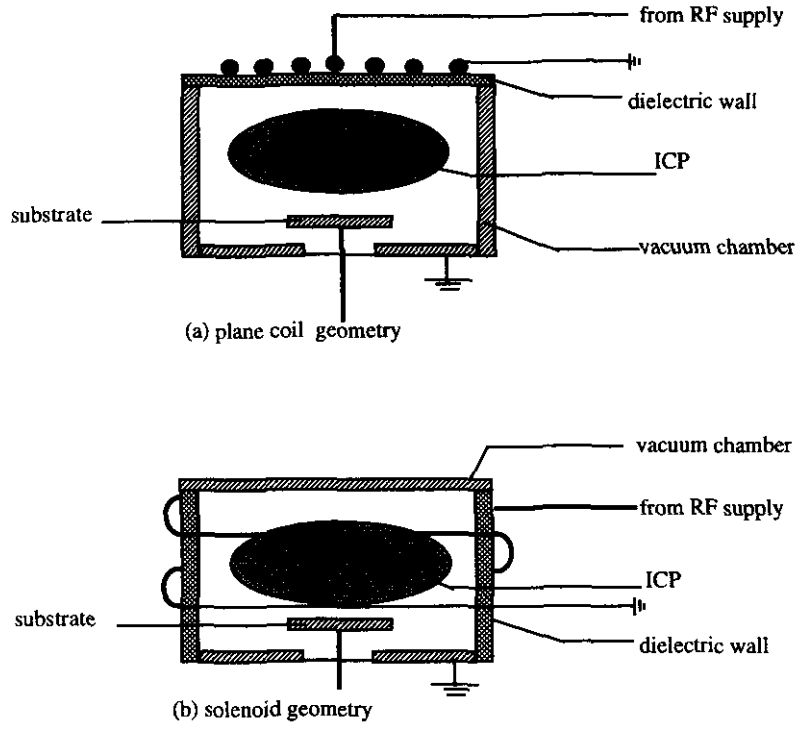

Fig 2.1 Typical ICP geometry

The first planar-coil systems for plasma processing were proposed by Coultas and Keller, later by Davis et al and then by Ogle [30-32]. Inductive plasma systems now dominate the advanced high plasma density market, led by the Lam, and the Applied Omega [32]. The former one is basically a planar coil device, while the latter one uses a solenoid RF coil.

Although many system are operated with planar coils, finite geometry effects make these configurations difficult to analyse [5]. In order to study low pressure and low temperature

inductively coupled discharge, a symmetric cylindrical inductive discharge system shown in figure 2.2, was set up at Oxford Research Unit of the Open University, UK, in 1992.

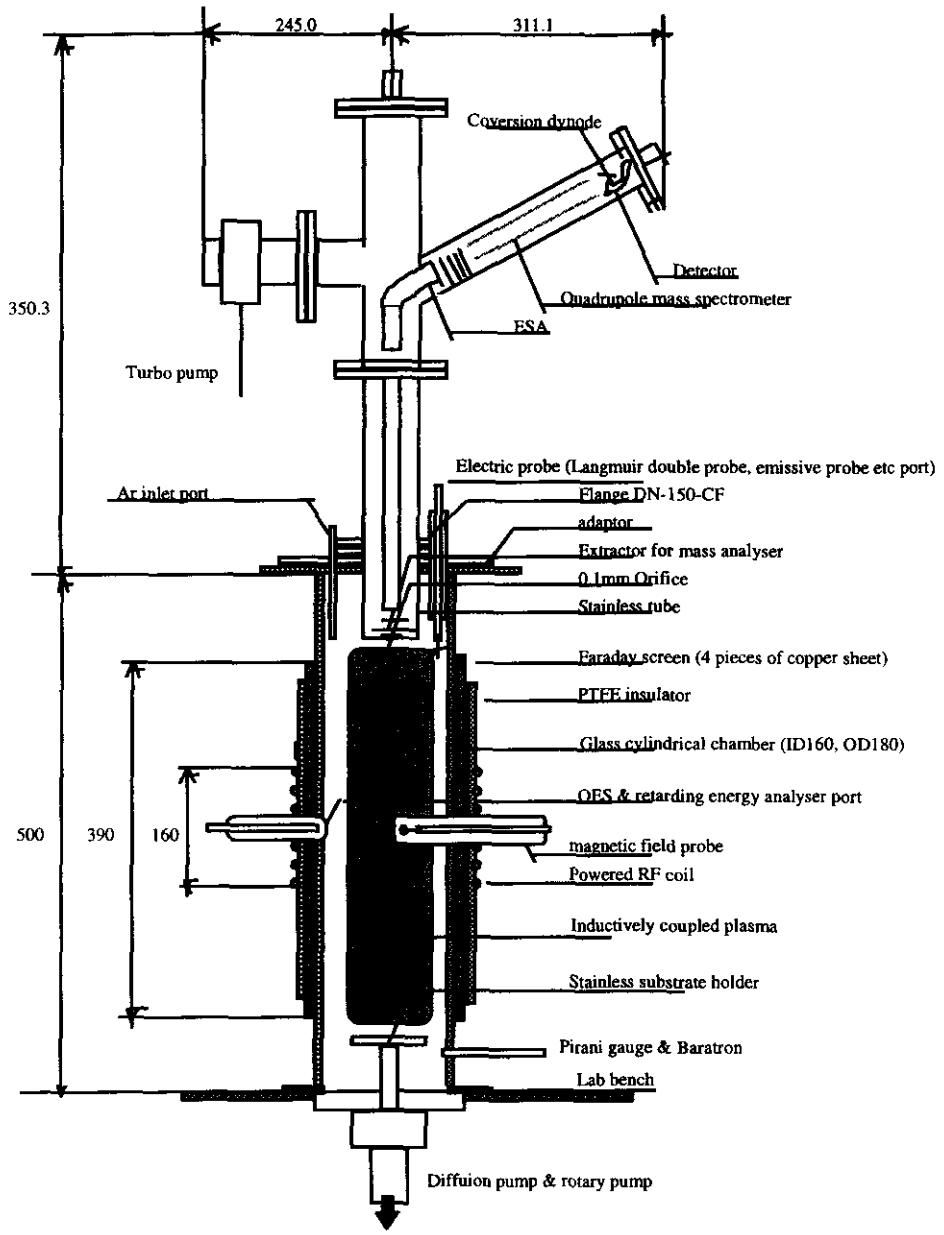

Figure 2.2 Experimental setup of ICP and diagnostic system at Oxford Research Unit

energy spectra of charged particle flux through a tiny hole on an external surface provide valuable data on conditions and processes occurring in the edge of plasma.

It is generally accepted that high-frequency breakdown has occurred when the volume ionisation due to electron-neutral or photon-neutral collisions equals the sum of volume loss process (recombinations, diffusions and charge-exchanges) (Herlin and Brown, 1948, MacDonald, 1966) [33, 34]. The ionisation is started by an external electrical field undoubtedly, therefore, different electromagnetic boundaries will determine different ionisation mechanisms. This is the origin of the concepts of capacitively and inductively coupled plasmas, i.e., E-discharge and H-discharge plasma. This can be further explained by use of the basic plasma equations in chapter 1 as follows:

Firstly, the general electromagnetic field solution of equations (1.1-4) are as follows (Feynman, 1950) [39],

$$\underline{B} = \nabla \times \underline{A} \tag{2.1}$$

$$\underline{E} = -\frac{\partial}{\partial t}\underline{A} - \nabla\phi \tag{2.2}$$

where $\underline{A}$ indicates the vector potential, ϕ is the electrostatic potential. And the first term on RHS of (2.2) is the definition of an inductive electric field, while the second term on RHS is the notation of a capacitive electric field.

Secondly, the vector potential satisfies the following equation [39],

$$\nabla^2 \underline{A} - \varepsilon_0 \mu_0 \frac{\partial^2}{\partial t^2} \underline{A} = -\mu_0 \underline{J} \tag{2.3}$$

where $\underline{J}$ is the plasma conduction current, and μ_0, ε_0 is the permeability and permittivity constant in free space, respectively. It can be shown from (2.3) that the vector potential is associated with the induced RF plasma conduction current, and vice versa.

Thirdly, the electrostatic potential and the vector potential are related through following expression [39],

$$\nabla \bullet \underline{A} = -\varepsilon_o \mu_o \frac{\partial}{\partial t} \phi \tag{2.4}$$

If the boundary condition is arranged in such a way that the self-consistent plasma conduction current is closed in the gas, (for example, in the case of an electrodeless discharge) i.e.,

$$\nabla \bullet \underline{J} = 0 \tag{2.5}$$

Then, substituting equations (2.4) and (2.5) into the divergence of equation (2.3) leads to,

$$\nabla \bullet \nabla^2 \underline{A} + (\varepsilon_0 \mu_0)^2 \frac{\partial^3}{\partial t^3} \phi = 0$$

Using basic vector operation rule $\nabla \bullet \nabla^2 \underline{A} = \nabla^2 (\nabla \bullet \underline{A})$ from reference [39] and equations (2.4) again, the above equation is transformed into the following RF electrostatic potential wave equation,

$$\nabla^2 \left(\frac{\partial}{\partial t} \phi \right) - \varepsilon_o \mu_o \frac{\partial^2}{\partial t^2} \left(\frac{\partial}{\partial t} \phi \right) = 0 \tag{2.6}$$

For waves propagating from an RF coil radially into the discharge chamber, assuming an axially symmetric boundary (this can be obtained by putting a Faraday screen surrounding the discharge chamber which will be addressed in next section), the general solution of (2.6) in a cylindrical coordinate is found as follows,

$$\phi = \alpha J_0\left(\frac{\omega}{c}r\right)sin(\omega t) + \beta Y_0\left(\frac{\omega}{c}r\right)cos(\omega t) + \phi_{DC} \tag{2.7}$$

Here ω is the RF angular frequency, c represents the light speed as usual, t is time, J_0 and Y_0 are the zeroth order Bessel functions of the first and second kind respectively [40], the real constants α and β are determined by some physical boundary conditions. The last term on RHS of (2.7) denotes the static DC potential.

Given an RF potential on the discharge chamber wall in the following form,

$$\phi_{wall} = \phi_w\, cos(\omega t + \gamma_w) \tag{2.8}$$

where constants ϕ_w, γ_w denote the amplitude and phase of the RF potential with respect the common earth respectively. A little algebra analysis leads to

$$\phi(r,t) = \phi_w \sqrt{\frac{\alpha^2 J^2{}_0\left(\frac{\omega}{c}r\right) + \beta^2 Y^2{}_0\left(\frac{\omega}{c}r\right)}{\alpha^2 J^2{}_0\left(\frac{\omega}{c}r_w\right) + \beta^2 Y^2{}_0\left(\frac{\omega}{c}r_w\right)}}\, cos\left\{\omega t + \gamma_w \frac{tan^{-1}\dfrac{\beta Y_0\left(\frac{\omega}{c}r\right)}{\alpha J_0\left(\frac{\omega}{c}r\right)}}{tan^{-1}\dfrac{\beta Y_0\left(\frac{\omega}{c}r_w\right)}{\alpha J_0\left(\frac{\omega}{c}r_w\right)}}\right\} + \phi_{DC} \tag{2.9}$$

On the other hand, supposing a perfectly-RF-earthed-Faraday screen (which will be described in next section) is surrounded outside the discharge chamber, the amplitude of

the RF potential on the wall is determined only by the RF conduction current flowing to the wall and the wall capacitance as follows,

$$\phi_{wall} = \frac{J_{er}}{\omega C_{wall}} = \frac{en_e V_{er}}{\omega C_{wall}} \tag{2.10}$$

here e is the electron charge, J_{er} and V_{er} represent the amplitude of electron RF radial current density and radial drift speed respectively, which will be studied in chapter 5, n_e is the electron density near the wall, and C_{wall} denotes the wall capacitance per unit area. Given the RF frequency 13.56 MHz, the wall thickness 10^{-2} m, the estimated electron density on the wall in the range of $1\sim5\times10^{16}$ m^{-3} (for a 100 W/10 mtorr argon ICP and it should be noted that the measurement of electron density on the wall is hardly possible by use of Langmuir probe due to a large space charge precence, thereafter the electron density on the wall which is less than the bulk plasma density 10^{17} m^{-3} is used here, in order to fulfil further analysis) and electron radial drift speed 10^3 m/s (that is 100 times smaller than the electron poloidal drift speed near the wall, which will be worked out in chapter 5), it can be shown from equation (2.10) that the amplitude of the RF potential on the wall is in the order of 10~50 V. Also at the RF frequency 13.56 MHz, in a cylindrical discharge chamber (ID 20 cm), J_0 and Y_0 , the zeroth Bessel functions of the first and second kind respectively [40] are roughly linear functions of radial position r. Based on those discussions, equation (2.9) can be quantitatively transformed into,

$$10\frac{r}{r_w}\cos(\omega t + \gamma_w) + \phi_{DC} \le \phi(r,t) \le 50\frac{r}{r_w}\cos(\omega t + \gamma_w) + \phi_{DC} \tag{2.11}$$

Here r_w is the cylindrical chamber radius, and γ_w is the phase factor of the wall potential. Equation (2.11) indicates that the RF space potential can be kept at low level (less than

100 V) in this sort of discharge plasma. This is the main advantage of ICPs, since the energy of ions arriving the substrate can be easily controlled by an independent voltage source [5].

In contrast, in the case of capacitively coupled discharge where the plasma conduction current is not closed in the gas, there must be a large RF electrostatic potential drop across the plasma sheath layer, in order to form the RF modulated space charge, to keep the total current being continued there. As result, charged particles move in a different manner in a capacitive discharge. This is why sometimes the ions are striking the substrate or wall with energies as high as 100-1000 V in a capacitively coupled plasma [5] and causing the damage of semiconductor devices during the processing; equally, this is the origin of the energy used in sputtering with RF plasmas.

Two discharge modes were observed in the experimental device studied here [41]. The first is a weak discharge, referred to as a capacitively coupled discharge plasma. It is produced by electrostatic fields between the ends of the solenoidal coil, which causes a weak ionization in the chamber. When the coil current is increased to a certain level (typically 10 A peak to peak for 10 mtorr argon gas in this chamber), the electromagnetic induction field drives in the plasma a poloidal current so strongly that a second intense discharge mode develops owing to inductive electron heating and subsequent ionzation process [42, 43].

In this thesis, the ICP plasma device in figure 2.2 has been studied experimentally, through various diagnostic methods including Langmuir probes, emissive probes, magnetic field probes, RF current & voltage probes, optical emission probes and mass-energy quadrupole analyser. Experimental data is compared with both numerical and analytical models. A typical database obtained from the inductive system and the diagnostics is shown in table 2.1.

Pyrex glass chamber size: ID=16cm ,OD= 20cm ,H=50cm						electric quanties through the induction coil				
Faraady screen deign: earthed seven H 36cm ,W 6cm ,T0.1cm copper sheets								amplitude	Vrf/V	170.00
induction coil design :H=25cm ;7 turns silver coated copper strap								amplitude	Irf/A	4.00
rf power source: f=13.56M Hz,w=2PI*f=8.52E+07,net output power=100W								difference	phase/deg	81.54
Langmuir probes, emissive probe, IEA probe, Hiden EQP probe, monolight OES probe are used here										
10mtorr Ar inductively coupled plasma database along radial direction on z=0 plane										
from double probe		from magnetic field probe								
Te/eV	**Ne/m-3**		**Bz/gauss**							**r/r$_w$**
2.60	1.60E+17		2.60		0.00E+00	0.00E+00	6.76E+05	0.00E+00	0.00	0.00
2.70	1.80E+17		2.60		1.00E+02	1.00E+03	6.89E+05	3.47E+04	0.05	0.20
2.70	1.75E+17		2.60		2.00E+02	3.00E+03	6.89E+05	1.07E+05	0.16	0.40
2.70	1.70E+17		3.40		3.00E+02	7.00E+03	6.89E+05	2.57E+05	0.37	0.60
2.60	1.30E+17		5.00		7.00E+02	4.00E+03	6.76E+05	3.60E+05	0.53	0.80
2.50	7.00E+16		5.90		1.00E+03	5.00E+02	6.63E+05	4.46E+05	0.67	0.90
double probe		emissive probe				capacitive Vrf probe	IEA probe	OES	EQP	
Te/eV	**Ne/m-3**	**DC-Vpw**		**VRFW**		**VRFW**	**ion energy**			**r/r$_w$**
2.60	1.60E+17	20		1		1.50				0.00
2.70	1.80E+17	18		1		1.50				0.20
2.70	1.75E+17	20		3		4.00				0.40
2.70	1.70E+17	25		10		6.50				0.60
2.60	1.30E+17	30		12		10.20				0.80
2.50	7.00E+16	28		18		15.00				0.90
							27	30	34	1

Table 2.1 Typical experimental database for 100 W/10 mtorr argon ICP.

Here V_d represents the electron drift velocity, V_{th} is the electron thermal speed,

r_w is the glass chamber radius and other quanties denote their own physical meanings as usual.

Details of how the above are obtained and their relevance will be discussed later and form the major part of this study.

2.2 Some considerations on the design of the ICP source

2.2.1 RF coil design:

Generally, whatever the discharge geometry is, an inductively coupled plasma can be simply considered as a single secondary turn of an RF power transformer. Hence, the greater the number of primary turns, the greater is the current induced in the discharge chamber. However, more turns will inevitably require a bigger electrostatic RF voltage across the two ends of the coil at a fixed RF current going through the coil, and that high electrostatic voltage may produce some capacitively coupled effects to the inductive system. An electrostatic shield (screen) placed between the coil and plasma could be used to reduced capacitive coupling. In practice, the commonly used RF coil at a frequency of 13.56 MHz has only a few turns, in order to keep the electrostatic field low and reduce the RF power dissipated in the inductor.

2.2.2 Faraday screen considerations

In order to make the RF component of plasma potential smaller, one needs to decrease the boundary electrostatic RF potential at the discharge chamber wall as much as possible. This can be achieved by use of a Faraday screen shown as follows:

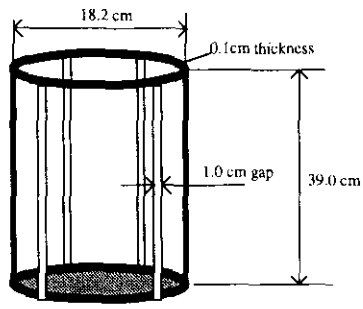

Figure 2.3 Schematic diagram of Faraday screen

This cylindrical screen was formed by four sections of 1 mm thick copper sheet. The gap between copper sheets was used to couple electromagnetic power into the Pyrex chamber, while the longitudinal continuity of the copper shorted the axial electrostatic field as it was designed to. A 1.0 cm gap was used to allow maximum RF power of 400 W to be transferred into the chamber. The height was chosen to be more than two times that of the RF coil, in order to eliminate any edge effects which may exist around the coil region in the axial direction. Theoretically, the number of copper section should be increased to as many as possible, in order to make better poloidal symmetry, which will be required in the theoretical study in chapter 4. Experimentally, the number of copper section was fixed at four, and a fairly good poloidal symmetric distribution of plasma parameters was obtained in the designed system, which will be shown in figure 3.5c.

2.2.3 Matching unit

In order to obtain the ICP discharge, a matching network between the RF power supply and its load, namely, the discharge plasma is needed. Basically, the matching unit is used to protect the power supply and increase power dissipated in the load, as shown in the following schematic circuit

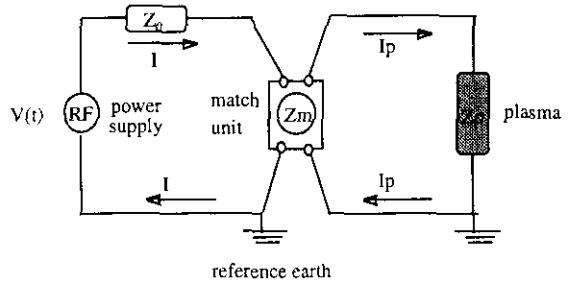

Fig 2.4 Schematic of the matching principle

The current going out from RF power supply is

$$I = \frac{V}{Z} \tag{2.12}$$

where V is the RF electromotive force (emf) provided by the power supply, and Z is the complex impedance of the overall system, which equals

$$Z = Z_0 + Z_L \tag{2.13}$$

where the first term on RHS of (2.13) is the equivalent impedance of the RF power supply plus transmission line. The second term is the overall load impedance, which is determined by matching unit impedance Z_m and plasma impedance Z_p in (2.14),

$$Z_L = \frac{Z_m \times Z_p}{Z_m + Z_p} \tag{2.14}$$

It is well know that when the overall load impedance equals conjugate of the characteristic impedance of the power supply, there is no reflected RF power back to power source [44]. This condition suggests that the matching unit impedance Z_m has to be

$$Z_m = \frac{Z_0^* \times Z_p}{Z_p - Z_0^*} \tag{2.15}$$

In principle, given the internal impedance of the RF power supply and the plasma impedance, the required matching unit parameters can be sorted out from the above expression. On the other hand, from measurement of external electric parameters (current, voltage, capacitance, inductance and resistance), one is able to know the effective plasma impedance [45]. It should be noted that normally a plasma impedance is a combination of

plasma sheath capacitance, bulk plasma inductance, and the plasma conductivity factor, each of them could be a nonlinear function of the RF field.

The matching unit and electric discharge circuit used in the work is a transformer-type RF matching network shown in figure 2.5,

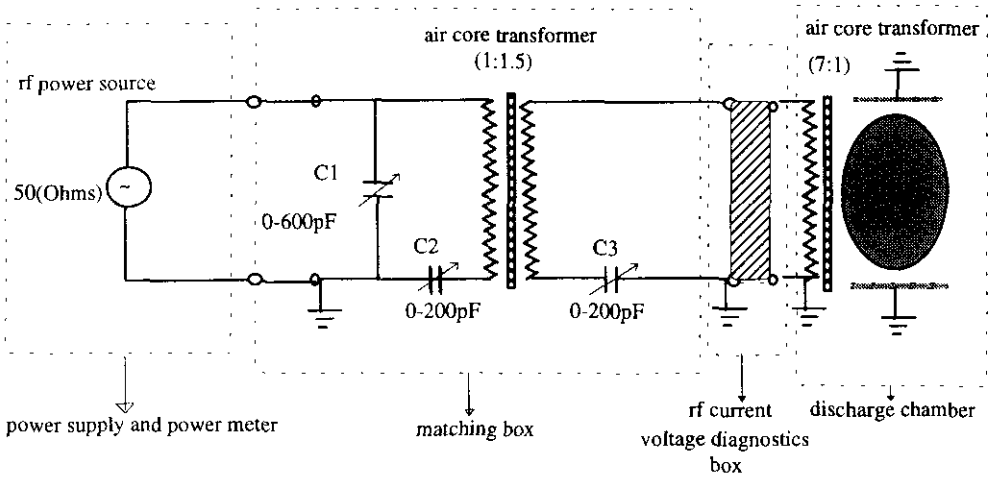

Figure 2.5 schematic show of the matching circuit in this work

During all the experiments, total power transfer efficiency into the discharge chamber could be measured [5, 46]. The principle is as follows: (1) Measure the RF voltage and current on the coil by an RF current-voltage sensor [47], the RF power dissipated in the lossy inductor and coupled into the discharge chamber is calculated as P_t, (2) Extinguish the discharge by increasing the pressure to 500 mtorr, the RF current measured will in general change, if C_1, C_2 , C_3 are kept unchanged, (3) Readjust the RF power source output until the RF current in the coil is the same as that measured in (1), and measure the RF voltage on the coil again, which will derive the RF power absorbed by the lossy

inductor transmission line, denoted by P_{loss} , (4) The RF power coupled into the discharge chamber is calculated by (P_f-P_{loss}). In this study, the RF power transfer efficiency as high as 95% was achieved for a 100 W/10 mtorr argon ICP by proper adjusting C_1, C_2 , C_3.

2.3 Diagnostic system

The topic of plasma diagnostics is a vast and diverse subject, even for investigating low temperature plasmas. In this work, the experimental data in table 2-1 was obtained through a number of different diagnostic techniques. The schematic diagram of the diagnostic system has been shown in figure 2-2. In the following section, we will describe the practical use of a Langmuir double probe, an emissive probe, a capacitive probe, a magnetic probe, a bolometric probe, a retarding field energy analyser, an optical emission probe, and a mass & energy filter system.

2.3.1 Langmuir double probe

From measurements of the current flow between two conductors biased relative to each other and immersed into the plasma, one is able to calculate the plasma density, and electron temperature. This method, introduced by Langmuir and analyzed in considerable detail by Mott-Smith and Langmuir (1926) [48] is usually called a double probe. It is generally used if there is no well-defined reference electrode in the plasma, as in an inductively coupled discharge. This technique provides valuable information on basic bulk plasma parameters. The sizes of the conducting tips have an important bearing on the analysis of the

current-voltage characteristics [49]. For instance, the probe tip size should be smaller than an electron mean free path to prevent perturbation of the plasma by the probe. Complications include vacuum sealing of the probe, allowing the probe tip to be replaceable (tip burnout can be a serious problem), and allowing the probe body to slide through a vacuum seal in order to scan the plasma. Details of various probe designs can be found in the literature [50-53]. A typical design is shown in figure 2-7. In an RF excited plasma, because the plasma must remain positive with respect to the electrostatic RF potential on the boundaries (see the formation of plasma sheath and presheath in chapter 1), the plasma potential also oscillates. As a result, the current drawn to a voltage-biased probe through the measurement circuit can be only interpreted properly provided that RF noise suppression techniques are used in the experiment [50-53]. The passive technique is to place a parallel LC resonant circuit in series with the probe tip tuned for a given RF frequency, so that the probe reactance to ground is much larger than the reactance between the probe and the plasma (in other words, the RF voltage across the probe sheath can be ignored compared with that of RF voltage appearing on the probe tip). The active RF noise suppression technique was introduced by Braithwaite, Benjamin and Allen (1987) [51]. They provided an active RF signal injected onto a Langmuir probe tip, which forced the tip exactly to follow the RF plasma potential variation; an RF phase shifter and attenuator/amplifier are tuned to optimised suppression. Both methods aim to make the probe tip able to follow the fluctuation of local RF plasma potential.

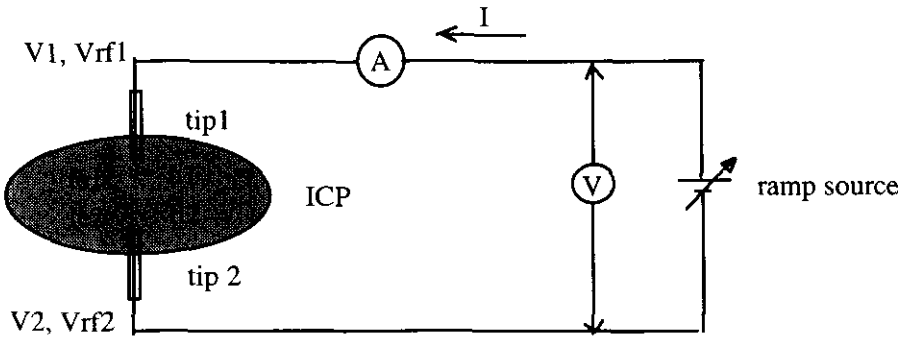

Figure 2.7 Principle of the Langmuir double probe circuitry

We have the following equations based on electrical circuit theory,

$$I_{e1} - I_{i1} = I \tag{2.16}$$

$$-I_{e2} + I_{i2} = I \tag{2.17}$$

$$V_2 - V_1 = V \tag{2.18}$$

$$I_{i1} = I_{i2} = I_i \tag{2.19}$$

In the presence of an electric field near the plasma sheath formed around the immersed probe tip, the EEDF of a maxwellian distributed electrons is in a similar form to equation (1.19), provided the electron kinetic energy factor could be replaced by the sum of electrostatic potential energy and kinetic energy. This assumption is usually called Boltzmann's relation (It should be noted that in the presence of large electron drift motion in some circumstances, this condition may be invalid. In this case, the double probe theory needs adjustment) [5, 10, 50]. Using this assumption, the time varying electron current collected by each electrostatic biased probe tip is straightforwardly worked out to be

$$I_{e1}(t) = n_0 eS\left(\frac{kT_e}{2\pi m_e}\right)^{1/2} exp\left(\frac{e}{kT_e}(V_1 + V_{RF1}\cos(\omega t))\right) \tag{2.20}$$

$$I_{e2}(t) = n_0 eS\left(\frac{kT_e}{2\pi m_e}\right)^{1/2} exp\left(\frac{e}{kT_e}(V_2 + V_{RF2}\cos(\omega t))\right) \tag{2.21}$$

where n_0 is the plasma density sampled by the tip, m_e is the electron mass, k is the Boltzmann constant, S is the effective probe tip area, and V, V_{RF} indicates the amplitude of DC and RF voltage on the tip with respect to a common reference point respectively, and ω is the RF angular frequency, t denotes time.

After complete time averaging, the mean electron currents flowing to probe tips are as follows (details are shown in appendix 1),

$$I_{e1} = n_0 eS\left(\frac{kT_e}{2\pi m_e}\right)^{1/2} exp\left(\frac{eV_1}{kT_e}\right) I_0\left(\frac{eV_{RF1}}{kT_e}\right) \tag{2.22}$$

$$I_{e2} = n_0 eS\left(\frac{kT_e}{2\pi m_e}\right)^{1/2} exp\left(\frac{eV_2}{kT_e}\right) I_0\left(\frac{eV_{RF2}}{kT_e}\right) \tag{2.23}$$

Here I_0 is the zeroth-order modified Bessel function of the first kind [40],

Combining (2.16-2.23) together and, it is straightforward to derive the double probe current-voltage characteristics in terms of RF voltage amplitude and electron temperature as follows:

$$I = \frac{I_i(\Gamma \exp(\frac{eV}{kT_e}) - 1)}{1 + \Gamma \exp(\frac{eV}{kT_e})} \tag{2.22}$$

where $\Gamma = I_0\left(\frac{eV_{RF2}}{kT_e}\right) \Big/ I_0\left(\frac{eV_{RF1}}{kT_e}\right)$ (2.23)

In principle, given the RF space potential in the plasma, fitting measured probe current and voltage to the above equation, one is able to find the plasma ion current and electron temperature. Moreover, for a collisionless plasma sheath, the collected plasma ion current by the probe tip can be treated as the Bohm flux current, which is simply determined by plasma density and Bohm speed (see equation (1.11)) as follows,

$$I_i = n_0 eS\left(\frac{kT_e}{m_i}\right)^{1/2} \tag{2.24}$$

here n_0 is the plasma denisty at the sheath-edge.

A typical experimental I-V curve is shown in the following figure:

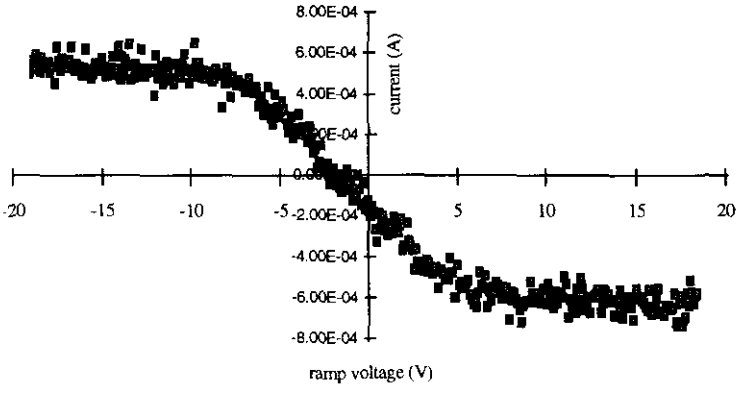

Figure 2.8 Typical double probe I-V curve from experiment in 100 W/10 mtorr Ar ICP.

A computer-controlled acquisition system (AEA Technology, UK) [54] was adapted for use in the experiments. The system consisted of an 486-based IBM-compatible PC with a 12-bit waveform generator (WFG) card and a 12-bit analogue-to-digital converter (ADC) card. Voltage ramp waveforms created by the computer were generated by the WFG and amplified in an external unit, giving maximum voltage limits of ± 50 V, before being directed to the probe. Currents flowing in the probe circuit were measured by a programmable gain amplifier (PGA) and then converted to a digital signal by the ADC card. The gain of the WFG was set by four digital I/O lines available on the WFG card and sensitivities of between ± 50 mA FSD and ± 0.125 mA FSD were obtainable, with corresponding resolutions from 0.025 mA to 60 nA.

All signals fed to and from the cards and their host computer were electrically isolated from the probe circuitry, which therefore had its own isolated ground plane. Twin-core coaxial cable was used to screen signals to and from the probe support from RF interference. Figure 2.9 shows the layout.

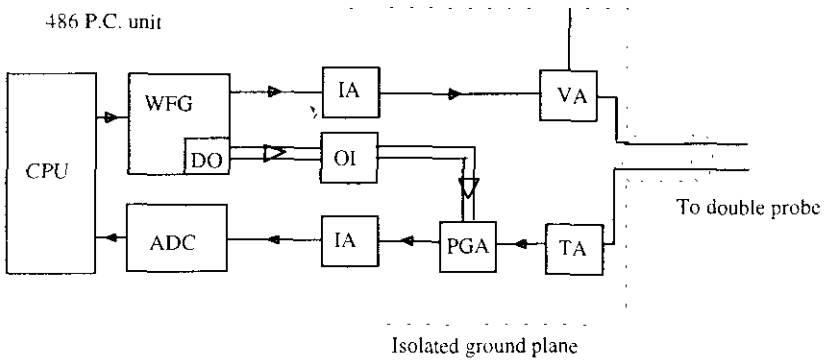

Figure 2.9 Schematic of AEA probe data acquisition system. WFG: waveform generator; DO: digital outputlines; ADC: analogue-digital converter; IA: unit gain isolation amplifier; OI: optoisolators;, VA: voltage amplifier; TA: transimpedance amplifier (current-voltage convertor); PGA: programmable gain amplifier.

Figure 2.10 shows the waveform used to sweep the electrostatic potential between the probe tips.

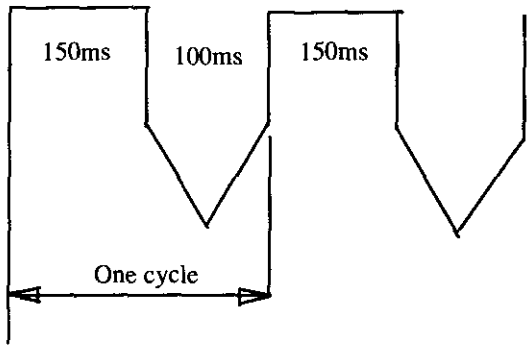

Figure 2.10 The voltage waveform sent to the probe by the AEA system

As is shown, the ramp waveform fed to the double probe was triangular with each period separated by a region of constant voltage. Probe characteristics were acquired during both the negative-going and positive-going ramps in each period.

Typically, the ramps had a 100 ms duration and were digitized into 1024 voltage steps, each of which, therefore, had a magnitude of less than 100 mV. The voltage at each step could be set with a resolution of better than 25 mV. During the region separating each pair of ramps the voltage on the probe could be used to condition, or clean, the probe by electron or ion bombardment immediately prior to a characteristics being obtained. This conditioning period was typically of 150 ms duration. Characteristics obtained during the positive- and negative-going ramps were averaged separately over a large number of ramp cycles. Depending on the intrinsic noise levels of the characteristics, the number of cycles was set between 10 and 1000, taking between 2 s and 3 minutes. With a 1000 shot

average, it was usually possible to obtain noise levels of better than 0.08%. Experimental data from this double probe are shown in next chapter.

2.3.2 Emissive probe

A hot wire electron-emitting probe can be used for a simple measurement of the plasma space potential. The probe filament is ohmically heated by a separate electric circuit. The electron emitting filament will not lose electrons to the plasma if the space potential of the plasma is below that of the filament. Hence, when the probe potential is swept through the plasma potential, there will be a sharp change in the probe current, owing to the emission of electrons strongly influenced by the local electric field.

When the probe is held negative with respect to the plasma potential, emitting electrons will leave the probe, contributing to the total measured probe current. When the probe potential is driven positive with respect to the plasma, the electrons are trapped by the local electric field and not able to leave the probe. Thus there is an abrupt change in the current when the probe potential passes through plasma potential. The differential of the probe current highlights this discontinuity which can be used to give a convenient measurement of plasma potential [55]. The filament is a C-shape tantalum wire (15 mm in length and 50 micron in diameter) as shown in figure 2.11,

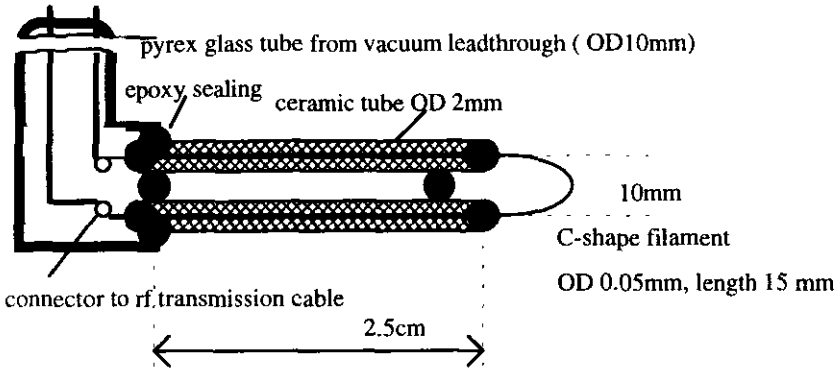

Figure 2.11 Schematic of an emissive probe

The construction of the emissive probe is essentially the same as the Langmuir probe, except that a filament is placed onto the double probe ends. The probe's emitted current should be made as large as possible because it is the emitted current which all emissive probe techniques rely on and exploit [56]. Except for very weakly emitting probes, space-charge effects limit the amount of emitted current which can escape from the probe when the probe bias is near or more negative than the local unperturbed space potential. Increasing the emitted current is partly achieved by using a thin wire. The smaller the wire diameter, the stronger the electric field at the wire surface and the less space-charge effects limit the emitted current. However, the wire can not be too small, as it must still be structurally sound when electrically heated. In practice, 0.05 mm tantalum wire is suitable for laboratory scale. For good spatial resolution, the length of the emitting wire of an emissive probe should be made as short as possible. However, it was observed that a good indication of the over-short filament is a frequent breaking in the middle of the wire, where the local temperature is significantly

higher than at the two ends. In practice, the length of the filaments is usually designed to be about 10-15 mm. The electric heating circuit for the emissive probe in this work is as follows:

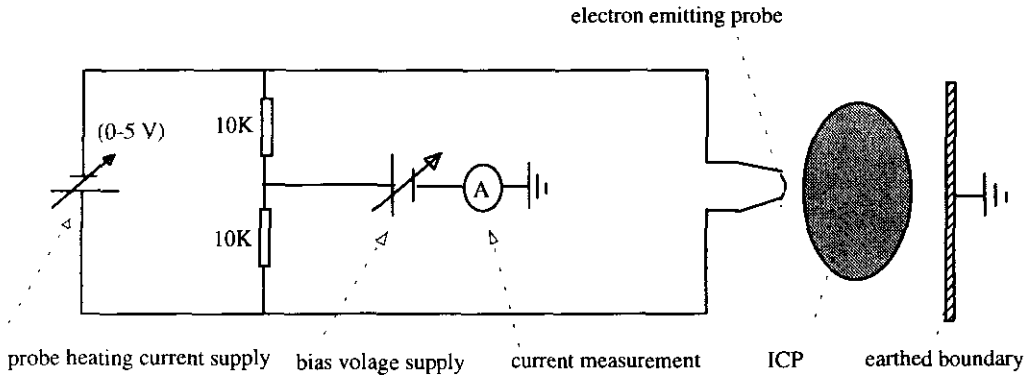

Figure 2.12 Schematic of emissive probe working circuit

2.3.3 RF capacitive probe

A small capacitance insulated from the plasma can be used to determine the RF component of the local plasma potential. If the space potential of a plasma oscillates at one frequency, the changing potential can be sensed using a capacitive potential divider in which the RF component voltage across the plasma sheath is negligible compared with that across the external capacitance. This probe can be treated as an RF voltage sensor.

The capacitive probe was put inside a vacuum-sealed Pyrex glass tube (OD 10 mm) which was movable in the cylindrical chamber as shown in figure 2.13, The probe tip is made of thin wire (OD 0.5 mm 3 mm in length) at the end of a 50Ω coaxial transmission line. The coaxial cable was terminated by a 50Ω load inside a LeCroy 9310 digital 300 MHz scope. The analysis of the frequency spectrum of the voltage signal V(t) on the

scope indicates that the RF high harmonic components are 20 dB lower than the fundamental. The probe was calibrated before it was inserted into the discharge chamber by a known RF voltage produced on a copper strap wrapped around the glass tube.

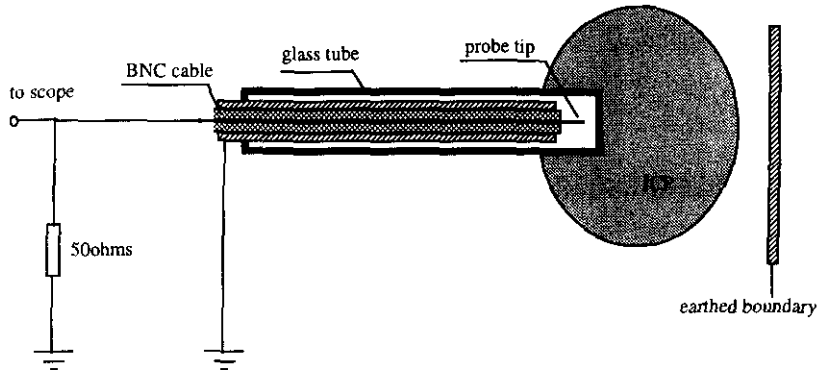

Figure 2.13 The schematic of RF capacitive probe

The external RF power matching condition did not need to be adjusted when the probe was inserted into the plasma. This observation suggests that the RF potential change owing to the capacitive probe could be ignored. The plasma RF potential can be derived from the measured scope voltage shown in the following equivalent electric circuit:

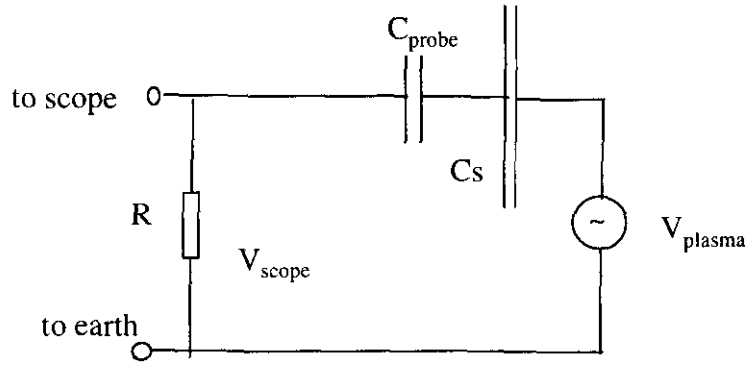

Figure 2.14 The equivalent electric circuit of a RF capacitive probe. Here R refers to the scope impedance, C_{probe} denotes the total capacitance of probe tip, the air gap and the glass tube, which can be made much smaller than the plasma sheath capacitance C_s.

The RF plasma potential hence is related to the scope voltage as follows,

$$V_{plasma} = \left(1 + \frac{1}{j\omega RC_{probe}}\right) V_{scope} \tag{2.25}$$

Experimental data from this probe are given in the next chapter.

2.3.4 RF magnetic field probe

This probe is an RF magnetic field sensor. A small loop immersed in the plasma can be used to derive the plasma electromagnetic field. According to basic plasma equation (1.1) and (1.2), the changing RF current in the plasma will produce magnetic field, this time-varying magnetic field will induce electric field. Hence, by measuring the induced electric potential, the corresponding magnetic field can be determined.

An inductive loop was positioned inside the plasma, sealed in a Pyrex glass tube (OD 8 mm) and movable along the radial direction on the mid-plane of the cylindrical chamber. The spatial resolution of this probe is limited by the effective probe tip size. The probe tip consists of single turn loop (square shape area of 2.5×2.5 mm^2) of thin wire at the end of a 50Ω coaxial transmission line. The coaxial cable was terminated by a 50Ω load inside the LeCroy 9310 digital 300 MHz scope. The analysis of the frequency spectrum of the voltage signal V(t) on the scope indicates that the RF harmonic components are 20 dB lower than the fundamental. The probe was calibrated by insertion into a known RF magnetic field produced by a solenoid without a plasma. The effect of capacitive pickup was found to be negligible by checking the signal when the probe was positioned

at the end of the RF coil, in the strongest capacitive field source around the discharge chamber, and by turning the probe parallel to the axial magnetic field.

The voltage induced on a single turn loop is given by [28],

$$V(t) = a\frac{dB(t)}{dt} \tag{2.26}$$

where a is the effective area of the loop, $B(t)$ is the spatial-averaged magnetic field through the small loop.

By measuring the amplitude of $V(r,t)$, one is able to determine the amplitude of magnetic field $B(r,t)$, given the RF frequency; by measuring the phase shift of $V(r,t)$ at different position, the relative phase distribution of $B(r,t)$ along radial direction is derived.

The experimental setup is shown in figure 2.15

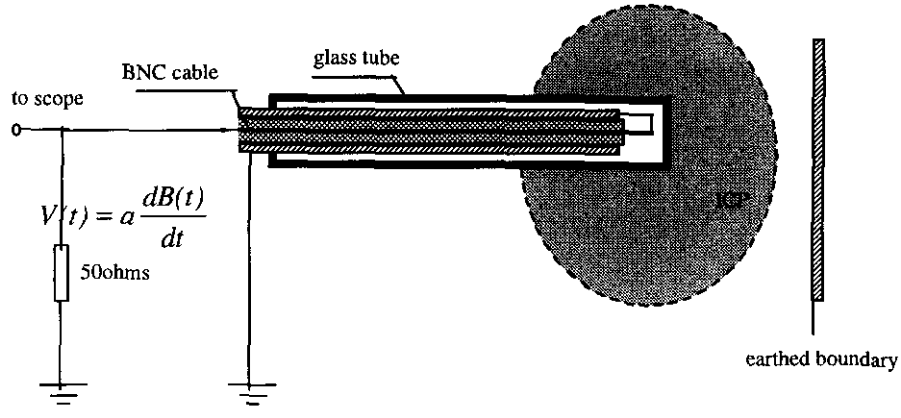

Figure 2.15 Schematic of a magnetic field probe

2.3.5 Retarding field energy analyser

The particle flux to a probe surface will be cut-off if the electric potential on the probe is properly biased to some level. This retarding field energy filter can be used to measure the energy distribution of the particles and hence derive information about the plasma potential [55]. The energy of charged particles can be analysed by a number of electrostatic and magnetic analysers. Many require a significant volume of vacuum chamber, with dimensions large compared with mean free paths in the discharge, so that some provision for particle extraction into a differentially pumped region is required. Such is the case where a quadrupole mass filter (e.g. Hiden EQP system) is installed. A retarding field type energy analyser has been designed to be mounted on the glass wall surface without disturbing the ICP, without additional pumping inside the analyser. A schematic of the analyser is given in figure 2.16:

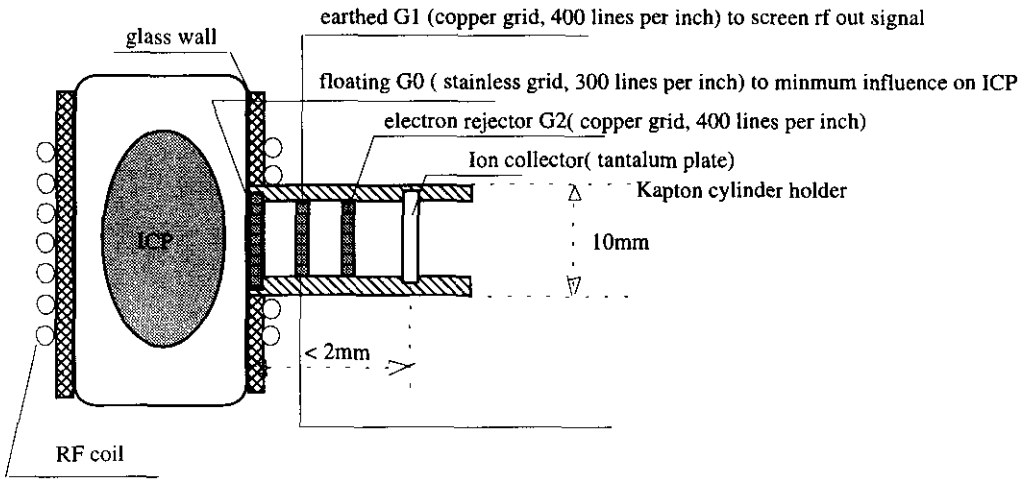

Figure 2.16 Schematic of the retarding ion energy analyser

The copper grids were made by Thorn EMI Vacuum tubes Ltd. using grooved glass masters. They are fitted in the analyser in a 'sandwich' construction using copper clad

Kapton as spacers, providing electrical connection to the grids through tabs. The thickness of the analyser was limited primarily by flatness of the grid and dielectric strength of the insulators; the thinnest design is required since there is no differential pumping for the analyser.

The principle of this analyser is as follows. The first grid G_0 is made of stainless mesh, which is assumed to be an equipotential array of floating sample apertures on the dielectric wall. To reduce the disturbance to the ICP, the second grid G_1 is an earthed sample aperture to screen RF fluctuation out of the analyser, the third grid G_2 is biased to reject electrons. The collector bias is swept until the ion flux is totally rejected. The collector current is measured using an isolating differential amplifier. The ramp voltage on the collector and the current going through the collector were simultaneously recorded by LeCroy digital scope as shown in figure 2.17.

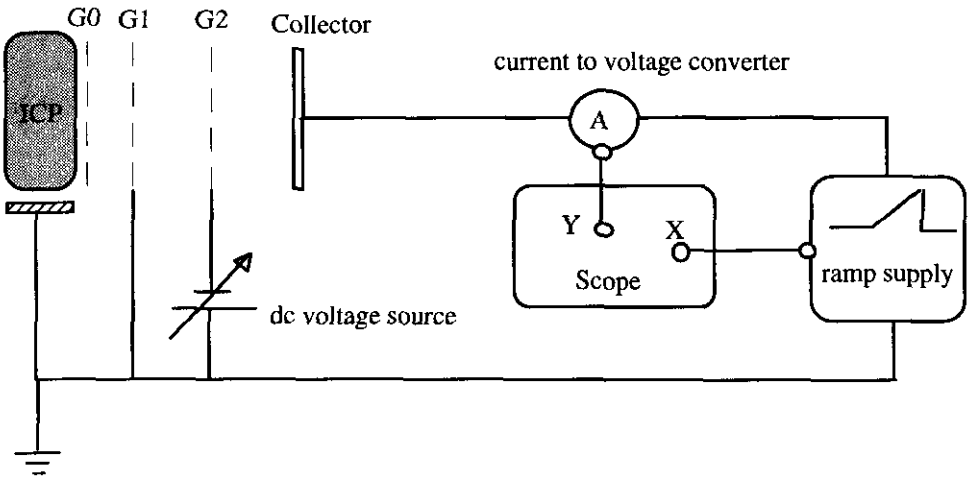

Figure 2.17 Schematic of the principle circuit for the analyser

The ion velocity distribution at the collector is related to the first differential of the collector current with respect to the retarding ramp bias and the plasma potential can be found by employing a proper plasma sheath model [55]. Results will be presented in chapter 3.

2.3.6 Optical emission spectrometer (OES)

The radiation resulting from electron impact excitation is commonly known as plasma-induced emission (PIE). By monitoring PIE, one is able to yield some information about the electron distribution function convolved with the species density for the optical wavelength being monitored and the cross section for electron impact excitation of the optical level. The optical emission density of the typical argon discharge lines are measured as function of RF input power and gas pressure.

Optical spectroscopy, which is a non-invasive diagnostic method, is widely used in a chemical environment, because it can offer some information on a wide variety of neutral and ionic species and on their environment. For example, fluorescence, induced when photons from a low power laser are absorbed and re-emitted by the target species, has been particularly well used in the last few years to elucidate some of the gas phase and surface reactions in plasma processing [5].

However, the work of this thesis is focused on the physics of the discharge itself, rather than chemical reactions. Therefore, argon gas is chosen for the discharge, in order to

investigate the physics of the plasma without the complication of chemistry. Argon, a commonly used benchmark gas for glow discharges, is a relatively simple test environment, where the argon plasma contains predominantly singly ionised argon ions, 99% of which are produced by singly-step electron impact ionisation [57].

There are a number of typical argon optical emission lines. Observation of 488 nm Ar^+ line in a helicon discharge plasma by a monochrometer provides information about plasma density [58]. In this work, a 200-900 nm dispersion element (a spinning grating) with a resolution of 0.7 nm shown in figure 2.18 was used to monitor Ar discharge emission lines from the chamber,

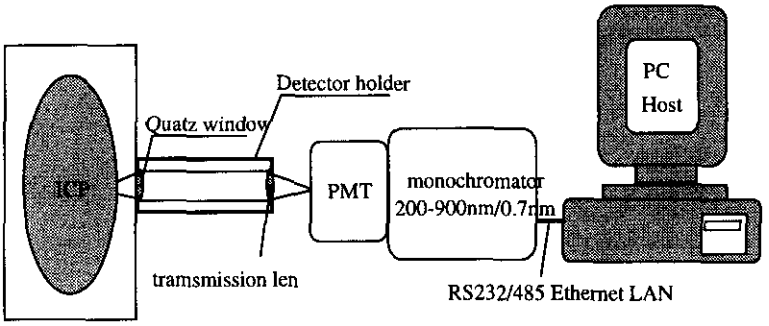

Figure 2.18 Optical Emission Spectrometer system used to monitor ICP

Figure 2.19 shows a typical optical emission spectrum for a 100 W/10 mtorr Ar ICP. Measurements show that a weak, blue discharge was started firstly throughout the chamber when the RF input power is greater than 20 W; the red domain lines intensify as the input power is increased.

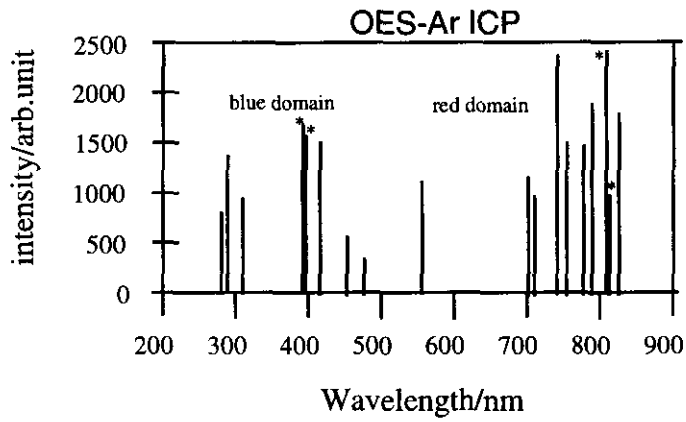

Figure 2.19 Typical optical emission spectrum for a 100 W/10 mtorr Ar ICP. Here the observed argon emission lines are marked by "" at 394.9 nm, 565.1 nm, 810.4 nm, and 811.5 nm. Other peaks are due to contributions from the residual gas in the chamber (e.g. water vapour etc.)*

Further study of these emission lines, such as the detail shape of each individual line, is the subject of another research field, beyond the scope of this work.

2.3.7 Bolometric probe

When a wire, immersed in the plasma, is biased very positive, or very negative, in addition to the ohmic heating by the current drawn from the plasma, there is an energy input due to the bombarding particles accelerated in the plasma sheath. This bombardment heating will be considerably greater than ohmic heating if the ohmic volt-drop is much less than the sheath potential difference. Measurement of the power deposited on the probe tip due to the particle heat flux will also show information about the local plasma potential, since the bombardment energy is determined by the potential difference between the probe and the plasma. The power dissipated on the probe tip was

measured by means of sensing radiation from the probe tip. This experiment is setup as follows:

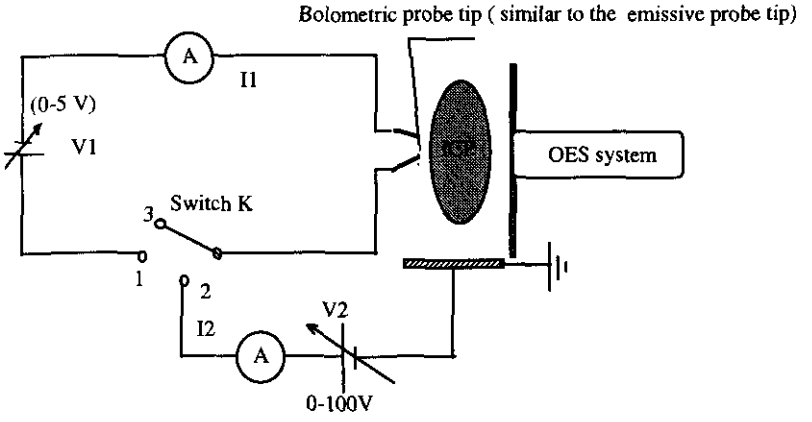

Figure 2.20 Experimental setup of a Bolometric probe for ICP

The operation of this probe is simply listed as follows:

(1) Strike a plasma, set K to position 3, record the ICP emission profile.

(2) Put K on position 2, positively bias the probe tip potential V_2, record another optical emission profile, then measure the current I_2 (which is the plasma electron current flowing through this circuit). The probe tip is assumed dominantly heated up by the bombardment power as follows,

$$P_2 = I_2(V_2 - V_p) \qquad (2.27)$$

This power is transported by the in-coming electrons which gain energy across the space sheath region around the probe, if the sheath is collisionless.

(3) Extinguish the plasma, set K to position 1, adjust V_1 until the observed black-body emission profile of this " hot filament" is the difference of emission profile in step (1) from the emission profile in step (2), then measure the V_I and I_I, the heating power on the filament is determined by,

$$P_1 = I_1 V_1 \tag{2.28}$$

(5) Equate (2.27) and (2.28), so that the plasma potential can be estimated by the following expression:

$$V_p = V_2 - \frac{I_1}{I_2} V_1 \tag{2.29}$$

Typical bolometric probe data compared with those from the emissive probe measurement in listed table 2.2 for a 10 mtorr Ar ICP are compared with results from other probes. The probe was positioned at the centre of plasma , I_1=300 mA, V_1=1±0.1 V.

RF input (W)	I_2 (mA)	V_2 (volts)	bolometric probe $V_p = V_2 - \frac{I_1}{I_2} V_1$ (volts)	retarding energy analyser results (volts)	emissive probe result (volts)
50	8	50	13	19	15
100	10	50	20	27	20
150	12	47	22	34	25
200	15	45	25	38	30

Table 2.2 Plasma potential in a 10 mtorr Ar ICP by a Bolometric probe, an emissive probe and a retarding energy analyser. The emissive probe was positioned at the centre of plasma, and the retarding energy analyser was installed near the glass wall.

Although results from bolometric probe have a similar trend same as those found from emissive probe, except at high power operation, errors in the estimation of plasma potential may appear by simply use of equation (2.29) because the real heating energy to

the bolometric probe tip should include other factors such as inelastic collisions between electrons, neutrals.

2.3.8 Mass/energy analysis

The kinetic energy of heavy charged-particles in the plasma can be measured using electrostatic and magnetic energy analyser separately by means of a quadrupole mass spectrometer (Coburn & Kay, 1972) [59]. The Hiden EQP system from Hiden Analytical Ltd (UK) is employed here to study the argon RF inductively coupled plasma (mass range 0-100 amu, energy range 0-100 eV).

Analysis of mass & energy spectrum of particle flux through a tiny hole on an external surface provide valuable data on conditions and processes occurring in the edge of the plasma. The Hiden EQP system is a high transmission ion energy analyser and quadrupole mass spectrometer designed for use as a plasma diagnostic tool. The spectrometer acquires data on mass spectra, energy spectra and appearance potential spectra, providing for detailed data on positive ions, negative ions, radicals and neutrals. Trends in intensity can be plotted against time. Transient and afterglow plasma can be studied with fast data acquisition. The EQP is additionally suitable for ion flux analysis from ion sources and drift tubes. In this work, the Hiden EQP mass spectrometer is installed as shown in figure 2.2. The following reported results only concerns the Ar^+ energy distribution, which provides information about local plasma potential. This system includes a sector field energy analyser, triple filter quadrupole analyser and ion counting

detector with differential pump housing and orifice sampling. The schematic of the system setup is as follows:

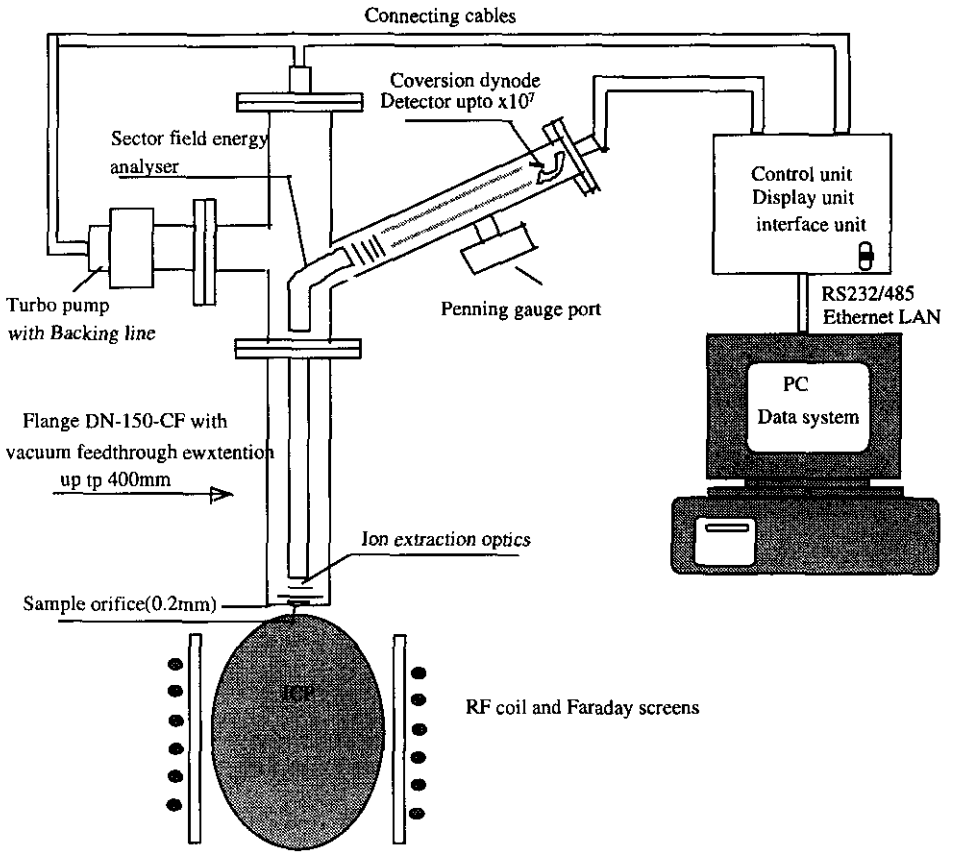

Figure 2.21 Schematic layout of the application of Hiden EQP system

Experimental data from this system are shown in next chapter.

2.4 Operation of the ICP

The schematic of the RF plasma device, and relevant experimental equipment have been already shown in figure 2.2. RF power at 13.56 MHz is coupled into the plasma through a 25 cm high, 16 cm diameter, 7 turn silver-coated copper strap coil. The Faraday screen

shields the electrostatic field between the coils. It is composed of 4 pieces of 0.1 cm in thickness, 6 cm wide and 36 cm long copper sheets. After the base pressure was lower than 10^{-5} torr, argon was admitted and flowed through the system to achieve an operating pressure in the range 5-50 mtorr. On applying RF to the coils, a weak, blue discharge was started first throughout the chamber. At 100 W input power level, an intense, pink discharge developed in the centre part of the Faraday screen. The first mode discharge is widely recognized as being due to the capacitive coupling effect, and the second stage discharge is due to the production of an inductively coupled plasma. Plasma parameters were determined from the diagnostic system described above.

In the next chapter, we are going to show the plasma parameters measured by use of the above diagnostic techniques.

Chapter 3 Experimental diagnostic results

3.1 Introduction

Numerous diagnostic methods have been proposed and successfully tried in the study of a high temperature plasma in thermonuclear fusion experiments [60]. For low pressure low temperature inductively coupled plasma in the application of semiconductor processing, most of the plasma parameters can be sorted out by use of the diagnostic system already described in previous chapter. For instance, plasma density and electron temperature could be derived from current-voltage characteristics of a Langmuir double probe, plasma potential could be known from an emissive probe, the energetic ions bombarding the substrate could be detected by use of retarding energy analyser or a newly invented ion flux probe [45], the RF electromagnetic field in the plasma are measured by a magnetic field probe and so on. In all experiments and the theoretical explanations in next chapter, the cylindrical coordinate system shown in figure 3.1 is used to model the plasma.

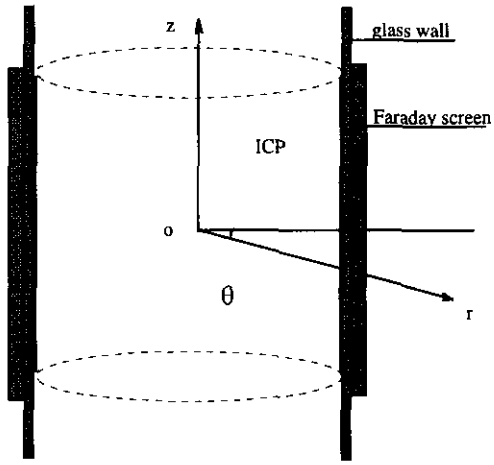

Figure 3.1 Coordinate used in this work. The origin is the centre of the cylindrical Pyrex glass chamber.

3.2 Measured electron temperature distribution

In order to be able to derive the plasma electron temperature, the measured double probe current-voltage characteristics must be compared with the theoretical I-V curves based on equations (2.22) and (2.23). First of all, from (2.22), at zero bias point, the derivative of probe current with respect to bias voltage is given by (3.1),

$$\left.\frac{dI}{dV}\right|_{V=0} = I_i \frac{1+2\Gamma-\Gamma^2}{(1+\Gamma)^2}\frac{e}{kT_e} \tag{3.1}$$

As it can be seen, the RHS is a combination of ion current I_i, RF potential ratio on probe tips Γ, and electron temperature in eV.

Secondly, from equation (2.18), it is straightforward to derive a relation between the offset voltage V_0 where the probe current is zero, the electron temperature and the RF potential factor Γ as follows,

$$exp(\frac{eV_0}{kT_e}) = \frac{1}{\Gamma} \tag{3.2}$$

Moreover, from the measured I-V curve, the ion current can be found by following approach,

$$I_i = I|_{V>>0} \tag{3.3}$$

Note that there are only three unknown quantities in equations (3.1-3) for a given a probe I-V curve. Therefore, fitting observed I-V curves to the above equations leads to data on plasma ion current, electron temperature and the RF potential ratio factor. Figure 3.2 shows an example of analysis result from the typical experimental data in figure (2.9).

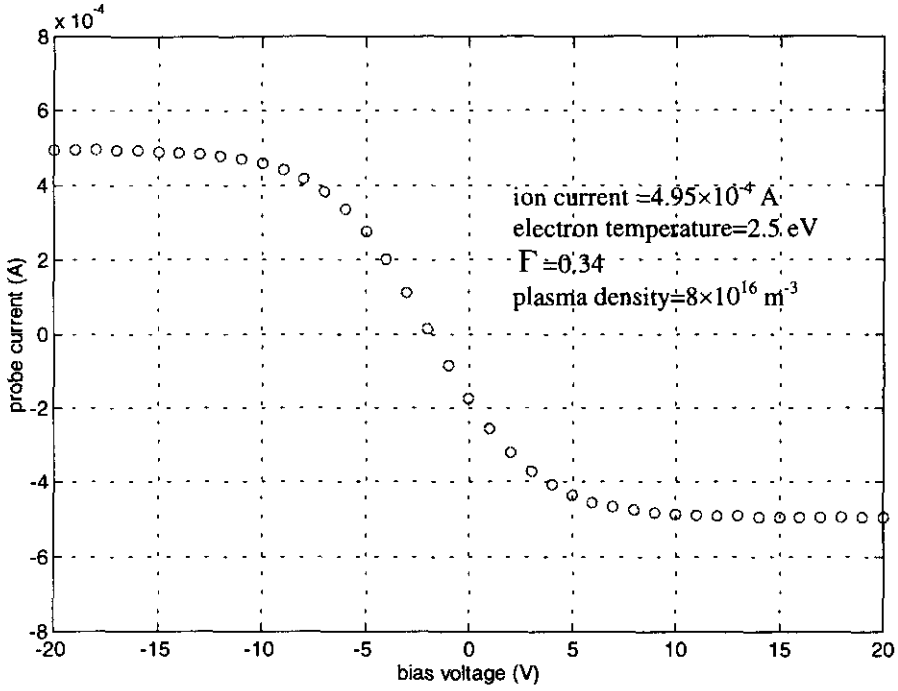

Figure 3.2 Fitted I-V characteristics of a double probe in 100 W/10 mtorr argon ICP based on equations (2.22-23). The probe was at r= 7.0 cm, z=0 cm. The area of probe tip is 1.57 $\times 10^{-5}$ m^2 . The plasma density was estimated from equation (2.24).

Figure 3.3 shows the measured electron temperature distribution.

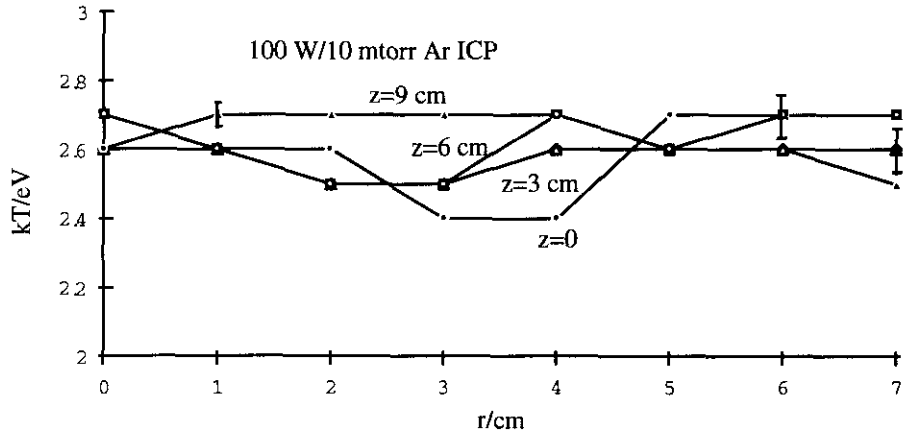

Figure 3.3 Electron temperature measurements in the ICP.

The error bar on vertical scale was estimated to be within 0.2 eV, based on spread of data on several experiments and also effected by the precision of determination

in finding the ion current in figure 3.2. The horizontal error bar was dependent on the actual probe tip size (few mm). The certainty associated with the analysis in general, was less than that of the experimental measurement. Figure 3.4 shows the measured electron temperature as function of gas pressure and RF power.

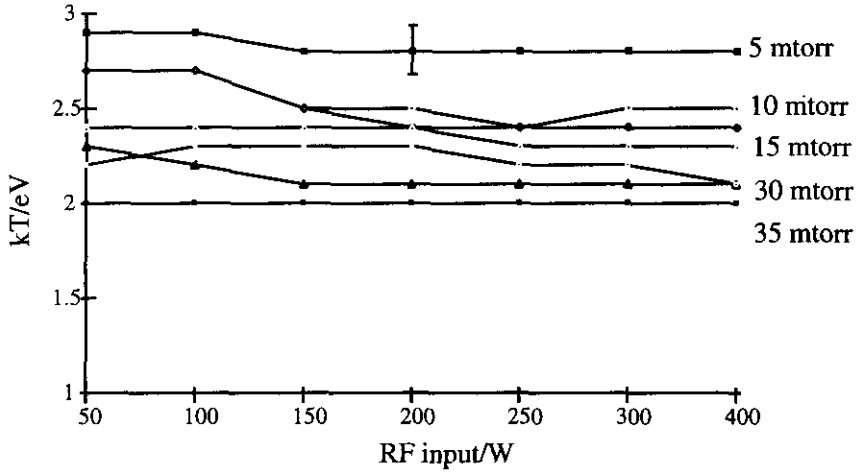

Figure 3.4 Measured electron temperature at the centre of ICP as function of input RF power and gas pressure.

The above two figures indicate that the measured electron temperature by a double probe is about 2-3±0.2 eV for a 100 W/10 mtorr Ar ICP. Also, measured electron temperature for lower pressure is seen to be slightly higher than that at higher pressure.

3.3 Measured plasma density distribution

The plasma density distributions measured by the double probe are shown in figure 3.5,

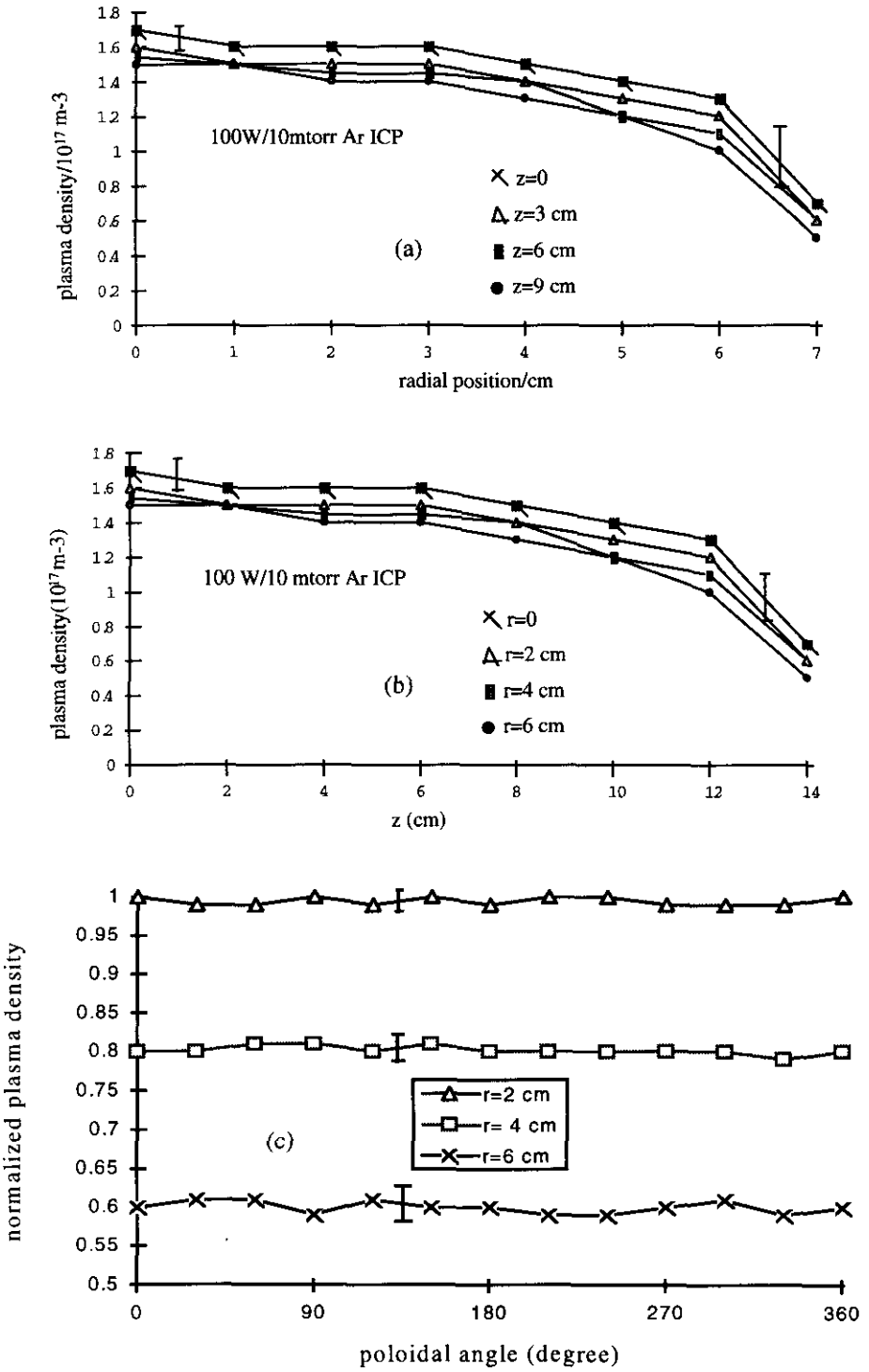

Figure 3.5 Measured plasma density profiles in ICP by a double probe. (a) radial distribution of plasma density. (b) axial distribution of plasma density. (c) poloidal distribution of plasma density.

Figure 3.5 shows that the ICP is well confined in the Faraday screen. The reduction of plasma density in the vicinity of glass wall is due to recombination of particles on the walls. Here the error bars were estimated based on spread of data on several experiments.

Figure 3.6 shows the plasma density as function of input power and gas pressure.

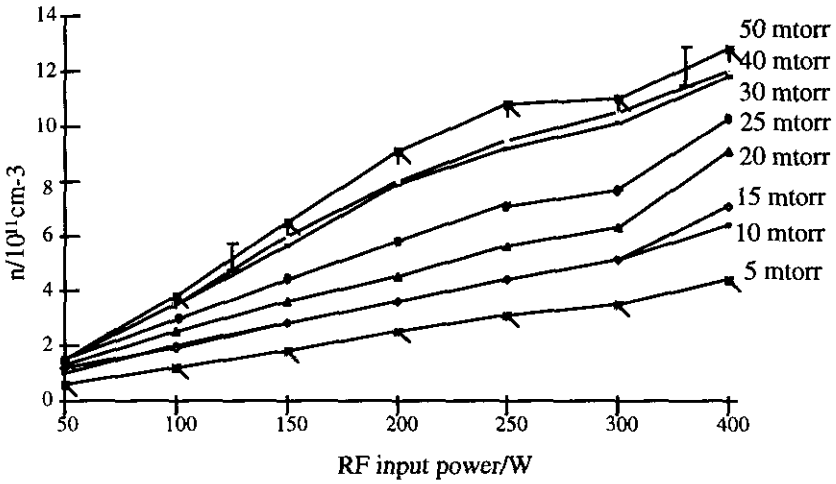

Figure 3.6 Plasma density as function of input power and gas pressure at the centre of ICP.

The above quasi-linear relation between ICP density and RF input power has been also reported for a flat coil discharge device in reference [5]. As it also can be seen, the increasing of gas pressure leads to the increasing of plasma density. It was found that when gas pressure was over 300 mtorr, it was difficult to obtained discharge in this device. It should be noted that it is difficult to measure the true pressure in the discharge, if the gas in the plasma is much hotter than the gas in the Pirani gauge. In this study, a fixed argon gas flow-rate at 40 sccc was used to

minimise the temperature effect to the pressure. Also care must taken to minimise the RF influence on the Pirani gauge output. The estimated error bar on the discharge gas pressure is 1 mtorr.

3.4 Measured plasma potential distribution

From equation (1.12), the directed lost ion kinetic power flux to the substrate (an important feature of plasma based processing), is related to the plasma potential, the ion Bohm speed and the plasma density. Hence, Measuring plasma potential is one of greatest interests in plasma diagnostics, and it also helps understanding of the overall picture of the charge particle motion in the plasma, which will be further discussed in the next chapter. In the experiment, the plasma potential was monitored by an emissive probe.

A typical probe current-voltage characteristic curve for an emissive probe in a 100 W/10 mtorr argon ICP is shown in figure 3.7, here the filament current was 500 mA, the potential difference between two ends of filament was 2.0 V, and the filament position was at r=5.0 cm, z=6.0 cm. The plasma potential was estimated to be 26.0 V, as indicated in figure 3.8. A typical measured plasma potential distribution by this probe in a 100 W/10 mtorr Ar ICP is shown in figure 3.9.

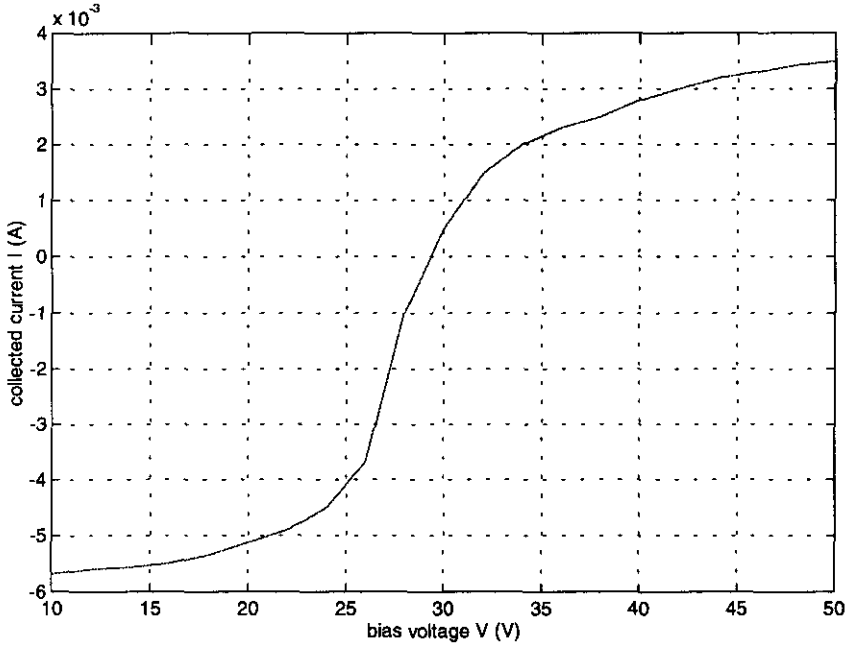

Figure 3.7 Measured I-V characteristic of the emissive probe in ICP

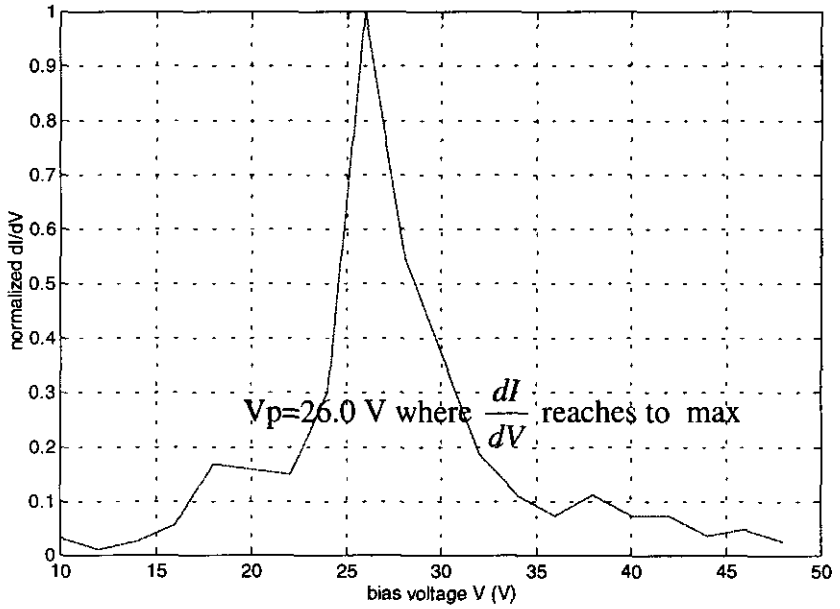

Figure 3.8 derivative of probe current with respect to ramp voltage

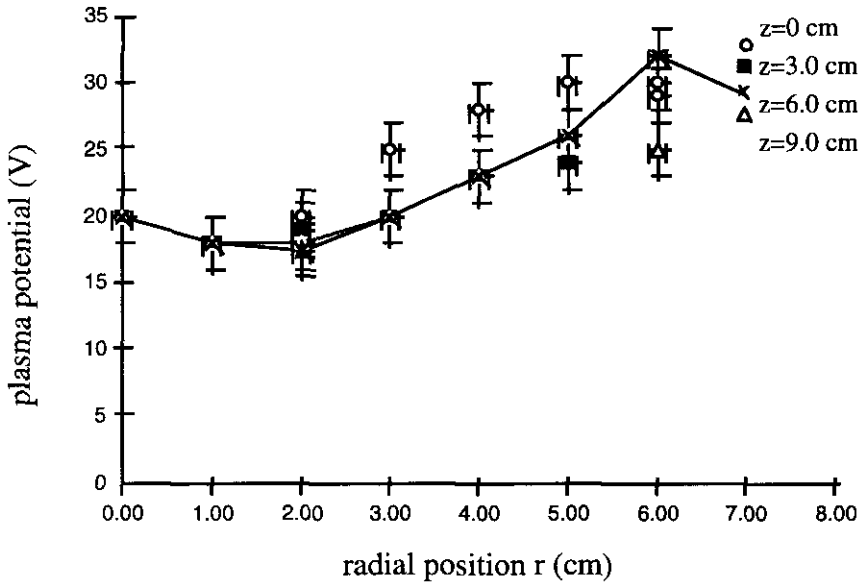

Figure 3.9 Plasma potential distribution in ICP

The measured data shows that the plasma potential is nonuniform along radial direction in the discharge chamber. The spatial resolution in the experiment was limited by the actual size of the probe. The observed ICP potential "hill" around glass wall has already been explained in [61, 62] by studying the ion sheath formation induced from the inward drift of the electron cloud in an inductive electromagnetic field. It should be noted that the overall charged particle momentum balance can be modelled by studying Maxwell's equations plus MHD equations, which will be addressed in chapter 4 and chapter 5.

3.5 Measured RF electrostatic potential distribution

Figure 3.10 shows the fundamental electrostatic RF potential measured by the capacitive probe and predicted by the equation (2.11); the higher harmonic component RF field was found less than 20 dB compared with the former part.

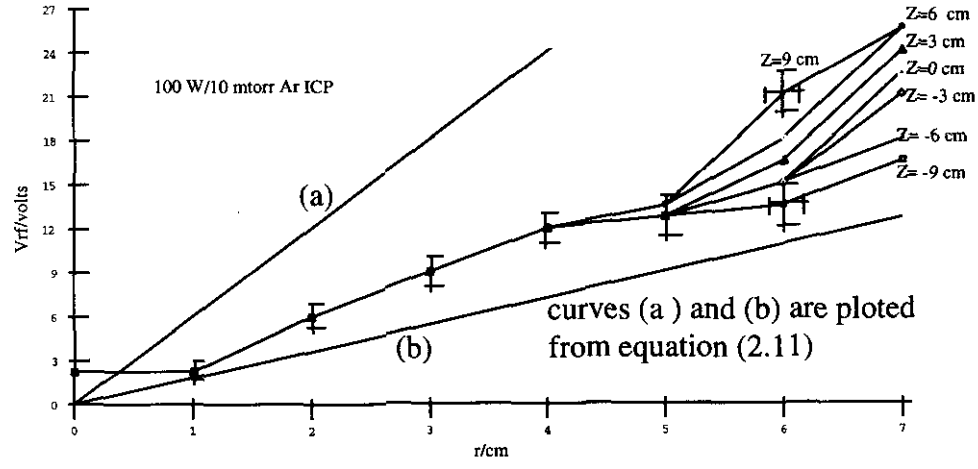

Figure 3.10 The electrostatic RF potential amplitude distribution in an ICP. Here the straight line is the theoretical prediction from equation (2.11) [the spread of data is dominated by precision to which the amplitude of oscilloscope trace could be determinated in the presence of experimental noise]

As can be seen, the RF potential profiles measured by the capacitive probe have the basic same trends as that predicted by equation (2.11). These data show that the axial electrostatic RF field is less than 1.0 V/cm inside the Faraday screen near the glass wall (1 or 2 cm away from the wall), and in most of plasma volume it can be ignored as it should, owing to the presence of Faraday screen. Also since the phase distribution of RF potential was roughly uniform along radial direction, it can be seen from these experiments that the radial RF electric field is estimated to be 5 V/cm near the glass wall at the z=0 plane. The spatial resolution in the experiment was limited by the actual size of

the probe. The differences between what predicted from equation (2.11) and the experimental data may be owing to: (1) The RF ion current flowing to the wall is not included in deriving equation (2.11), (2) It is very difficult to have a perfectly-RF-earthed-Faraday screen (in practice, there is only one earth point in an RF system), (3) It is hard to measure the true particle densities on the wall.

Now, we are going to derive the induction EM field based on the magnetic field probe measurement. First of all, as the higher component of the measured emf voltage signal was less than 20 dB compared with fundamental one, the magnetic field at z=0 plane and $V(r,t)$ can be written in the following form,

$$V(r,t) = V_0(r)\exp(j\omega t + j\Phi_V) \tag{3.4}$$

$$B(r,t) = B_0(r)\exp(j\omega t + j\Phi_B) \tag{3.5}$$

where $V(r,t)$, $B(r,t)$ are complex, ω is the RF excitation angular frequency, other symbols have their usual meanings. Substituting (3.4) and (3.5) in to equation (2.26), we have the amplitude and phase of the magnetic field being determined by equation (3.6),

$$\begin{aligned} B_0(r) &= \frac{V_0(r)}{a\omega} \\ \Phi_B &= \Phi_V + 90^0 \end{aligned} \tag{3.6}$$

here a is the area of the effective single turn loop, which could be calibrated in the experiment [28, 63, 64]. Once the magnetic field is known, using the axial form of basic equations (1.1) (details are shown in appendix 2),

$$\frac{1}{r}\frac{\partial}{\partial r}(rE) = -\frac{\partial}{\partial t}B \tag{3.7}$$

the poloidal induction electric field can be calculated by equation (3.8),

$$E(r,t) = E_0(r)exp(j\omega t + j\Phi_E) \tag{3.8}$$

where the amplitude of the induction field is found to satisfy

$$E_0(r) = \left[\left(\frac{1}{r}\int_0^r r\omega B_0 \cos(\Phi_V)dr\right)^2 + \left(\frac{1}{r}\int_0^r r\omega B_0 \sin(\Phi_V)dr\right)^2\right]^{1/2} \tag{3.9}$$

and the phase factor of the induction field satisfies equation (3.10)

$$\Phi_E = \tan^{-1}\left[\frac{\int_0^r r\omega B_0 \sin(\Phi_V)dr}{\int_0^r r\omega B_0 \cos(\Phi_V)dr}\right] \tag{3.10}$$

Moreover, from the poloidal form of basic equation (1.2),

$$\frac{\partial}{\partial r}(B) = \mu_0 J + \mu_0\varepsilon_0\frac{\partial}{\partial t}E \tag{3.11}$$

Hence, the plasma conduction current can be calculated to be

$$J(r,t) = J_0(r)exp(j\omega t + j\Phi) - j\omega\varepsilon_0 E_0\, exp(j\omega t + j\Phi_E) \tag{3.12}$$

where

$$J_0(r) = \frac{1}{\mu_0}\left[\left(\frac{\partial}{\partial r}B_0\right)^2 + \left(B_0\frac{\partial}{\partial r}\Phi_B\right)^2\right]^{1/2}$$
$$\Phi = \Phi_B + \tan^{-1}\left(B_0\frac{\partial}{\partial r}\Phi_B \Big/ \frac{\partial B_0}{\partial r}\right) \tag{3.13}$$

Furthermore, the averaged power dissipated in the plasma can be derived by calculation of time averaged product of $\underline{J}\bullet\underline{E}$ as follows,

$$S = E_0(r)J_0(r)\cos(\Phi_E - \Phi) \tag{3.14}$$

It should be note that the time averaged contribution to S from the displacement current term, i.e., the second term on RHS of equation (3.12) is zero.

Figure 3.11 shows a typical measured magnetic field distribution for 100 W/10 mtorr ICP at the z=0 plane.

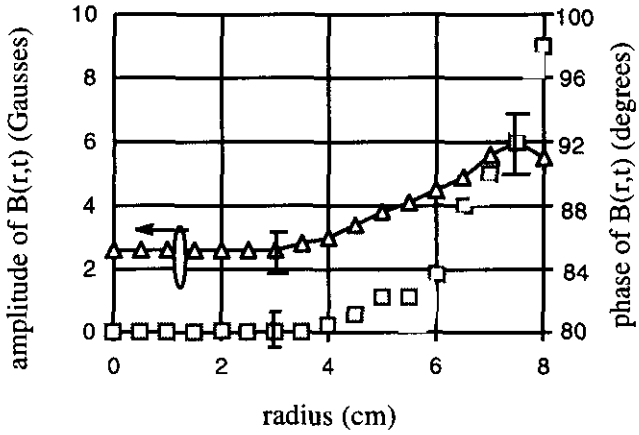

Figure 3.11 Measured axial magnetic field distribution by a loop probe at z=0 plane. The phase was measured with respect to an RF voltage signal on the RF coil.

The above data indicates that the phase of the magnetic field along radius is approximately uniform when r <4 cm, the spatial variation of phase is less than 20 degrees in the region as r >4 cm. It will be shown in chapter 4, that this phase distribution in turn indicates that most of input RF power is dissipated near the glass wall, rather than in the middle region of the discharge chamber. Similar results have been reported in [28, 63] in a planar inductively coupled plasma source. The radial and poloidal component of magnetic field were found negligible when compared with axial field (20 dB less or a factor of 100 times smaller in amplitude).

Typical derived plasma parameters from equations (3.6-14) at the z=0 plane are shown in figure 3.12.

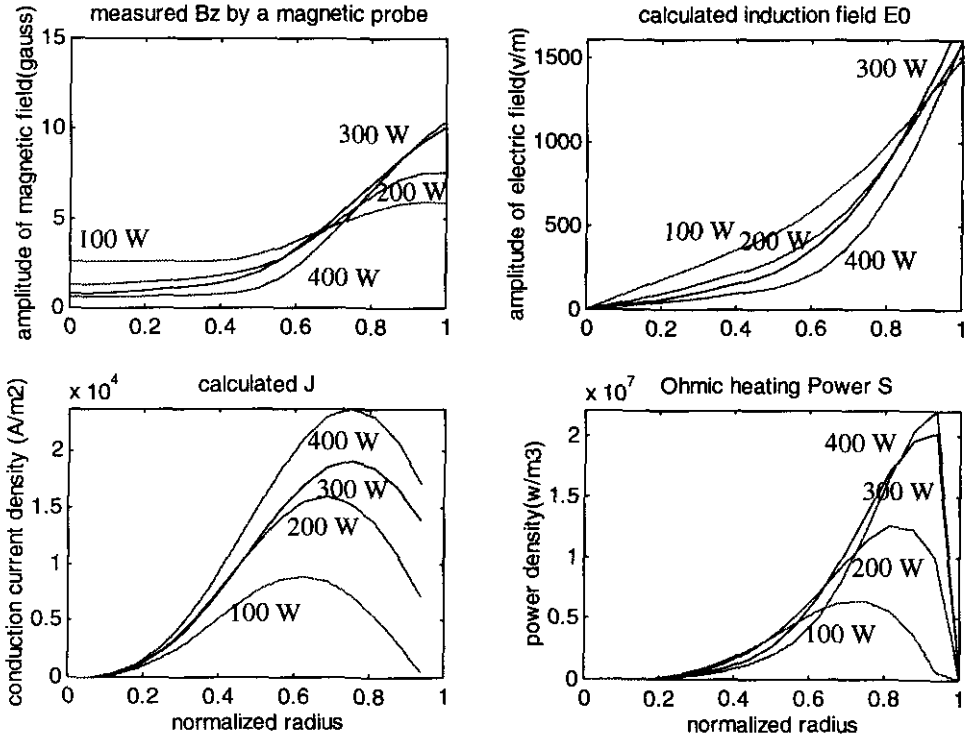

Figure 3.12 Typical magnetic field measured by a magnetic probe and derived electromagnetic field characteristics at the middle plane in a 10 mtorr ICP for different RF input power level.

The above experimental results show that both the axial magnetic field and inductive electric field are decreased when more RF power is coupled into the plasma, as it should due to the screening effect by the drift motion of the plasma electrons. Most of input RF power is dissipated near the glass wall, which implies that the electron effective collision processes play an important power coupling role near the glass wall (see equations (1.23-24)). The spatial resolution in the experiment was limited by the actual size of the probe, i.e., 0.5 mm.

Moreover, the data shows EM field falls to the plasam centre, in other words, EM field is attenuated when it encounters the plasma. As it can be seen from the above figure, the typical EM field propagation decay length of EM field in the experiments is about 1-2 cm in the discharge from the glass wall. This phenomenon can be easily explained by introduction of a plasma "skin depth" concept (it should be noted that the plasma electron frequency in the experiments is the order of 10^{10} s^{-1}, hence, the associated plasma skin depth is about to be 1-2 cm) [5, 28].

3.6 Ion velocity distribution functions (IVDFs) and ion energy distribution functions (IEDFs) in ICP

In a collisionless plasma sheath near to the collector, using the free-fall ion motion model, the ion current collected by a retarding energy analyser is straightforwardly determined by

$$I = ae\int_{v_i}^{\infty}(IVDF)vdv = ae\int_{v_i}^{\infty}\frac{dN}{dv}vdv \qquad (3.15)$$

where a is the collector area, dN represents the number of ions of velocity between v and v+dv, v_i denotes the minimum ion speed at which they reach the collector and therefore is given by equation (3.16),

$$v_i = \sqrt{\frac{2e(V_p - V)}{M}} \qquad (3.16)$$

Here e is electron charge, M is ion mass, and V_p is the space potential at the plasma sheath edge, V is retarding potential on the collector.

The ion velocity distribution functions at the collector is related to the first differential of the collector current with respect to the retarding ramp bias as shown in equation (3.17),

$$\frac{dI}{dV} = \frac{e}{M}(IVDF) \tag{3.17}$$

The plasma potential can be found at position where $\frac{dI}{dV} \approx 0$ [55, 65]. Figure 3.13 and figure 3.14 show the typical measured IVDFs and plasma potential in the ICP.

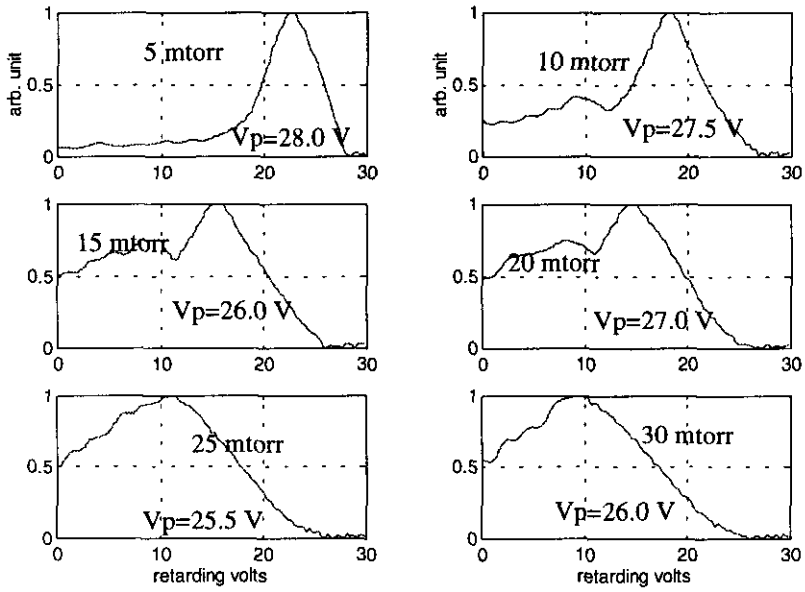

Figure 3.13 IVDFs vs gas pressure in ICP . RF input was 100 W. The retarding energy analyser was mounted in the wall at the z=0 plane. The plasma potential was determined at the retarding potential where no signal was observed.

The above IVDVs show the same basic trends same as the IVDF in an RF CCP device, reported in [55]. The broadening of IVDF as the pressure increases is attributed to ion-neutral collision processes and the main peak of the IVDFs is formed by the collected ions travelling directly across the plasma sheath edge [55]. As it can be seen, at fixed

input RF power, the variation of measured plasma potential is less than 2.5 V as the pressure increased from 5 to 30 mtorr .

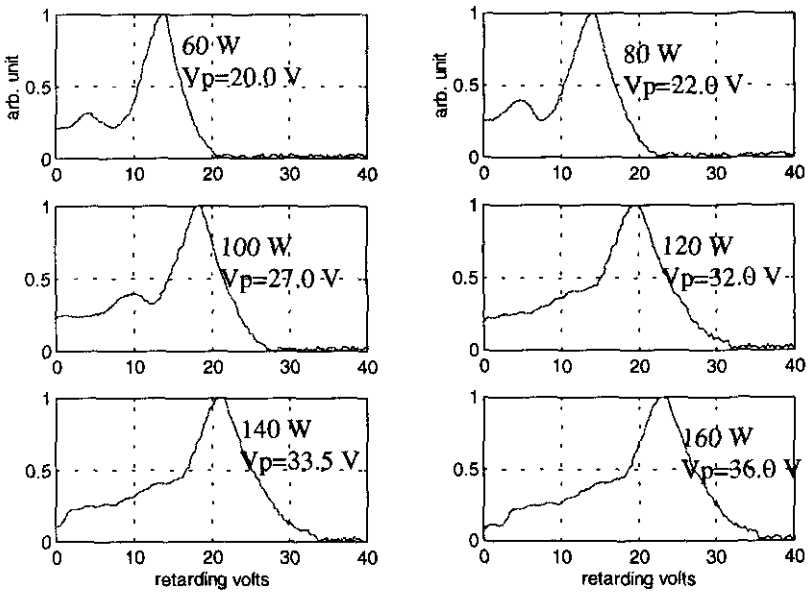

Figure 3.14 IVDFs vs RF input power. Ar pressure = 10 mtorr. The retarding energy analyser was mounted in the wall at the z=0 plane. The plasma potential was determined at the retarding potential where no signal was observed.

Moreover, as can be seen, when more RF power is coupled into the discharge chamber, the measured plasma potential increases. Also, because the electron-mean-free-path and the ion-mean-free-path (typically 1-10 mm) [5] around 10 mtorr Ar is much longer than the plasma sheath scale λ_D (typically 0.1 mm) in this experiment, there is no need to consider charge-exchange and the electrostatic RF ionization processes when ions and electrons are travelling across the plasma sheath region. Other peaks in the above two figures are thought to represent either ions whose motions are modulated by the plasma potential fluctuation when they pass across the plasma sheath or which are produced by a

large induction electric field (15 V/cm) existing in the plasma sheath. It must be noted that both the DC electric field in figure 3.9 measured by the emissive probe and the RF electostatic field (1 V/cm) in figure 3.10 measured by capacitive field probe are much smaller compared with the induction RF electric field (shown in figure 3.11) measured by magnetic probe. The induction RF field maintains ICP and may produce the inductive ionization processes near the glass wall where the electron density shown in figure 3.5 is falling but the induction field is increasing.

Furthermore, as shown in table 2.2, the estimated plasma potentials from IVDFs are fairly comparable with those data obtained from an emissive probe and a bolometric probe. In practice, the maximum operating pressure in argon ICP did not exceed 30 mtorr and the input RF power did not exceed 200 W. Measured maximum ion energy at various condition was less than 40 eV. This working environment guarantees that the effective ion-neutral collisions within the analyser could be ignored [55] and the secondary electron emission from the analyser owing to the bombardment of high energy ions is excluded.

Finally, the ion energy distribution functions (IEDFs) can be derived from measured IVDFs as follows,

$$IEDF = \frac{dN}{dE} = \frac{dN}{Mvdv} = \frac{IVDF}{Mv} = \frac{IVDF}{\sqrt{2eM(V_p - V)}} \tag{3.18}$$

here, dN represents the number of ions which energy equals lies between E and $E+dE$, v is ion velocity with kinetic energy E, and V_p is the plasma potential. Some of derived IEDFs from figure 3.13 and figure 3.14 are shown in figure 3.15, 3.16,

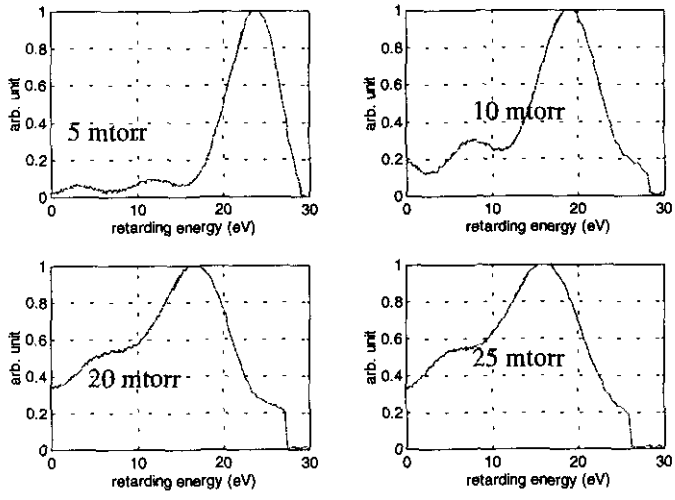

Figure 3.15 Measured IEDFs vs gas pressure in ICP . RF input was 100 W. The retarding energy analyser was mounted in the wall at the z=0 plane

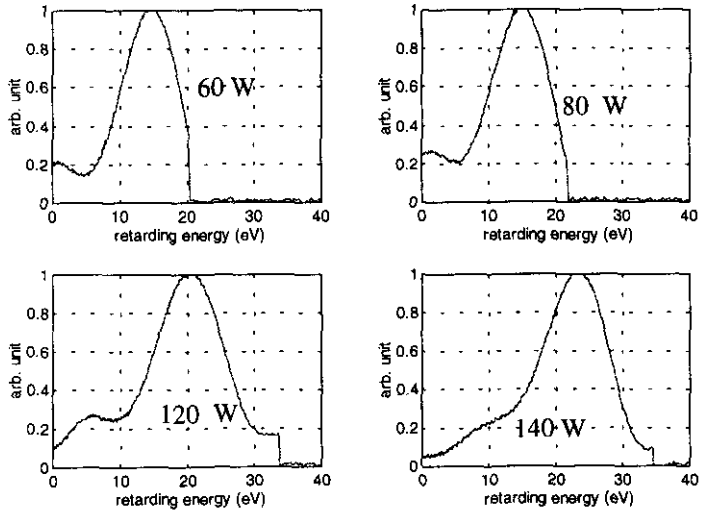

Figure 3.16 Measured IEDFs vs RF input power. Ar pressure = 10 mtorr. The retarding energy analyser was mounted in the wall at the z=0 plane. These IEDF's are total IEDF (no mass selection)

As seen from the above figures, the ion current is stopped when the retarding potetnial on the collector is increased to the local plasma potential. The derived plasma potential is more sensitive to RF input power rather the discharge gas pressure. Furthermore, the low energy ions due to inductively ionization were observed. Finally, typical measured Ar^+ IEDFs along the z direction measured by the Hiden EQP are shown as follows:

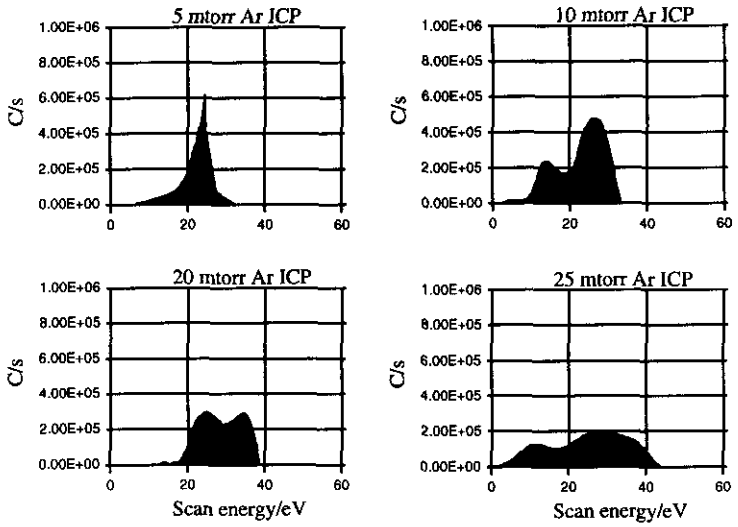

Figure 3.17 Ar^+ IEDFs of an 100W Ar ICP at various gas pressure from EQP system

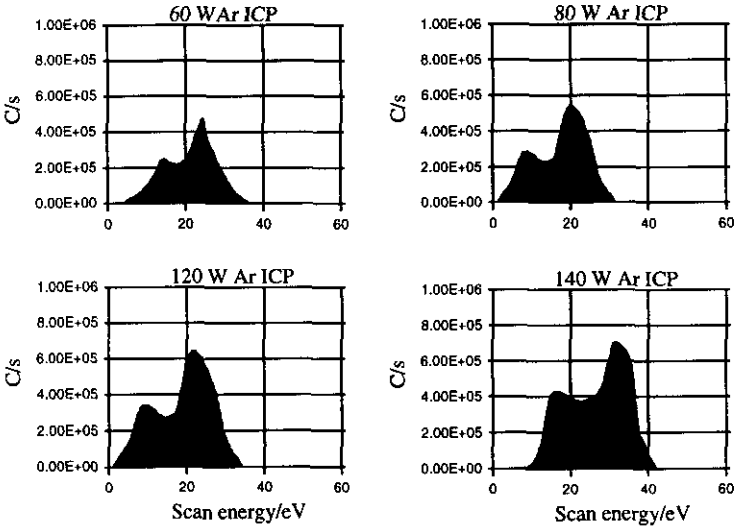

Figure 3.18 Ar^+ IEDFs of an 10 mtorr Ar ICP at various RF power level from EQP

The above IEDF's show the same basic trends as those in figure 3.15 and figure 3.16. The measured local plasma potential by Hiden EQP system is roughly a factor of 1.5 bigger than that measured by the retarding energy analyser. It is important to note the different location of the two ion distribution monitors (IVDFs were measure measured at r=8 cm, z=0, while IEDFs were sampled at r=0, z=18 cm). The local plasma density on the sheath edge around Hiden EQP probe is much smaller than that near retarding energy analyser, therefore the plasma sheath length may be comparable with ion-mean-free-path. As a result, unlike the situation in figure 3-15 and 3-16, it is believed that the saddle shapes of IEDF in figure 3-17 and 3-18 are either due to various ion collision processes, such as *ion-neutral elastic and resonant-charge-exchange collision [5] effects* or RF plasma potential fluctuation effects [65]. Further theoretical models and experimental investigation will pave a way to careful control and modification of the IVDFs or IEDFs for a high density, low pressure inductively coupled plasma for application of an advanced surface processing industry.

In the next chapter, using the above experimental data, we are going to study some electromagnetic characteristics in a high density, low pressure inductively coupled plasma, in order to understand the operation of the ICP in detail.

Chapter 4 Modelling of an inductively coupled plasma

4-1 Introduction

The modelling of the electromagnetic properties of low pressure inductively coupled plasmas (ICPs) has been intensified since the 1980s, mainly owing to the promising needs of the semiconductor processing industry, such as material etching and film deposition [5, 8]. A one-dimensional model of inductively coupled plasma confined in a cylindrical chamber was presented by Thomson (1927) [66]. He computed expressions for the electromagnetic fields assuming constant electron density across the discharge volume. Eckert (1961) [67] used Bessel functions for the fields by including the averaged value of the electron density in Maxwell's equations, and a 'Schottky' ambipolar diffusion radial profile (Schottky (1924)) [68] for the electron density to compute power deposition and impedance in these low pressure discharges. Henriksen et al (1971) [69] found a closed-form solution for the electromagnetic fields assuming a parabolic density profile. Denneman (1990) [21] modelled the discharge using a Schottky density profile again to solve the coupled Maxwell's equations numerically. More recently, Lister et al (1992) [26] also assumed a Bessel function electron density profile and used the space averaged conductivity in Maxwell's equations and obtained some plasma properties for 1-D cylindrical, inductively coupled discharges. Also, Piejak et al (1992) [27] used one-turn secondary of an air-core transformer model, considering only space-averaged plasma properties; they tried to present a practical design and optimization tool for a plasma

processing source based on an inductively discharge. Turner (1993) [29] presented a 1-D simulation and analysis of the electron heating processes in an inductively coupled discharge.

A two-dimensional analytical model of an inductively coupled plasma was proposed by Haas et al (1993) [62]. They solved Maxwell's equation following Thomson's assumption, and then used magnetohydrodynamics (MHD) fluid equations to model a low pressure inductively coupled plasma. The time-averaged electrostatic potential was shown to rise sharply toward the wall under some circumstances. A two-dimensional hybrid model of ICP for etching set up by Ventzek et al (1993) [4] was focused on a flat coil inductively coupled discharge device. Their two-D(r, z) model consists of an electromagnetic module, an electron Monte Carlo simulation, a hydrodynamic-chemical kinetics simulation, and an off-line plasma chemistry Monte Carlo simulation. They began with the EMM by calculating the coil-generated electric and magnetic field through finite difference method of successive-over-relaxation (SOR), then following Sommerer & Kushner (1992) [70], they completed hydrodynamic-chemical kinetics simulation, and feedback the time-averaged plasma conductivity (i.e. electron density profile information) into electromagnetic module to iterate toward a solution. This was the first attempt to find a self-consistent 2-D electromagnetic field in an inductively coupled plasma. Most recently, a two-dimensional analytic model by V. Vahedi et al (1995) [71] for the whole collisional regime has been developed to describe power deposition in a plane-coil-excited inductively-coupled plasma source. Note, the experimental device studied here is

the cylindrical coil and the differences in coil geometry can have strong effects on the overall plasma structure.

In the following section, we introduce the basic plasma equations used in this thesis. Then in section 4.3, after consideration of plasma-wall boundary condition for the experimental device, we are able to develop an electromagnetic module into an inductively coupled plasma excited by a traditional external coil including earthed screens. In section 4.4, we will find the electromagnetic field using a measured plasma density profile. Finally, the theoretical predictions are compared with experimental results reported in the previous chapter.

4-2 Basic plasma equations

As mentioned in chapter 1 and chapter 2, Maxwell's equations in a low temperature low pressure plasma are as follows,

$$\nabla \times \underline{E} = -\frac{\partial}{\partial t}\underline{B} \tag{4.1}$$

$$\nabla \times \underline{B} = \mu_0 \underline{J} + \mu_0 \varepsilon_0 \frac{\partial}{\partial t}\underline{E} \tag{4.2}$$

$$\nabla \bullet \underline{E} = \frac{\rho}{\varepsilon_0} \tag{4.3}$$

$$\nabla \bullet \underline{B} = 0 \tag{4.4}$$

where μ_0, ε_0 is the permeability and permittivity constant in free space, respectively, and $\underline{B}$ the magnetic field vector, $\underline{E}$ the electric field vector, $\underline{J}$ the conduction current vector, and ρ the net charge density.

One approach to solve the above equations is to take the conduction current and net charge as given, and introduce concepts of vector potential as mentioned in chapter 2. The general solution of equations (4.1-4) are as follows,

$$\underline{B} = \nabla \times \underline{A} \tag{4.5}$$

$$\underline{E} = -\frac{\partial}{\partial t}\underline{A} - \nabla\phi \tag{4.6}$$

where $\underline{A}$ indicates the vector potential, ϕ is the electrostatic potential. These in turn satisfy following equations,

$$\nabla^2 \underline{A} - \varepsilon_0\mu_0 \frac{\partial^2}{\partial t^2}\underline{A} = -\mu_0 \underline{J} \tag{4.7}$$

$$\nabla^2\phi - \varepsilon_0\mu_0 \frac{\partial^2}{\partial t^2}\phi = -\frac{\rho}{\varepsilon_0} \tag{4.8}$$

$$\text{and } \nabla \bullet \underline{A} = -\varepsilon_0\mu_0 \frac{\partial}{\partial t}\phi \tag{4.9}$$

Furthermore, the first moment of Boltzmann equation (1.6) yield the charge cloud force equation (4.10) [5],

$$m_e n_e \frac{d\underline{V}_e}{dt} = -en_e(\underline{E} + \underline{V}_e \times \underline{B}) - \nu_e m_e n_e \underline{V}_e - kT_e \nabla n_e \tag{4.10}$$

where the first term on RHS is the Lorentz force on electron fluid, the second is the frictional force due to the effective electron collision processes, and the last term

represents the electron pressure. Here m_e is electron mass, e is the electron charge, and n_e is the electron density, k is Boltzmann constant, T_e is the electron temperature.

Finally, the electron current $\underline{J}$ is defined by equation (4.11)

$$\underline{J} = -en_e \underline{V_e} \tag{4.11}$$

4.3 Theory

4.3.1 ICP vector potential

To model the system shown in figure 2.2, we consider only inductive coupling to the plasma. It is assumed that the capacitive coupling effects have been screened out by the electrostatic screen, and this screen does not disturb the poloidal symmetry in the coordinate shown in figure 4.1,

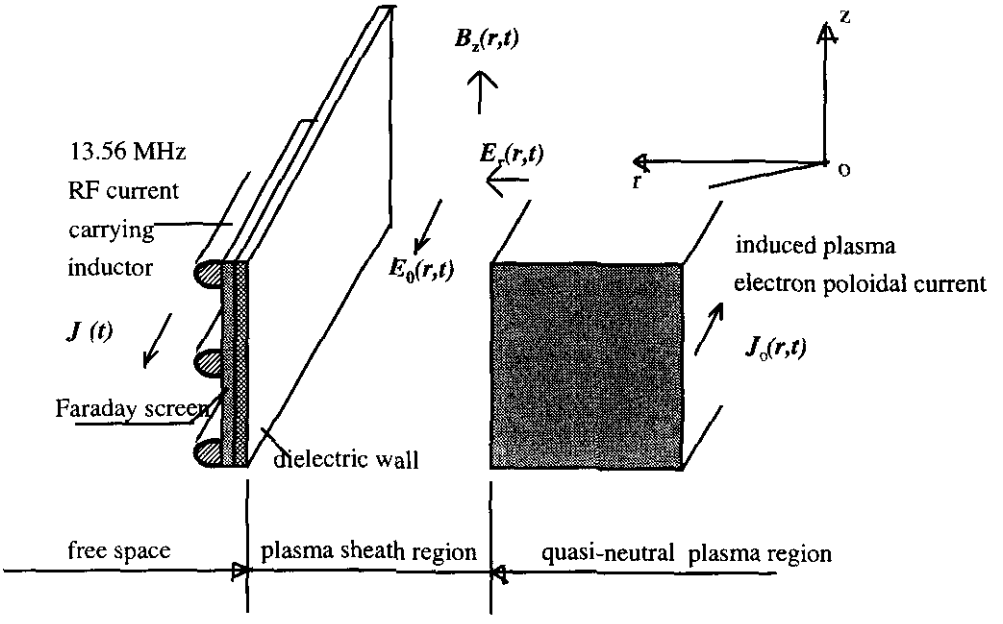

Figure 4.1 schematic coordinate for modelling of ICP

All the quantities here are assumed to be poloidally symmetric, ie, $\frac{\partial}{\partial\theta} \equiv 0$. In figure 4.1, the axial magnetic field $B_z(r,t)$ is supposed to be associated with an RF current through external coil, J, which excites a poloidal electric field $E_\theta(r,t)$. This in turn maintains the poloidal plasma electron current $J_\theta(r,t)$. A radial electrostatic electric field $E_r(r,t)$ is associated with the plasma-boundary (dielectric wall) requirement (i.e., the plasma presheath and sheath formation). The axial electric field has been assumed to be shorted by the electrostatic screen outside the chamber. Using basic vector operations as in appendix 2, the above assumptions lead to following simplified equations from equations (4.5), (4.6) and (4.7),

$$B_z = \frac{1}{r}\frac{\partial}{\partial r}(rA_\theta)$$
$$E_\theta = -\frac{\partial}{\partial t}A_\theta \tag{4.12}$$

$$\left(\frac{\partial^2}{\partial z^2} + \frac{1}{r}\frac{\partial}{\partial r} + \frac{\partial^2}{\partial r^2} - \frac{1}{r^2}\right)A_\theta - \varepsilon_0\mu_0\frac{\partial^2}{\partial t^2}A_\theta = -\mu_0 J_\theta \tag{4.13}$$

Due to the observation that the high harmonic component of RF field was found to be negligible compared with the fundamental RF field, we ignore RF harmonic wave effects in the current study (it should be noted that the harmonic effects could be treated in a parallel approach by means of Fourier transformation). We also assume that the poloidal vector potential is in complex spot frequency form of

$$A_\theta = A_0(r,z)\exp(j\omega t + j\Phi_A) \tag{4.14}$$

where ω is the RF angular frequency, both the amplitude A_0 and the phase factor are positive real functions of spatial position (r, z).

Substituting (4.14) in to (4.12-4.13), we find the solutions of the induction field as follows,

$$B_z = B_0(r,z)\exp(j\omega t + j\Phi_B) \tag{4.15}$$

where

$$\begin{aligned} B_0(r) &= \left[\left(\frac{\partial}{\partial r}A_0 + \frac{A_0}{r}\right)^2 + \left(A_0\frac{\partial}{\partial r}\Phi_A\right)^2\right]^{1/2} \\ \Phi_B &= \Phi_A + \tan^{-1}\left(A_0\frac{\partial}{\partial r}\Phi_A \Big/ \left(\frac{A_0}{r} + \frac{\partial A_0}{\partial r}\right)\right) \end{aligned} \tag{4.16}$$

and

$$E_\theta = E_0(r,z)\exp(j\omega t + j\Phi_E) \tag{4.17}$$

where

$$\begin{aligned} E_0 &= \omega A_0 \\ \Phi_E &= \Phi_A - \frac{\pi}{2} \end{aligned} \tag{4.18}$$

Moreover, from equation (4.16) and (4.18), the time averaged Poynting power vector coupled into plasma is found to be

$$\underline{S_r} = -\frac{1}{2}E_0B_0\sin\left\{\tan^{-1}\left[A_0\frac{\partial}{\partial r}\Phi_A \Big/ \left(\frac{A_0}{r} + \frac{\partial}{\partial r}A_0\right)\right]\right\} \tag{4.19}$$

Based on the above equations, table 4.1 shows how the phase distribution of vector potential affects the magnetic field phase distribution, induction field phase distribution and the RF power coupled into ICP when the amplitude of vector potential is given.

	case 1	case 2	case3
Φ_A	constant	increases as r increase	decreases as r increases
Φ_B	constant	increases as r increase	decreases as r increases
Φ_E	constant	increases as r increase	decreases as r increases
S_r	0, which is vacuum solution where no power exchange	<0 , which indicates that RF power flux flows into the ICP from external coil	>0, which means plasma outputs power to external device (e.g. fusion realized)

Table 4.1 effects of different phase distribution of vector potential

As it can be seen, the form of vector potential plays an important role in RF power coupling mechanism.

In the next section, we are going to find the physical meaning of the ICP vector potential and study the ICP electrostatic potential.

4.3.2 The time-averaged ICP electrostatic potential

The electrostatic RF space potential has been previously studied in chapter 2. Here we are going to study the time-average static potential along the radial direction.

According to equation (4.11), the poloidal conduction current can be written as

$$J_\theta = -en_e V_{e\theta} \tag{4.20}$$

where n_e is the local electron density, $V_{e\theta}$ is the poloidal electron drift velocity, given by the electron macroscopic motion equation (4.10), which leads to the following two equations for electron poloidal and radial force balances,

$$\frac{\partial}{\partial t} V_{e\theta} = -\frac{e}{m} E_\theta - \nu_e V_{e\theta} \tag{4.21}$$

$$-\frac{I}{r} V_{e\theta}^{\ 2} = -\frac{e}{m} E_r - \frac{e}{m} V_{e\theta} B_z - \frac{kT_e}{mn_e} \frac{\partial n_e}{\partial r} \tag{4.22}$$

Where e is the electron charge, m is the electron mass, t is time, ν_e is the effective electron collision frequency. In deriving (4.21) and (4.22), the electron radial drift velocity has been assumed negligible compared with the poloidal drift effect (it will be shown that this is a good assumption in chapter 5). It should be noted that near the glass wall, a small time averaged electron radial drift has to exist in order to satisfy the well known ambipolarity requirement [72], which in turn has to be determined by study of the ion radial motion [73-77]. Also, for a weakly ionized low temperature discharge plasma, the last term on the RHS in equation (4.22), the plasma density pressure force contribution, may have an important effect on the radial force balance in the plasma sheath region.

In chapter 2, it has been already noted that for a purely inductive discharge, the RF electrostatic potential should not vary in time very much. Experimental data in chapter 3 demonstrates the RF electrostatic field is less than 5 V/cm, which is negligible compared with measured large induction RF field 15 V/cm in a 100 W/10 mtorr argon ICP. Also the measured time average plasma potential shows the existence of a potential hill in the discharge chamber along the radial direction. We now explain this phenomenon by considering equations (4.16-4.22) as follows.

Using equations (4.12), (4.14) and solving equations (4.21) and (4.22) for the electron poloidal drift velocity and the time averaged radial electric field, leads to equation (4.23) and (4.24),

$$V_{e\theta} = \frac{e}{m}\frac{1}{\left(1 - j\frac{\nu_e}{\omega}\right)}A_\theta = \frac{e}{m}A_0\, exp(j\omega t + j\Phi_A + j\frac{\nu_e}{\omega}) \tag{4.23}$$

here $\frac{\nu_e}{\omega} << 1$ is assumed for a low pressure discharge. It is clear now that the ICP vector potential is associated with the electron drift velocity. The phase difference between them is proportional to the effective electron collision frequency.

$$\langle E_r \rangle = \frac{1}{2r}\frac{e}{m}A_0^{\,2}\left\{1 - \frac{rB_0}{A_0}cos\left(\Phi_A + \frac{\nu_e}{\omega} - \Phi_B\right)\right\} - \frac{kT_e}{en_e}\frac{\partial n_e}{\partial r} \tag{4.24}$$

here the bracket on LHS represent the time average process. Using equation (4.16), the above equation can be transformed into the following form,

$$\langle E_r \rangle = \frac{1}{2r}\frac{e}{m}A_0^{\,2}\left\{1 - \sqrt{\left[\left(1 + \frac{r\partial}{A_0\partial r}A_0\right)^2 + \left(\frac{r\partial}{\partial r}\Phi_A\right)^2\right]}cos\left(\frac{\nu_e}{\omega} - \Delta\right)\right\} - \frac{kT_e}{en_e}\frac{\partial n_e}{\partial r} \tag{4.25}$$

$$\text{here } \Delta = tan^{-1}\left[\frac{r\frac{\partial}{\partial r}\Phi_A}{1+\frac{r\partial}{A_0\partial r}A_0}\right] \tag{4.26}$$

As it can be seen from equation (4.25), based on the measured plasma density and electron temperature, if the ICP vector potential is known, the time averaged electrostatic electric field can be calculated numerically, and thus plasma potential distribution along radius can be derived by integral of $<E_r>$. Before starting to solve the plasma vector potential profile, it is interesting to do a little analytical analysis about possible trend in $<E_r>$, as listed in table 4.2, which shows special cases in bulk plasma where the electrostatic field and related plasma potential varies along the radial direction due to different ICP vector potential profiles.

	requirements	$\langle E_r \rangle$	plasma potential profile
case 1	$\frac{\partial ln(A_0)}{\partial r} << \frac{1}{r}, \frac{\partial \Phi_A}{\partial r} \approx 0$	$\langle E_r \rangle = \frac{1}{2r}\frac{e}{m}A_0^2\left\{1-cos\left(\frac{\nu_c}{\omega}\right)\right\} > 0$	V_p decreases as r increases
case 2	$\frac{\partial ln(A_0)}{\partial r} >> \frac{1}{r} >> \frac{\partial \Phi_A}{\partial r} > 0$	$\langle E_r \rangle = -\frac{1}{2}\frac{e}{m}A_0\frac{\partial}{\partial r}A_0 cos\left(\frac{\nu_c}{\omega}\right) < 0$	V_p increases as r increases
case 3	$\frac{\partial \Phi_A}{\partial r} >> \frac{\partial ln(A_0)}{\partial r} >> \frac{1}{r}$	$\langle E_r \rangle = -\frac{1}{2}\frac{e}{m}A_0\frac{\partial}{\partial r}A_0 cos(\Delta)$	depends on Δ and A_0

Table 4.2 Possible plasma potential solutions in ICP

4.3.3 Vector potential equation

Combining equations (4.13), (4.20) and (4.23), we obtain an equation for the vector potential,

$$\frac{\partial^2}{\partial z^2}A+\frac{\partial^2}{\partial r^2}A+\frac{1}{r}\frac{\partial}{\partial r}A-\frac{1}{r^2}A=KA \tag{4.27}$$

where

$$K=\left(\frac{\omega_{pe}}{c}\right)^2\left(1-j\frac{\nu_e}{\omega}\right)-\left(\frac{\omega}{c}\right)^2 \tag{4.28}$$

and $A=A(r,z)exp(j\Phi_A)$

Here c, which equals $\frac{1}{\sqrt{\varepsilon_0\mu_0}}$, is the speed of light; ω_{pe}, the plasma frequency, is given by (1.19), which is a function of the local plasma density $n(r,z)$. It is now concluded that the ICP vector potential could be found by solving equation (4.27) numerically, provided that boundary conditions of $A(r,z)$, the RF frequency, the effective electron collision frequency, and the plasma density profile are known. Once the vector potential is given, the induction electric field, magnetic field, Poynting power vector, and the radial electrostatic field can be calculated from equations (4.15-4.26), respectively.

To solve equation (4.27) numerically, a finite-element analysis approach was adopted in this study. A mathematical grid (2M rows and 2N columns) columns is set into the cylindrical discharge chamber as follows:

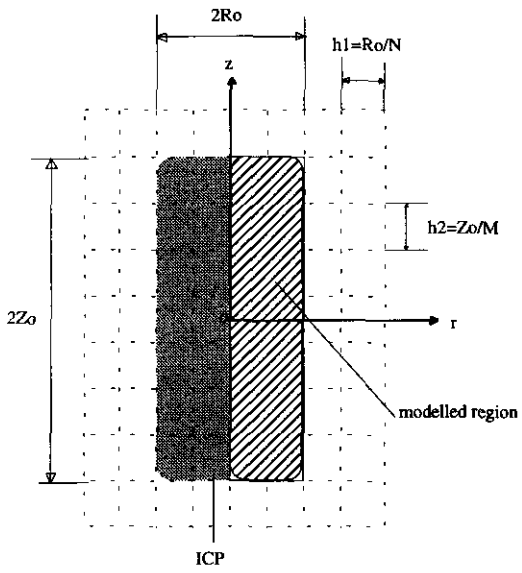

Figure 4.2 a mathematical spatial grid used to digitise the real continuous space. Here $2Z_0$ equals the height of the Faraday screen, $2R_0$ is the internal diameter of chamber.

In principle, any order derivatives of $A(r,z)$ with respect to space can be worked out provided that the mesh size is chosen properly, in order to avoid non physical smoothing effects or other instabilities. The details of this finite element analysis by using Matlab software [78] are listed in appendix 3. Boundary values at the edge of the plasma are considered as follows:

At the edge of Faraday screen, the plasma density is so weak that the first term on RHS of equation (4.28) is much smaller than the second term, and the z dependence of A can be ignored compared with the r dependence. In other words,

$$K \approx \left(\frac{\omega}{c}\right)^2 \tag{4.29}$$

$$\frac{\partial^2}{\partial z^2} A << \frac{\partial^2}{\partial r^2} A \tag{4.30}$$

An approximate solution for equation (4.27) by use of the above two assumptions is found to be

$$A \propto J_1(\frac{\omega}{c} r) \approx A_0 \frac{r}{R_0} \tag{4.31}$$

where J_1 indicates the first order Bessel function of first kind [40]. Hence, the boundary condition at the edge of Faraday screen is determined as,

$$A(r, \pm Z_0) = A_0 \frac{r}{R_0} \tag{4.32}$$

Moreover, at the centre of discharge chamber, it is physically anticipated that no induction RF field exists, thus

$$A(0, z) = 0 \tag{4.33}$$

Furthermore, near the glass wall, a uniform vector potential was assumed around the Faraday screen, hence,

$$A(R_0, z) = A_0 \tag{4.34}$$

In the above three expressions, A_0 is a constant.

Given P_{in}, the fixed input RF power to the discharge chamber and a measured plasma density profile, equation (4.27) can be solved using the method of successive-over-relaxation [79]. The solution is considered to have converged if the relative difference of $A(r,z)$ at every mesh point in the modelled region after 30 successive iterations, is such that $\frac{\Delta A}{A} \leq 10^{-3}$. Using the given plasma density profile, from equation (4.27), we are then able to find this distribution of $A(r,z)$ with the value of A_0 and a constant-electron-neutral

collision frequency. The electric field, magnetic field and plasma conduction current, power dissipation in plasma and the radial electric field can then be found from equations (4.16-4.26) respectively. Using the parallel approach of reference [4], the next step is to adjust A_0 and solve $A(r,z)$ again, until power dissipated in the chamber (see equation (1.24)) is equal to the total input RF power.

A schematic of this ICP EM model is shown as in the following flow chart,

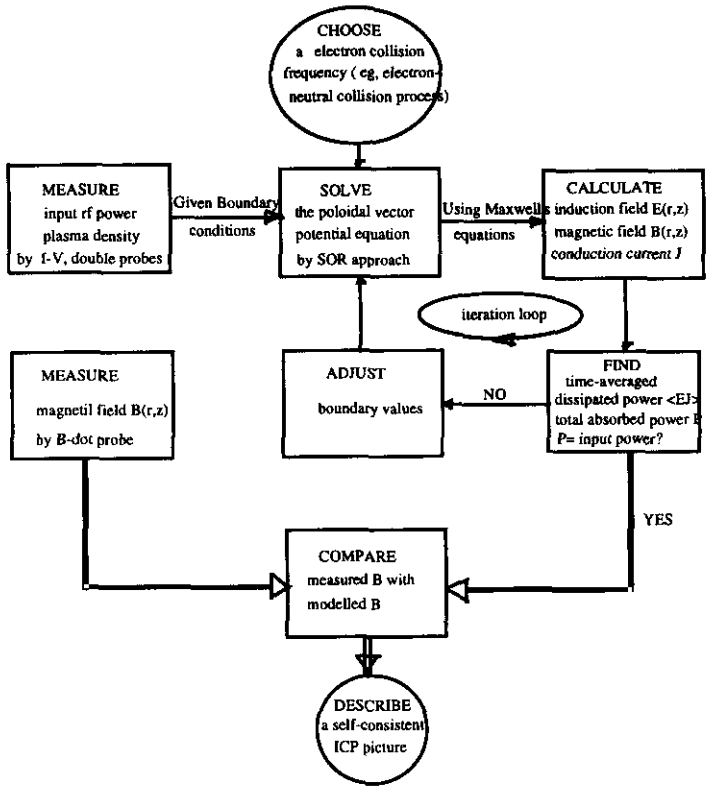

Figure 4.3 Flow chart of modelling ICP

4.4 EM simulations and discussions

Given a measured plasma density distribution in the discharge chamber, an electron effective collision frequency profile (including gas pressure factor), EM simulations are achieved by solving equations (4.16-4.26) accordingly. To take an example of modelling a 100 W/10 mtorr Ar inductively-coupled plasma, one proceeds as follows:

Firstly, based on measured plasma density profiles shown in figure 4.4,

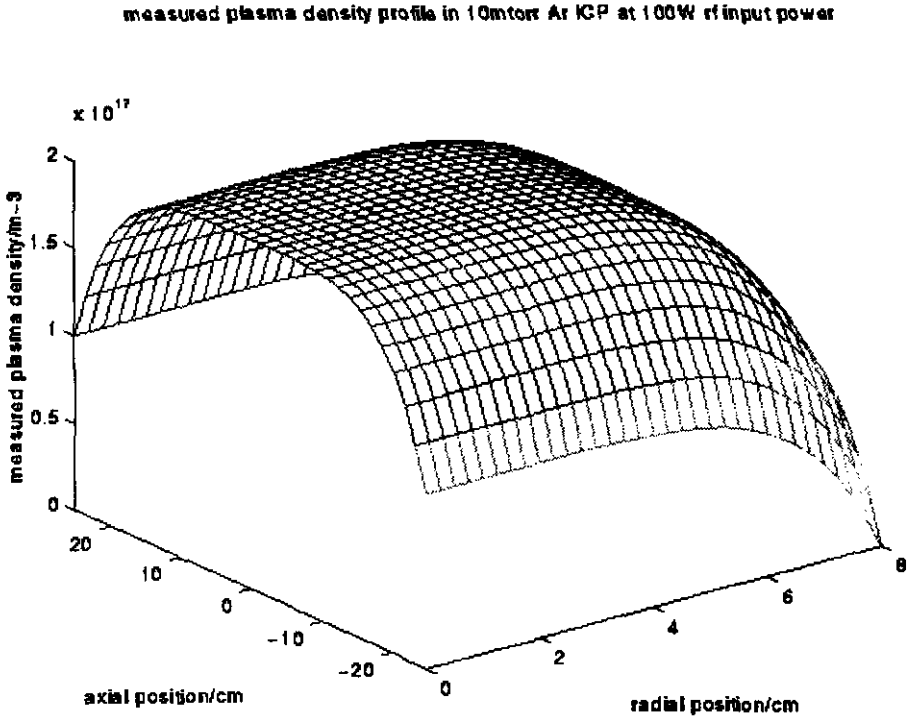

Figure 4.4 input plasma density profile measured by a Langmuir double probe. The measured electron temperature was roughly 2.5 eV on average, in the discharge chamber.

Secondly, given the effective electron collision frequency 1×10^{7} S^{-1} in 10 mtorr argon gas, we solve equation (4.27) for an initial guess of $A_0=10^{-5}$ sV/m. The corresponding

electromagnetic field and calculate the power absorbed by the plasma is found. This turns out to be only 60% of the input RF power of 100 W. Then, the next step similar to the approach used in [4], is to increase value of A_0 by a factor of 1.1, and solve equation (4.27) again. Finally, after several iterations, the electromagnetic parameters which enable the RF power absorbed by the plasma to equal the input RF power are obtained. Figure 4.5 shows the ICP vector potential distribution.

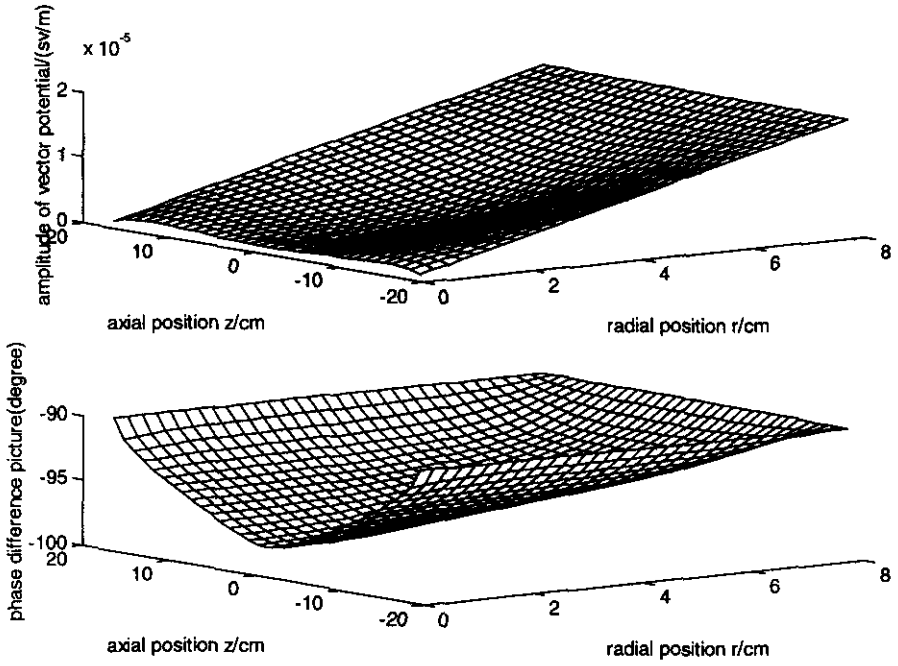

Figure 4.5 plasma vector potential A(r,z) distribution

From the above figure, it can be recognised that the ICP vector potential in this study satisfies the requirements of case 3 in table 4.1 and case 2 in table 4.2. Thus, it should be anticipated that time averaged Poynting vector is negative, namely its direction is pointing inward along radial direction, and the time averaged plasma potential should have an " uphill " trend along radial direction as shown in figure 3.9 experimentally. This

feature will be analysed later on. The corresponding magnetic field from equation (4.16) is shown in figure 4.6.

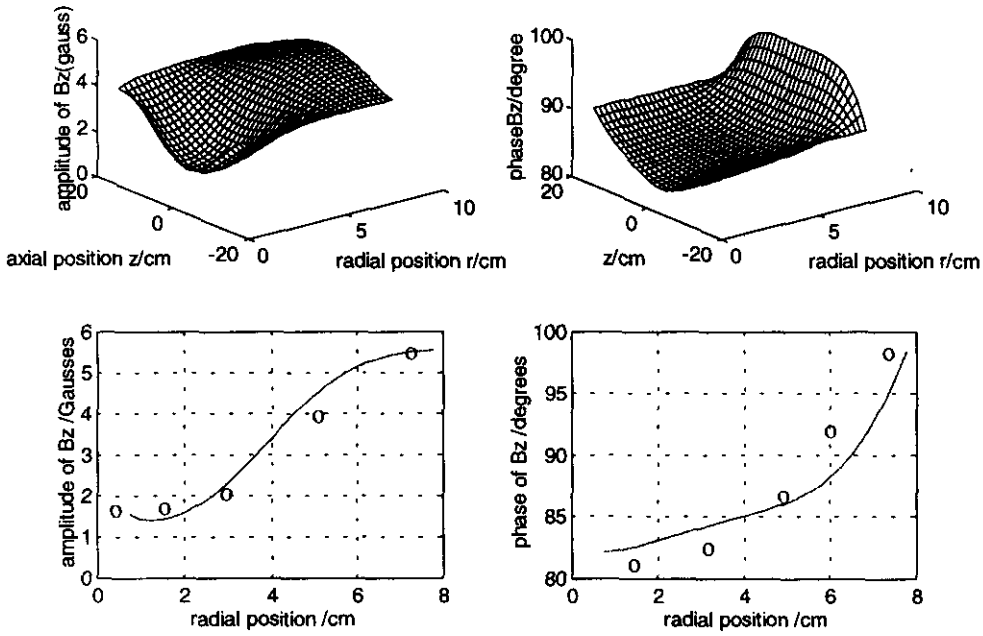

Fgiure 4.6 Magnetic field distribution. Here solid line is simulated trend, which is being compared with the experimental data marked by circles from figure 3.12 for 100 W/10 mtorr ICP.

As it can be seen, a reasonable agreement is the observed in the basic trends both in magnitude and phase of magnetic field. The derived induction electric field is presented in figure 4.7 as follows,

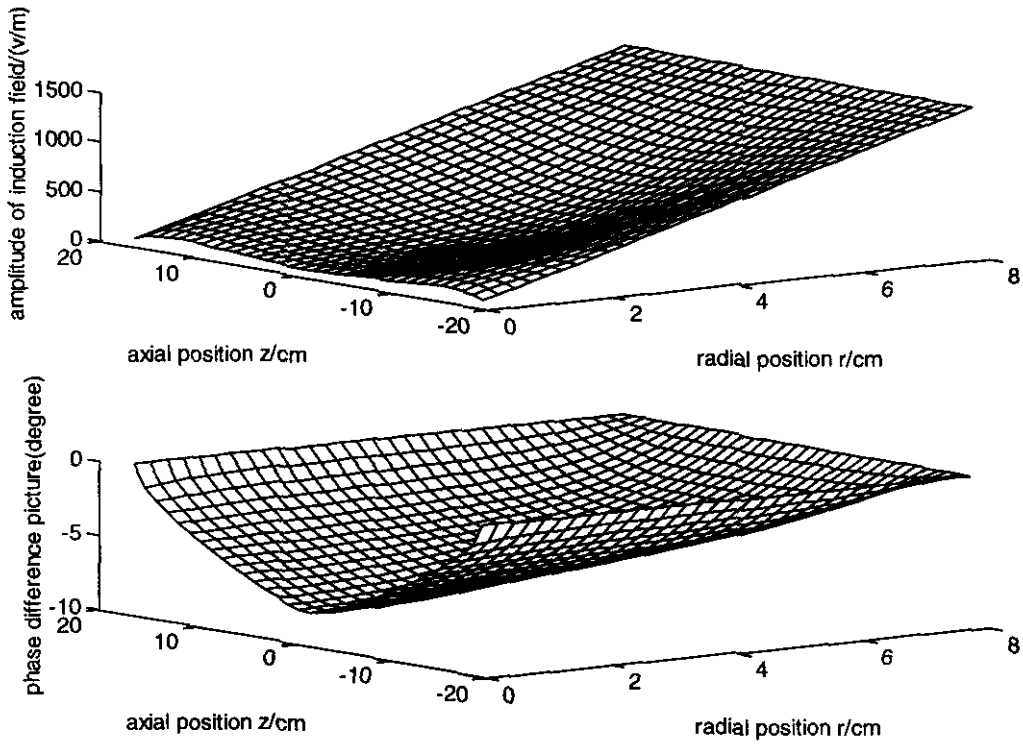

Figure 4.7 Simulated induction electric field in a 100 W/10 mtorr argon ICP

As can be seen, the simulated induction electric field is roughly a linear function of radial position and fairly comparable to the data shown in figure 3.12.

The simulated conduction current density profile in 100 W /10 mtorr ICP is shown the following figure,

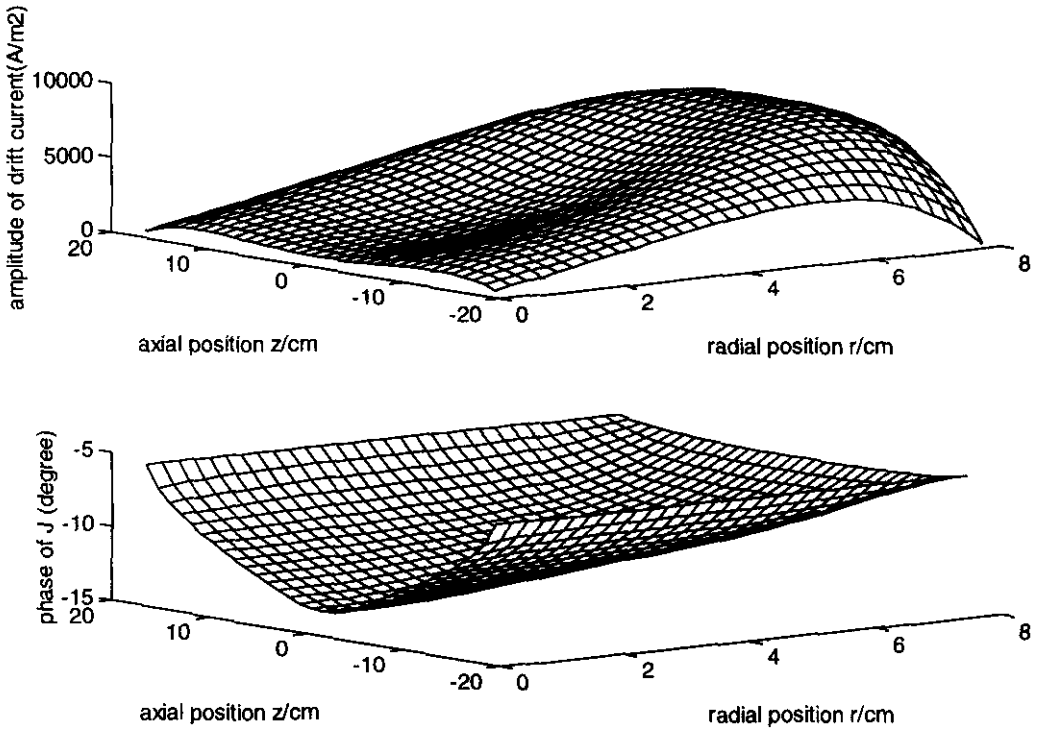

Fgiure 4.8 Simulated electron polidal drift current density distribution

As can be seen, the simulated electron current density reaches its maximum near the glass wall, as it should, since the induction electric field increases toward to the wall and the induced electron drift motion intensifies there. However, around the wall, because the electron density reduces sharply as shown in figure 4.4, the electron drift current density defined by equation (4.11) reduces as illustrated here exactly.

Figure 4.9 shows the simulated electron poloidal drift velocity distribution.

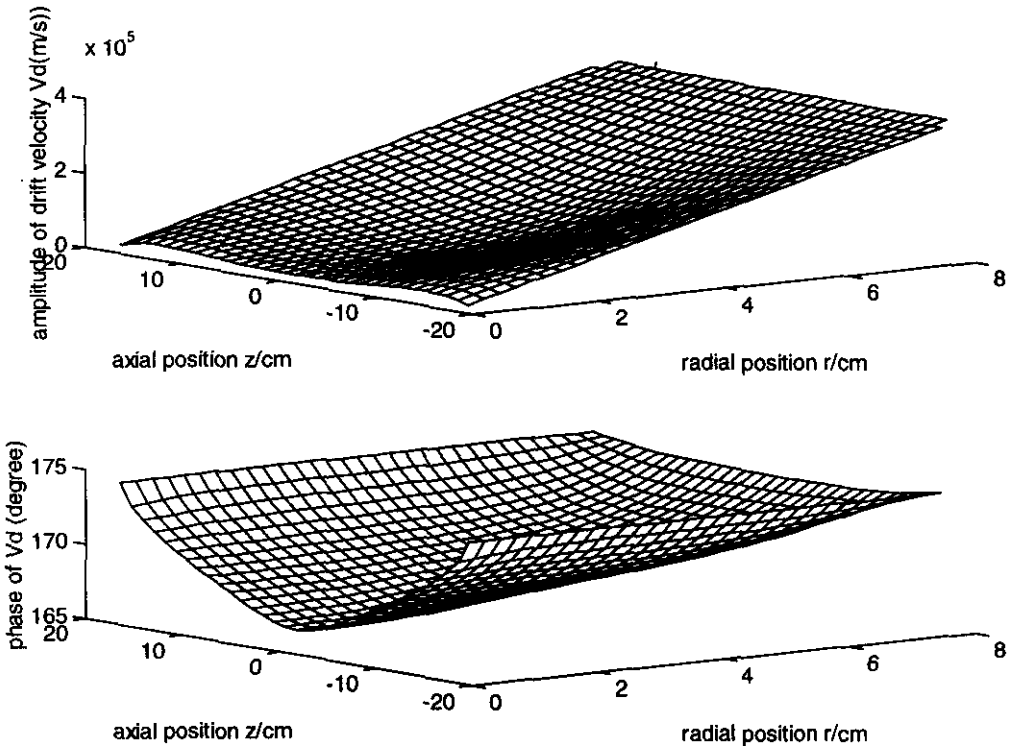

figure 4.9 Simulated electron poloidal drift velocity distribution

As can be seen, near the glass wall, the simulated electron poloidal drift velocity (4×10^5 m/s) is comparable to the electron thermal speed defined in equation (1.10), that is the order of 10^6 m/s for kT_e at 2.5 eV (see table 2.1). Hence near the wall, EEDF in ICP may be a drift-Maxwellian distribution. This phenomenon may produce some problems in Langmuir double probe interpretation of the ICP's parameters near the glass wall, since equations (1.19) and (2.20) are no longer valid in the presence of large drift conduction current near the Langmuir double tips. It should be studied in the future works. Some interesting observations of non-Maxwellian EEDF in ICPs have been reported by Kortshagen et al (1994) [80], Mahoney et al (1994) [81], and Lai et al (1995) [82].

Figure 4.10 shows the calculated dissipated RF power density profile and the simulated time averaged Poynting vector in the plasma.

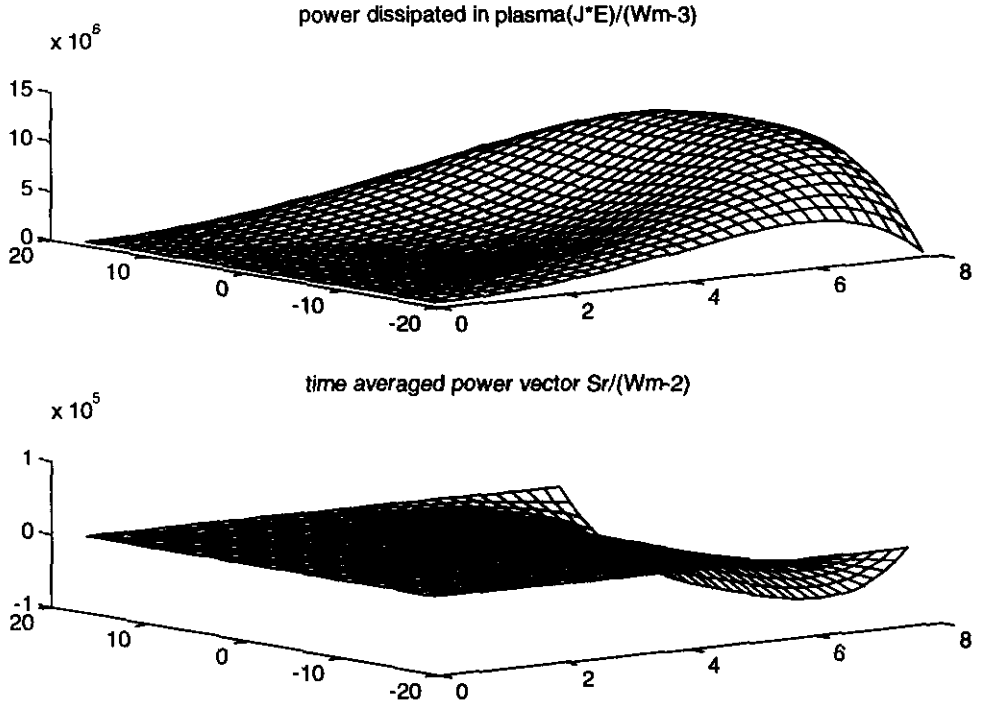

Figure 4.10 Simulated dissipated RF power density profile and the time averaged Poynting vector in the plasma

As can be seen, the simulated data compares well to the measured and derived results shown in figure 3.12. Also, it shows that the RF power is inductively coupled into the chamber and is dissipated near the glass wall (1-2 cm away), as it is expected from discussion in previous sections.

The simulated time averaged radial electric field distribution is presented and compared with the experimental data in figure 4.11,

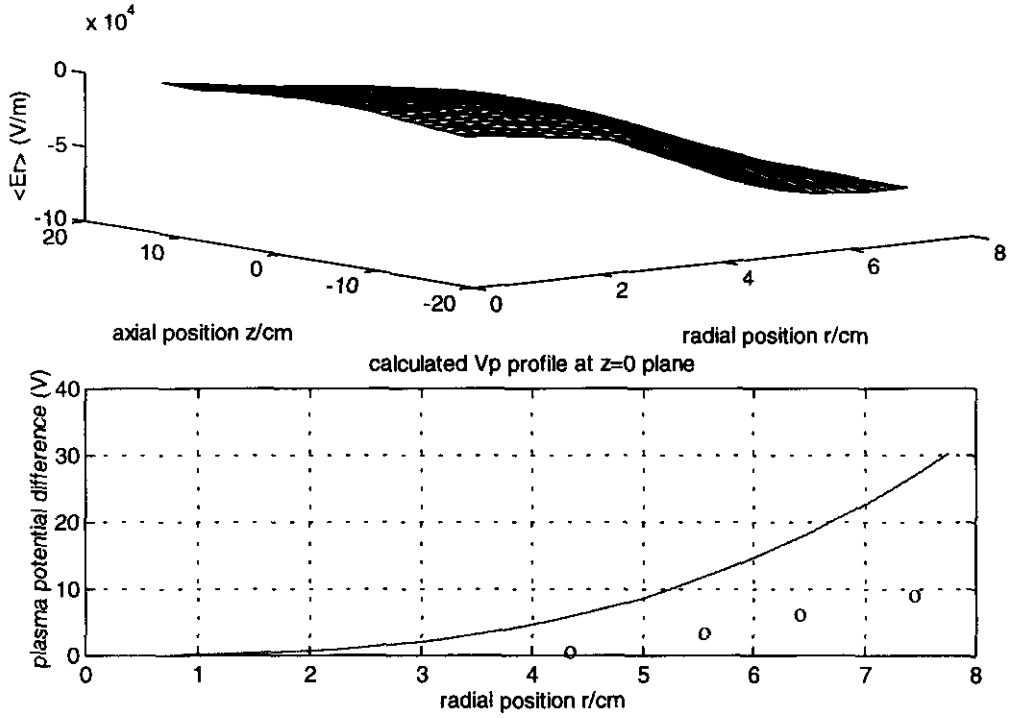

Figure 4.11 The simulated time averaged radial electric field distribution. Here the modelled plasma potential profile (the solid line) is compared with the measured profile marked by circles data taken from figure 3.9.

As it can be seen, both simulated result and experimental data show an upward potential trend as the radius increases. However, an obvious difference is seen near the glass wall. This may be due to the following reasons: (1) the current model ignores the radial and axial motion of the charge in the overall plasma force balance, (2) a self-consistent plasma density profile is not available to be used in the solving vector potential equation (4.27), (3) the lack of presheath and sheath theory in the current ICP study hinders the determination of the induction field boundary conditions of equation (4.27), (4) the effective electron collision frequency may not be a constant, it may be influenced by the

RF field, and may have to include a stochastic collision factor [5]. Those factors should be the main objectives in future theoretical analysis of an ICP.

Furthermore, from the above simulation results, it can be seen now that the RF induction field, magnetic field, plasma conduction current are radially increasing toward the glass wall. This is due to the induced plasma " thin layer " current always going in the opposite direction to the external RF conduction current flowing through the inductor [5], and therefore, the total RF field in the centre part of plasma is reduced according to Maxwell's equations.

In summary, based on measured profiles of plasma density and electron temperature, and given some initial assumptions, the RF vector potential, the electric field, the magnetic field, the dissipated RF power, and the plasma electrostatic potential profile have been successfully modelled and predicted by solving Maxwell's equations and electron fluid equation. The derived RF vector potential equation for a cylindrical geometry has for the first time been numerically solved. The finite-element analysis approach in this study can be applied to other geometries too. Good agreement between the simulations and the diagnosed plasma parameters has been demonstrated in this study. In the next chapter, we will try to explain the form of electron, ion radial drift motion, and present an ICP density profile, which will be compared with the input plasma density profile used in the simulation.

Chapter 5 Further considerations and conclusions

5.1 Introduction

The grand challenge for the plasma theorists is to produce a model which contains a complete understanding of the processes which initiate, sustain and disrupt the plasma and which thus contains information about the concentration of the electric charge carriers and their behaviour. There are several approaches to model a plasma. One is to write down all the equations (kinetic or fluid theory) which describe the plasma, basically electromagnetic and statistical. The direct solving of them needs the experimental measurements to set the boundary conditions, as shown in chapter 4. Another approach is to make a number of assumptions until an analytical solution can be found. This analytical approach can be used to gain insight into the major physical processes in the plasma and allows the common features of different plasma to be identified as we did in chapter 4 in describing the electron poloidal drifting motion, the ICP vector potential and the plasma potential profile along radial direction. In this chapter, we study some physics phenomena associated with electron and ion motion in a low temperature inductively coupled plasma. A model for ICP density distribution will be compared with other theories. The work and conclusions of this study are summarised at the end.

5.2 Electrons drift motion in ICP

It is well known that an ion-acoustic wave can be launched into plasma by applying an RF voltage waveform to an electrode immersed in a plasma [77]. Considering the case of RF inductively coupled plasma, we are going to show that the induced plasma electron poloidal drift motion in chapter 4 will significantly modify the characteristics of ion radial motion and affect the IEDFs through various collision processes.

By applying an RF voltage waveform to an electrode in a plasma, the space-charge sheath adjacent to the electrode can be caused to expand or contract, hence the plasma density can be modulated through the ion acoustic wave propagation. In an inductively coupled plasma, in order to maintain an induced RF conduction current, either the plasma density or charged particle velocity has to be modulated by the external electromagnetic field. Owing to the collective behave of the plasma, the electron drift motion logically leads to the modification of ion motion. Normally the ion motion along the RF field direction is regarded as small enough to be ignored in modelling of ICPs [21, 24, 27, 29], mainly owing to the insensitivity of ions to high frequencies. In modelling of capacitively coupled plasma, which has relatively low density compared with ICPs, the steady ion assumption is a good assumption [5], provided that the plasma ion frequency is much smaller than that of external RF field. However, the plasma density in this study is of the order of $10^{17} m^{-3}$ or even higher for an inductively coupled plasma excited by RF 13.56 MHz, hence, ions in the ICP do respond to the RF fluctuations. This was experimentally

confirmed by the observed IEDFs in chapter 3, in which ion energy up to nearly 30 eV was monitored near the glass wall for a 100 W/10 mtorr argon ICP.

The ion radial motion must be connected with electron radial motion, in order to satisfy the ambipolarity requirement [68] as mentioned in chapter 4. In this chapter, the electron fluid motion equation (4.10) is written in the following exact form (see appendix 2),

θ direction $$\frac{\partial}{\partial t}V_{e\theta}+V_{er}\frac{\partial}{\partial r}V_{e\theta}+\frac{1}{r}V_{er}V_{e\theta}=-\frac{e}{m_e}E_{\theta}+\frac{e}{m_e}V_{er}B_z-\nu_e V_{e\theta} \tag{5.1}$$

r-direction $$\frac{\partial}{\partial t}V_{er}+V_{er}\frac{\partial}{\partial r}V_{er}-\frac{1}{r}V_{e\theta}{}^2=-\frac{e}{m_e}E_r-\frac{e}{m_e}V_{e\theta}B_z-\frac{kT_e}{m_e}\frac{\partial}{\partial r}(\ln n_e)-\nu_e V_{er} \tag{5.2}$$

Here, e is the electron charge, m_e is the electron mass, other quantities have their normal meanings. The first term on the RHS of (5.2) is the electrostatic force term. The second term is the Lorentz force effect, while the third one indicates the electron pressure force along radius and the last term represents the effective electron collision contribution.

Furthermore, in the case of non-relativistic electron drift motion in 13.56 MHz electromagnetic fields, we assume that the plasma effective electron energy in the drift fluid can be given by the Lagrangian function [83] as follows:

$$\mathrm{E}_{eff}\approx L=-e\phi+\frac{1}{2}m_e\left[V_{e\theta}{}^2+V_{er}{}^2\right]-eV_{e\theta}A_{\theta} \tag{5.3}$$

where $\phi=-\int E_r dr$, represents the radial electrostatic potential, and $A_\theta=-\int E_\theta dt$ implies the induction vector potential.

We also assume a relation for an inductively coupled plasma, which physically means that electron tends to stay in the lower energy state,

$$n_e = n_0 \, exp\left\{-\frac{E_{eff}}{kT_e}\right\} \tag{5.4}$$

Where n_0 is the electron density where the effective electron energy equals zero, k is the Boltzmann constant, and T_e is the electron temperature. From equation (5.2) and (5.4), it can be straightforwardly seen that in the absence of RF induction field, equation (5.4) becomes the well known Boltzmann's relation for a capacitively coupled plasma [5].

Using the plasma vector potential form rather induction electric field and magnetic field expressions, namely, substituting equation (4.12) into equation (5.1), the electron poloidal drift velocity is found

$$V_{e\theta} = \frac{e\omega}{m_e(\omega - j\nu_e)} A_\theta \tag{5.5}$$

It is interesting to note this is exactly the same expression as equation (4.23). Combining expressions (5.3-5.5) together, leads to

$$n_e = n_0 \, exp\left\{\frac{e\phi - \frac{1}{2}m_e V_{er}^{\,2} - \frac{e^2}{2m_e}A_\theta^{\,2}}{kT_e}\right\} \tag{5.6}$$

In deriving (5.6), $\nu_e << \omega$ is assumed again. Substituting (5.6) into equation (5.2), leads to an expression for electron radial motion as follows,

$$V_{er} = -j\frac{e}{m_e\omega}V_{e\theta}\left(\frac{A_\theta}{r} + \frac{\partial}{\partial r}A_\theta\right) \approx -j\frac{e}{m_e\omega}V_{e\theta}\frac{\partial}{\partial r}A_\theta \tag{5.7}$$

In deriving (5.7), the plasma vector potential is assumed to satisfy the requirement of case 2 in table 4.2. It is interesting to note that:

(1) the derived electron radial drift will have the first harmonic RF component if the plasma vector potential is given by equation (4.14), and therefore the RF current in external circuit may have harmonic component as well due to this electron radial motion,

(2) a little algebra work shows that

$$\left|10\log\frac{V_{er}}{V_{e\theta}}\right| = 10\log\left|\frac{e}{m_e\omega}\left(\frac{\partial}{\partial r}A_\theta\right)\right| \approx -20 \text{ dB} \tag{5.8}$$

for a 100 W/10 mtorr argon ICP reported in chapter 4. This analysis leads to an excellent theoretical support to the experimental observation, in which the RF harmonic component in external electric circuit is less than 20 dB.

(3) Using equation (4.14) and (5.5), the time averaged electron radial velocity can be derived to be,

$$\langle V_{er}\rangle = -\frac{e}{2m}A_0\left(\frac{\partial}{\partial r}A_0 + A_0\frac{\partial}{\partial r}\Phi_A\right)\cos\frac{\nu_e}{\omega} \tag{5.9}$$

where A_0, Φ_A is the amplitude and phase factor of plasma vector potential respectively. Both of them may be a function of *(r, z)*. For the case 2 in table 4.2, it is straightforward to know that (5.9) is negative, as it should, because the induced plasma current is forced to move away from the external RF current carrying inductor [61]. Moreover, it is worth mentioning that for an argon ICP reported in this study, the time averaged electron radial drift velocity is reduced to zero at the centre of discharge chamber. It should be noted that a self-consistent electron motion picture has to be studied by a 3-dimensional fluid model, in order to explain electron flux along axial direction.

$$\frac{\partial}{\partial \tau}u + u\frac{\partial}{\partial X}u - \frac{\partial}{\partial X}\eta = -P_1, P_1 = \frac{m_e}{m_i}\frac{V_{er}}{C_s^{\,2}}\frac{\partial}{\partial X}V_{er} \tag{5.12}$$

$$\frac{\partial}{\partial \tau}\eta + u\frac{\partial}{\partial X}\eta - \frac{\partial}{\partial X}u = P_2, P_2 = \frac{\nu_{iz}}{\omega_{pi}} + \frac{u}{X} \tag{5.13}$$

The exact solutions of the above equations can be found numerically by employing a parallel approach adopted in [70, 71]. As it can be seen from above equations, the ions radial motion is influenced by electron radial drift and ionization process, which play an important " ion source " term on RHS of (5.12) and (5.13) , and hence ion energy may be modulated.

5.4 IEDFs in ICP

Both experimental data in chapter 3 and theoretical simulation results in chapter 4 indicate that the RF vector potential or the induction field can be written as follows in the centre plasma region,

$$E \propto r \tag{5.14}$$

Let us assume that the effective electron collision frequency and the ionization rate in an argon glow discharge plasma can be in the following form [72],

$$\nu_{iz} \propto f(E/p) \propto c_1E^2 + c_2E + c_3 \tag{5.15}$$

where f is function of gas type and other boundaries, p is the given neutral pressure, and $c_{1,2,3}$ are constants, which depends on the type of gas. From the discussions in the previous section, a time averaged electron radial drift exists in the ICP. This in turn requires that electron or ion source appears in the volume of discharge. This is achieved

by inductive ionization process near the glass wall, due to fact that most of the input RF power is dissipated there, as described in chapter 4.

Based on expressions (5.14) and (5.15), assuming an ionization rate profile at z=0 plane is the following form,

$$\nu_{iz} = \frac{\nu_e}{E_0}\left(E - \frac{E^2}{E_0}\right) \tag{5.16}$$

Here E_0 is the amplitude of induction field on the glass wall, and the maximum ionization rate has been assumed associated with half of the effective electron collision frequency. Owing to this induction ionization, the IVDFs or IEDFs will differ from that reported by [55, 65] in a capacitively coupled RF plasma. Apart from the main group of ions which are born in the plasma presheath region, there are also ions born in plasma sheath region which travel into retarding energy analyser, with relatively low energy as shown in figure 3.15-3.18. To derive the exact expression of IEDFs in ICP, one has to begin with solving another basic plasma equation for ion velocity distribution function F_i, in equation (5.17), which is similar to equation (1.6) in this thesis.

$$\frac{\partial}{\partial t}F_i + \underline{v}\bullet\nabla F_i + \frac{\underline{F}}{m_i}\bullet\frac{\partial}{\partial \underline{v}}F_i = \nu_{iz} f \tag{5.17}$$

where F_i is the number of ions in the phase space of velocity v, position r, and time t. f is the electron velocity distribution function mentioned in chapter 1. F is the force acting on the ion, which is equal to $e(\underline{E} + \underline{v}\times\underline{B})$, the first term on LHS is the time rate of change of F_i, while the second one stands for the change of F_i due to particles motion in space r,

the third one represents external force influence on the change of F_i, and the RHS stands for time rate of change of F_i due to ionization process. The study of equation (5.17) plus the basic equations (1.1-1.5) will pave a way to careful control and modification of the IVDFs or the IEDFs for a high density, low pressure inductively coupled plasma in the application of an advanced surface processing industry.

5.5 The radial plasma density distribution

It is well known that the ion density is equal to the electron density in the quasi-neutral region. This is one of fundamental characteristics of plasma, i.e., the plasma quasi-neutrality [73]. Given the electron density expression in equation (5.6), the time averaged plasma density can be calculated as follows,

$$n = n_0 \left\langle exp\left\{ \frac{e\phi - \frac{1}{2} m_e V_{er}^{\ 2} - \frac{e^2}{2m_e} A_\theta^{\ 2}}{kT_e} \right\} \right\rangle \tag{5.18}$$

where the brackets denote the time average process. The RF component of electrostatic potential ϕ can be shown to be negligible in ICP studied in this study as compared to electron drift energy. The DC component of electrostatic potential can be calculated by integrating of the time averaged radial electric field shown in figure 4.9. Using equation (5.5), (5.18) can be transformed into (5.19),

$$n = n_0 \left\langle exp\left\{ -\frac{\frac{e}{2m_e} A_\theta^{\,2} \left[1 + \left(\frac{V_{er}}{V_{e\theta}} \right)^2 - \frac{2m_e \phi}{eA_\theta^{\,2}} \right]}{kT_e/e} \right\} \right\rangle \tag{5.19}$$

Assuming relation (5.20) in the region near the glass wall,

$$1 >> \left(\frac{V_{er}}{V_{e\theta}} \right)^2, \left| \frac{2m_e \phi}{eA_\theta^{\,2}} \right| \tag{5.20}$$

we have,

$$n = n_0 \left\langle exp\left\{ -\frac{\frac{e}{2m_e} A_\theta^{\,2}}{kT_e/e} \right\} \right\rangle \tag{5.21}$$

Using expression (4.14) for plasma vector potential, and (5.5) for the electron poloidal drift velocity, the normalized plasma density can be calculated as follows,

$$\frac{n}{n_0} = \left\langle exp\left\{ -\frac{e}{2m_e} \frac{A_0^{\,2} cos^2(\omega t + \Phi_A)}{kT_e/e} \right\} \right\rangle$$

$$= \left\langle exp\left\{ -\frac{e}{4m_e} A_0^{\,2} \left[\frac{1 + cos(2\omega t + 2\Phi_A)}{kT_e/e} \right] \right\} \right\rangle$$

$$= exp\left[-\frac{e^2}{4m_e} \frac{A_0^{\,2}}{kT_e} \right] \left\langle exp\left\{ -\frac{e^2}{4m_e} \frac{A_0^{\,2}}{kT_e} cos(2\omega t + 2\Phi_A) \right\} \right\rangle$$

$$= I_0\left(\frac{e^2}{4m_e} \frac{A_0^{\,2}}{kT_e} \right) exp\left[-\frac{e^2}{4m_e} \frac{A_0^{\,2}}{kT_e} \right] \tag{5.22}$$

which can be simplified to,

$$\frac{n}{n_0} = I_0\left(\frac{\frac{1}{2}m_e V_d^2}{2kT_e}\right)exp\left[-\frac{\frac{1}{2}m_e V_d^2}{2kT_e}\right] \tag{5.23}$$

where I_0 is the zeroth-order modified Bessel function of the first kind as already mentioned in equation (2.17), and the amplitude of vector potential A_0 is a real function of position (r, z), and V_d represents the amplitude of the electron poloidal drift velocity. In deriving (5.23), $\nu_e << \omega$ is used.

As it can be seen clearly, the derived equation (5.23) expresses plasma density distribution in terms of electron temperature and electron drift motion for the first time. It can be used as an input plasma density profile, to search for a self consistent EM field. In the simulation, the calculated radial plasma density profile was fed back to the ICP model in chapter 4 and the subsequent change was found negligible (less than 1%). However, it has been found that the electron effective collision frequency distribution strongly affects EM field and the electron drift motion as well. It has been reconzied that the current constant electron effective collision frequency profile has to be adjusted in the future theoretical analysis, in order to find a completely-self-consistent solution of plasma vector potential equation (4.27).

Figure 5.1 shows the plasma density distribution presented by equation (5.22) for a 100 W/10 mtorr argon ICP.

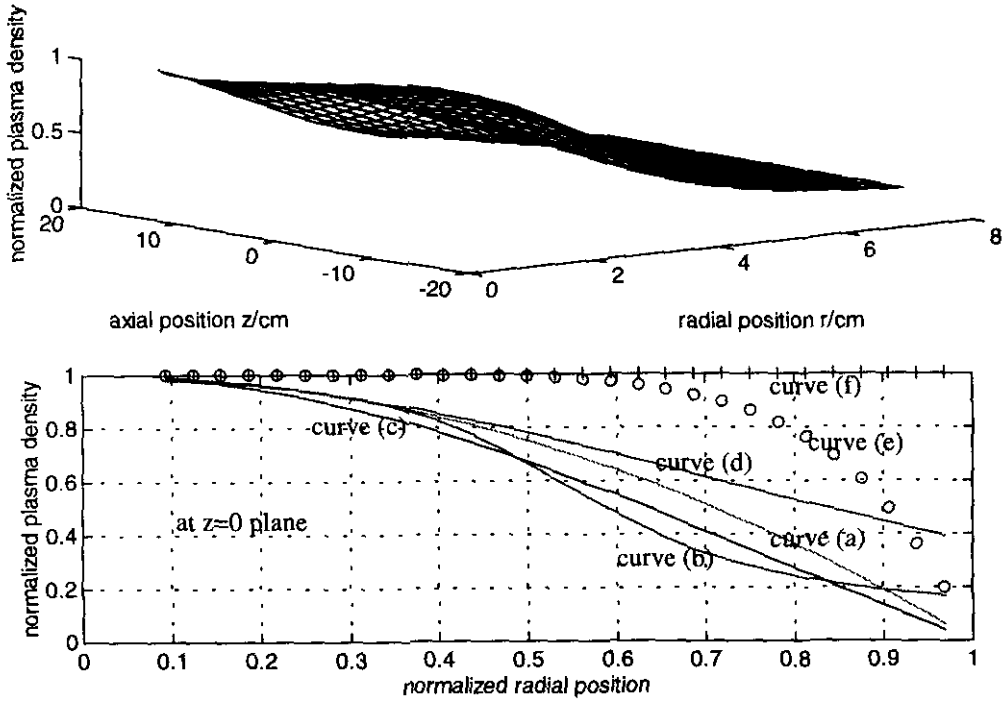

Fgiure 5.1 Normalized ICP plasma density distributions from equation (5.22), references [21, 26, 67, 68, 69] and the measured data extracted from figure 3.5a.
curve (a) is the parabolic density profile from [69],
curve (b) is the density profile from equation (5.23),
curve (c) is the Bessel function density profile from references [26, 67],
curve (d) is the Schottky density profile from [21, 68],
curve (e) is the experimental data from figure 3.5a in this study.
curve (f) is the constant density profile in reference [66].

As it can be seen from the above figure, all the theories except [66] show the similar trend in which that the plasma density decreases when r increases. Near the glass wall, prediction from equation (5.22) matches well the experimental data. This may be useful in the studying of physics of inductively coupled RF plasma presheath and sheath. Research on ion sheath formation and a study of self-consistent charge carrier motion in Oxford Research Unit is under the way.

5.6 Conclusions

This PhD thesis is about a theoretical analysis and experimental study of the physics of low pressure (5-50 mtorr), low electron temperature (1-10 eV), high density ($10^{17} - 10^{18} m^{-3}$) inductively coupled plasma. A symmetric, cylindrical inductively coupled discharge system has been set up. A single turn loop magnetic probe has been used to measure electromagnetic (EM) field in the discharge chamber. An Langmuir double probe has been designed to measure the plasma density and electron temperature. An emissive probe was used to measure the time averaged plasma potential, while a capacitive probe was used to measure the RF component of the plasma potential. A retarding field energy analyser has been used to measure the ion flux flowing to the glass wall on the midplane. The Hiden EQP mass/energy sensor has been used to monitor ion flux along the axial direction. A monochrometer was used to monitor Ar discharge emission lines from the chamber. A bolometric probe was designed to derive the plasma potential. An RF current-voltage probe was used to monitor the RF input power.

- Experimental results show that (1) the inductively coupled plasma is well confined inside the Faraday screen in the pressure range of 5-50 mtorr and RF power range of 10-400 W, (2) the measured electrostatic RF field (<1 V/cm) in the discharge chamber is negligible, compared with the large induction RF field, which is in the order of 15 V/cm, (3) the plasma potential " uphill " trend along radius in ICP was reported and modelled, (4) the measured magnetic field was used to derive the plasma conduction current density profile, the RF induction field distribution, according to

Maxwell's equations, (5) the measured electron temperature is about 2-3 eV at the RF input power of 100-400 W and argon pressure of 5-50 mtorr, (6) the IEDFs in radial direction and axial direction were observed in the experiments.

- A two-dimensional electromagnetic, finite-element analysis model has been set up to simulate the operation of the inductively coupled plasma using the external coil configuration used in the experimental work. Given input RF power, the measured plasma density profile, Maxwell's equations and magnetrohydrodynamical (MHD) fluid equations are used to calculate the self-consistent plasma vector potential, the RF induction field, the magnetic field, the conduction current density and the time averaged electrostatic electric field. A number of predictions are presented and compared with experiments. Good agreement between the theory and experiment has been demonstrated successfully.

- Electron, ion drift motions, and the ICP plasma density distribution are modelled, compared with experimental data. It has been concluded that the 3-dimetional studying of electron and ion motion in the inductive RF field and the IEDFs in ICP is needed to further understanding of physics of ICP sheath, to pave a way to careful control and modification of IVDFs or IEDFs for a high density, low pressure inductively coupled plasma in the application of an advanced surface processing industry.

Appendix 1 Time average electron current collected by a Langmuir probe tip

(1) The instantaneous electron current collected by Langmuir probe tip is given in equation (2.20), as follows,

$$I_{e1}(t) = n_0 eS\left(\frac{kT_e}{2\pi m_e}\right)^{1/2} exp\left(\frac{e}{kT_e}(V_1 + V_{RF1}\cos(\omega t))\right) \tag{A1.1}$$

(2) A generating function of Bessel function is given in reference [40],

$$exp\left[x\frac{y - y^{-1}}{2}\right] = \sum_{n=-\infty}^{\infty} J_n(x)y^n \tag{A1.2}$$

Here J_n is called the n-th order Bessel function of the first kind, which satisfy

$$J_n(-x) = (-1)^n J_n(x) \tag{A1.3}$$

(3) The n-th order modified Bessel function of first kind is defined by

$$I_n(x) = j^{-n} J_n(jx) \tag{A1.4}$$

Putting $y = exp\left[j\left(90^0 - \omega t\right)\right]$ into (A1.2), leads to,

$$exp\left[jx\cos(\omega t)\right] = \sum_{n=-\infty}^{\infty} J_n(x)e^{jn\left(90^0 - \omega t\right)} \tag{A1.5}$$

Letting $jx=z$, equation (A1.5) is transformed to,

$$exp[z\cos(\omega t)] = \sum_{n=-\infty}^{\infty} J_n(-jz)e^{jn(90^0-\omega t)} \tag{A1.6}$$

Using (A1.3) and (A1.4), it is straightforward to know that,

$$exp[z\cos(\omega t)] = \sum_{n=-\infty}^{\infty} (-1)^n I_n(z)e^{jn(90^0-\omega t)} \tag{A1.7}$$

(4) The time averaging of (A1.1) is shown to be,

$$\langle I_{e1}(t)\rangle = n_0 eS\left(\frac{kT_e}{2\pi m_e}\right)^{1/2}\left\langle exp\left(\frac{e}{kT_e}(V_1 + V_{RF1}\cos(\omega t))\right)\right\rangle$$

$$= n_0 eS\left(\frac{kT_e}{2\pi m_e}\right)^{1/2} exp\left(\frac{e}{kT_e}V_1\right)\left\langle exp\left(\frac{e}{kT_e}V_{RF1}\cos(\omega t)\right)\right\rangle$$

$$= n_0 eS\left(\frac{kT_e}{2\pi m_e}\right)^{1/2} exp\left(\frac{e}{kT_e}V_1\right)\left\langle \sum_{n=-\infty}^{\infty}(-1)^n I_n\left(\frac{e}{kT_e}V_{RF1}\right)e^{jn(90^0-\omega t)}\right\rangle$$

$$= n_0 eS\left(\frac{kT_e}{2\pi m_e}\right)^{1/2} exp\left(\frac{e}{kT_e}V_1\right) I_0\left(\frac{e}{kT_e}V_{RF1}\right)$$

which is equation (2.22).

Appendix 2 Basic vector operations used in a cylindrical coordinate

Given a vector appeared in figure 3.1, we have,

(1) Divergence of $\underline{A}$

$$\nabla \bullet \underline{A} = \frac{1}{r}\frac{\partial}{\partial r}(rA_r) + \frac{1}{r}\frac{\partial}{\partial \theta}A_\theta + \frac{\partial}{\partial z}A_z$$

(2) Curl of $\underline{A}$

$$(\nabla \times A)_r = \frac{1}{r}\frac{\partial}{\partial \theta}A_z - \frac{\partial}{\partial z}A_\theta$$

$$(\nabla \times A)_\theta = \frac{\partial}{\partial z}A_r - \frac{\partial}{\partial r}A_z$$

$$(\nabla \times A)_z = \frac{1}{r}\frac{\partial}{\partial r}(rA_z) - \frac{1}{r}\frac{\partial}{\partial \theta}A_r$$

(3) If $\underline{V}$ represents a drift velocity which may be a function of time t and space position $\underline{r}$, the derivative of $\underline{V}$ equals (see reference [5]),

$$\frac{d\underline{V}}{dt} = \frac{\partial}{\partial t}\underline{V} + \left(\underline{V} \bullet \nabla\right)\underline{V}$$

hence,

$$\left(\frac{d\underline{V}}{dt}\right)_\theta = \left[\frac{\partial}{\partial t}\underline{V} + \left(\underline{V} \bullet \nabla\right)\underline{V}\right]_\theta = \frac{\partial}{\partial t}V_\theta + V_r\frac{\partial}{\partial r}V_\theta + \frac{V_\theta}{r}\frac{\partial}{\partial \theta}V_\theta + V_z\frac{\partial}{\partial z}V_\theta + \frac{V_\theta V_r}{r}$$

$$\left(\frac{d\underline{V}}{dt}\right)_r = \left[\frac{\partial}{\partial t}\underline{V} + \left(\underline{V} \bullet \nabla\right)\underline{V}\right]_r = \frac{\partial}{\partial t}V_r + V_r\frac{\partial}{\partial r}V_r + \frac{V_\theta}{r}\frac{\partial}{\partial \theta}V_r + V_z\frac{\partial}{\partial z}V_r - \frac{V_\theta^2}{r}$$

(4) Laplace operator on vector follows that the poloidal component equals to

$$\left(\nabla^2 \underline{A}\right)_\theta = \frac{\partial}{\partial r}\left[\frac{1}{r}\frac{\partial}{\partial r}\left(rA_\theta\right)\right] + \frac{1}{r^2}\frac{\partial^2}{\partial \theta^2}A_\theta + \frac{2}{r^2}\frac{\partial}{\partial \theta}A_r + \frac{\partial^2}{\partial z^2}A_\theta$$

Appendix 3 Matlab language code to find the RF field in ICP

```
clc,clear all,
echo on
% code to find the numerical solution of EM field in ICP.
%  John 23 Aug/1995
% you need load chapter4.mat (icp)  to run this bit.
% chapter4.mat    must be a standard matlab or ascii file
        % consists of RF frequency/MHz;
        % boundary conditions
        % neutral gas pressure/mtorr.
        % the default values are: f=13.56 MHz; ne=2*1.e17 m-3 ;
        % effective electron collision frequency 1.e7
        % the number of finite element mesh unit [32 32]
        % iteration itmax 20
        % the final cycle calculation tolarence 0.01
        % measured electron density profile in the coil volume
        % press any key to continue.
echo off
pause
```

```
u0=4*pi*1.e-7;      e0=8.85*1.e-12;      c=3.e8;omeka=2*pi*13.56*1.e6;me=9.1*1.e-31;
E=1.9*1.e-19;
 r0=8*1.e-2;z0=16*1.e-2;                    % size of rf induction coil
free=1.e1*omeka;                            % electron collision frequency
load icp.mat
M=icp(4,1);N=icp(5,1); itmax=icp(6,1); tol=icp(7,1);
Mi=icp(8,1)*1.67*1.e-27;Te=icp(9,1);
xstep=1/M; x=(0:xstep:1)';  % please note Dx refer to Dj, Dy refer to Di later.
ystep=1/N; y=(0:ystep:1);   % x==radius, y====z.
Vin=zeros(size(x*y));
[m,n]=size(Vin);
cx=(m+1)/2; cy=(n+1)/2;  % the central position of Vin
for p=1:m, Vin(p,n)=1; end
for q=1:n, Vin(1,q)=(q-1)/(n-1);
        Vin(m,q)=(q-1)/(n-1);end
% those E0 at the boundary.
save bound.mat Vin
ne=zeros(size(Vin));
load ne.mat
ome=omeka*ones(size(ne)); fre=zeros(size(ne));
for p=1:m,
  for q=1:n,
```

```
    fre(p,q)=free*(1+0*y(1,q).^2);
 end
end
sigma=ne*E.^2/me./(fre+i*ome);
K=i*omeka*(u0*sigma+i*omeka*u0*e0*ones(size(ne)));  % matrix here !!!
h=1/2;  hx=h/xstep; hy=h/ystep;  % nine-point configuration now v0=[3,3]
x0=(0:h:1)'; y0=(0:h:1);
v0=zeros(size(x0*y0));
for i=1:3,
   for j=1:3,
    p=hx*(i-1)+1; q=hy*(j-1)+1;
    v0(1,j)=Vin(1,q); v0(3,j)=Vin(m,q);
    v0(i,1)=Vin(p,1); v0(i,3)=Vin(p,n);
    v0(2,2)=(v0(1,1)+v0(1,3)+v0(3,3)+v0(3,1)...
          +2*(v0(1,2)+v0(2,3)+v0(3,2)+v0(2,1))...
          +2*(v0(3,2)-v0(1,2)))/(4*h.^2*(1/4+K(i,j))+12);  % h=1/2
    end
end
Vin(cx,cy)=v0(2,2);
a0=Vin(cx,cy);
A=Vin;
for i=2:m-1,
```

```
 if i<cx,
   A(i,cy)=A(1,cy)+(a0-A(1,cy))/(cx-1)*(i-1);
 elseif i>cx,
   A(i,cy)=a0+(A(m,cy)-a0)/(m-cx)*(i-cx); end
 end
for j=2:n-1,
 if j<cy,
   A(cx,j)=A(cx,1)+(a0-A(cx,1))/(cy-1)*(j-1);
 elseif j>cy,
   A(cx,j)=a0+(A(cx,n)-a0)/(n-cy)*(j-cy); end
end
                % just found those on the axises.
for j=2:n-1,
  for i=2:m-1,
    if i<cx ,
      A(i,j)=A(1,j)+(A(cx,j)-A(1,j))/(cx-1)*(i-1);
    elseif i>cx,
      A(i,j)=A(cx,j)+(A(m,j)-A(cx,j))/(m-cx)*(i-cx); end
    end
  end
Vin=1.5e3*A;          % times the absolute value of boundary induction field
 g=guess(M,N);
```

```
figNumber=figure( ...
        'Name','poloidal electrical field distribution ', ...
      'NumberTitle','on', ...
        'Visible','on');
title('poloidal electric field distribution')
it=0;
v=Vin; vit=v;
R=zeros(size(v));
error=R;
while it<itmax,      % the main loop begin now
for j=2:N ,
 for i=2:M,
  R(i,j)=(2*(v(i-1,j)+v(i,j-1)+v(i+1,j)+v(i,j+1))...
        +v(i-1,j-1)+v(i-1,j+1)+v(i+1,j+1)+v(i+1,j-1)...
        +2*(r0/N)*(v(i,j+1)-v(i,j-1))/((j-1)*r0/N))/...        % h=r0/M
        (4*(r0/N).^2*((N/j*r0).^2 +K(i,j))+12)-v(i,j);
  v(i,j)=v(i,j)+g/4*R(i,j);    % this is residual for wave equation of E
 end
end
it=it+1
for i=2:M,
```

```
  mesh(X(2:n),Y,U(:,2:n))
  xlabel('radial position r/cm')
  ylabel('axial position z/cm')
  zlabel(' amplitude of induction field/(v/m)')

subplot(2,1,2)
  mesh(X(2:n),Y,phaseE(:,2:n))
  xlabel('radial position r/cm')
  ylabel('axial position z/cm')
  zlabel('phase difference picture(degree)')
save E0.mat E0
figNumber=figure( ...
        'Name','plasma vector potential distribution ', ...
      'NumberTitle','on', ...
        'Visible','on');
title('vector potetnial distribuition')
clear j,
A=E0/j./ome;
phaseA=angle(A)*180/pi; U=abs(A);
 subplot(2,1,1)
  mesh(X(2:n),Y,U(:,2:n))
  xlabel('radial position r/cm')
```

```
  ylabel('axial position z/cm')
  zlabel(' amplitude of vector potential/(sv/m)')
subplot(2,1,2)
  mesh(X(2:n),Y,phaseA(:,2:n))
  xlabel('radial position r/cm')
  ylabel('axial position z/cm')
  zlabel('phase difference picture(degree)')
save A0.mat A


figNumber=figure( ...
        'Name','drifting electron current distribution ', ...
      'NumberTitle','on', ...
        'Visible','on');
title('drifting electron current distribuition')
J=sigma.*E0;U=abs(J);phaseJ=angle(J)*180/pi;
  subplot(2,1,1)
  mesh(X(2:n),Y,U(:,2:n))
  xlabel('radial position r/cm')
  ylabel('axial position z/cm')
  zlabel('amplitude of drift current(A/m2)')


subplot(2,1,2)
```

```
  mesh(X(2:N),Y,phaseJ(:,2:N))
  xlabel('radial position r/cm')
  ylabel('axial position z/cm')
  zlabel('phaseJ/degree)')


figNumber=figure( ...
        'Name','axial B field distribution ', ...
     'NumberTitle','on', ...
        'Visible','on');
title('axial B field distribution')
Bz=zeros(size(E0));clear i;
for p=1:m,
   for q=2:N, Bz(p,q)=(i/omeka*((E0(p,q+1)-E0(p,q-1))/(2/N)+E0(p,q)/(q/N)))/r0*1.e4;
   end
end
U=abs(Bz);  phaseBz=angle(Bz)*180/pi;
  subplot(2,2,1)
  mesh(X(4:N),Y,U(:,4:N))
  xlabel('radial position r/cm')
  ylabel('axial position z/cm')
  zlabel('amplitude of Bz(gauss)')
```

```
subplot(2,2,2)
  mesh(X(4:N),Y,phaseBz(:,4:N))
  xlabel('radial position r/cm')
  ylabel(' z/cm')
  zlabel('phaseBz/degree')
subplot(2,2,3)
plot(X(4:N),U(cx,4:N),'r-')
xlabel('radial position /cm')
ylabel(' amplitude of Bz /Gausses')
axis([0 8 0 6])
grid
subplot(2,2,4)
plot(X(4:N),phaseBz(cx,4:N),'r-')
xlabel('radial position /cm')
ylabel(' phase of Bz /degrees')
axis([0 8 80 100])
grid
save Bz.mat Bz


figNumber=figure( ...
        'Name','radial electrostatic field distribution ', ...
      'NumberTitle','on', ...
```

```
        'Visible','on');
title(' <Er> distribuition')
Er=zeros(size(A));
for p=2:M,
   for q=2:N,
Er(p,q)=0.5/(q/N*r0)*E/me*abs(A(p,q))^2*...
        (1-q/N*r0*abs(Bz(p,q))./abs(A(p,q))*...
        cos(angle(A(p,q))-angle(Bz(p,q))+fre(p,q)/ome(p,q)))...
        -2/ne(p,q)*(ne(p,q+1)-ne(p,q))/(q/N*r0);
   end
end
Er=Er/1.e2;
save Er.mat Er
subplot(2,1,1)
mesh(X(4:N),Y(4:N),Er(4:N,4:N))
  xlabel('radial position r/cm')
  ylabel('axial position z/cm')
  zlabel('<Er> (V/m)')
[p5,s5]=polyfit(X,Er(:,cy),10);
save p5.mat p5; % ready to integrate Er at z=0 plane
subplot(2,1,2)
Vp=zeros(size(X));
```

```
for q=2:N,
Vp(q)=-quad('Vp',X(1)*1.e-2,X(q)*1.e-2);
end
plot(X(2:N),Vp(2:N),'r-')
xlabel('radial position r/cm')
ylabel(' plasma potential difference (V)')
title('calculated Vp profile at z=0 plane')
grid

figNumber=figure( ...
        'Name','power coupling picture ', ...
      'NumberTitle','on', ...
        'Visible','on');
title('power coupling picture')
P=J.*E0; U1=abs(P).*cos(angle(J)-angle(E0));
 subplot(2,1,1)
  mesh(X(2:n),Y,U1(:,2:n))

title('power dissipated in plasma(J*E)/(Wm-3)')

Sr=1/u0*E0.*Bz*1.e-4; U2=abs(Sr).*cos(angle(Bz)-angle(E0));
 subplot(2,1,2)
```

```
 mesh(X(2:N),Y,U2(:,2:N))

 title('time averaged power vector Sr/(Wm-2)')


end
```

==========

References:

1. J.H. Keller, M.S. Barnes and J.C. Forster

43rd Annual Gaseous Electronics conference,

Champaign-Urbana, Illinois, 16-19 Oct. 1990, Abstract NA-5.

2. Lam Research Corporation, Technical Note TN-003(1993).

3. Katsuhiro Yokota, Manabu Takada, Yoshikazu Ohno and Saichi Katayama

J. Appl.Phys. 72(3), 1188,1992

4. Peter L.G. Ventzek, Michael Grapperhaus and Mark J. Kushner

J. Vac.Sci. Technol.B 12(6),3119, 1994.

5. Michael A. Lieberman, Richard A. Gottscho

Design of high-density plasma source for materials processing,

1994 by Academic Press Inc. ISBN 0-12-533018-9

6. K.U. Riemann, J.Phys.D:Appl.Phys. 24, 493, 1991

7. H.S.W. Massey and E.H.S. Burhop, "Electronic and Ionic impact phenomena",

Oxford: Clarendon Press, 1952.

8. D.R. Bates, " Atomic and Molecular Processes",

New York and London: Academic Press, 1962.

9. S.C. Brown, Introduction to electric discharges in gases, 165, 1966

by John Wiley & Sons, Inc.

10. B. Chapman, glow discharge processes, J Wiley & Sons, 1980.

11. F. Llewellyn-Johns, Phil. Mag. 11, 163, 1931.

12. G. Babat, J. Instn.elect. Engrs 94, 27, 1947.

13. J. A. Bittencourt, Fundamentals of plasma physics, 1, Pergamon Press, 1986.

14. W.Hittorf., Wiedemanns Ann. Phys. 21, 90, 1884.

15. J.Thomson , J. of Philosophical Magazine 32, 445, 1891.

16. G. I. Babat, J.IEE, 47, 27-37, 1947.

17. A.D Stokes, Proc. IEE 112, 1583, 1965.

18. J.J. Thomson and G.P. Thomson, " Conduction of electricity through gases", by Press of Cambridge University, 1933.

19. J.S.Townsend and R.H. Donaldson, Phil. Mag., 5, 178, 1928.

20. G.D. Yarnold, Phil.Mag., 13, P. 1179, 1932.

21 J.W. Denneman, J.Phys. D23, 293, 1989.

22. A.J. Hatch and H.B. Williams, GEC conference, 1951, New York.

23. A. H. Von Engel and G. Francis, Proc. R.Soc., B63, 823, 1950.

24 D.K. Coultas and J.H. Keller, European Patent Application 0379828 A2, 1989.

25. C.K. Birdsall, IEEE Transaction on plasma science 19(2), 65, 1991.

26. G.G. Lister and M. Cox, Plasma Source Sci. Technol. 1, 67, 1991.

27. R.B. Piejak and V.A. Godyak, Plasma Source Sci Technol 1, 179,1992.

28. J. Hopwood et al, J. Vac. Technol.A 11(1), 147, 1992.

29. M.M. Turner, Phys.Review Letter 71(12), 1884, 1992.

30. J.H. Keller, 42 GEC Conference, Bull.Am. Phys. Soc.Series 2, 34, 1989.

31. D.K. Coultas and J.H. Keller, US Patent 5304279, 1994.

32a. J.H. Keller, Plasma Source Sci Technol.5, 166, 1996.

32b. V.J.Law, N.StJ.Braithwaite, J.Vac.Sci.& Tech. B, Vol.12, No.6, pp.3337-3341, 1994.

33. M.A. Herlin and S.C Brown, Phys. Rev. 74, 291, 1948.

34. A.D. MacDonald Microwave Breakdown in Gases (New York: Wiley), 1966.

35. S.F. Durrant, Fresentius Journal of Analytical Chemistry, 347(10), 389-392, 1993.

36. V.Comello, R&D magazine, 35(5), 79-80, 1993

37. A.P. Paranjpe, J. of Vac. Sci. & Tech. A: Vac. Surface and films, 12(4), 1221-1228,1994.

38. H.M. Wu, et al, IEEE Tran. on Plasma Science, 25(4), 776-785, 1997.

39. R.P.Feynman, et al, lectures on physics, 2, Addison-Wesley Publishing Company, 1964.

40. A.C. Bajpai, L.R. Mustoe, and D. Walker, "Advanced engineering mathematics", John Wiley & Sons , 1978.

41. S. Yang , F.A. Haas and N StJ Braithwaite, 22ed IOP Conference, Oxford, UK, 1993.

42. K. Chandrakar, J. Phys. D, 11, 1809, 1978.

43. J. Amorim, H.S. Maciel and J.P. Sudano, J.Vac.Sci.Technol.B 9(2), 362, 1991.

44. R. E. Collin, Foundations for microwave engineering , 91, 1992 by McGraw-Hill, Inc.

45. N. StJ Braithwaite, Plasma souce Sci. & Tech., 6(2), 133-139, 1997.

46. V.A. Godyak and N.Sternberg, Phys.Rev. A. 42, 2299, 1990.

47. C.M.O. Mahony, N.Braithwaite, internal report of ORU, 1994.

48. Mott-Smith, H.M. and I. Langmuir, Phys.Rev. 28, 727, 1926.

49. J. D. Swift, M. J. R. Schwar, electrical probes for plasma diagnostics, Iliffe Books Ltd, 1970

50. F.F. Chen, Introduction to plasma Diagnostic Techniques, R.H.Huddlestone and S.L.leonard, eds. academic, New York, 1965.

51. N. St. J. Braithwaite, N.M.P. Benjamin and J.E.Allen, J.Phys.E: Sci.Instrum. 20, 1046-1049, 1987

52. N.Hershkowitz, in Plasma Diagnostics, Vol.1, O.Auciello and D.L.Flamm, eds., Acdamic, New York, 1989.

53. V.A.Godyak, R.B.Piejak, and B.M.Alexandrovich, Plasma Source Sci.Technol.1,36, 1992.

54. PlasmaProbe operation manual, AEA Technology/UK, 1990.

55. S.G.Ingram, N.St.J.Braithwaite, J.Appl.Phys. D, Vol.21, No.10, 1496-1503, 1988

56. A.A. Goruppa, N.SJ. Braithwaite, and D.M. Grant T, Diamond and related materials, 3(10), 1223-1226.

57. R. Winkler, et al, Plasma Chemistry and Plasma Processing, 1987, Vol.7, No.3, pp.245-265

58. F.F. Chen, et al, Plasma Sources Science & Technology, 1996, Vol.5, No.2, pp.173-180

59. J.W. Coburn, E. Kay, J.Appl.Phys.43, 4965

60. M. Alikettani and Max F. Hoyaux, " plasma engineering", chapter 6, London Butterworths & Co. Ltd, 1973.

61. N.ST.J. Braithwaite, F.A. Haas, J. Physics D-Applied Physics, 27(9), 1992-1993, 1994.

62. F.A. Haas, S. Yang, N StJ Braithwaite, 46th GEC conference, Montreal, Canada,1994.

63. J.A. Meyer, R.Mau, and A.E.Wendt, J.Appl.phys. 79, 1298, 1996.

64. F.A. Hass, N StJ Braithwaite, J. Appl. Phys., 82(7), 3612-3614,1997.

65. S.G.Ingram, N.St.J.Braithwaite, J.Appl.Phys. D, Vol.68, No.11, pp.5519-5527, 1990.

66. J. Thomson, Phil.Mag. 7, 1127, 1927.

67. H. U. Eckert, J. Appl.Phys. 33, 2780, 1961.

68. W. Schottky, Phys.Z. 25, 635, 1924.

69. B.B. Henniksen, D.R. Keefer and M.H. Clarkson, J.Appl. Phys. 42, 5460, 1971.

70. T.J. Sommerer and M.J.Kushner, J.Appl.Phys. 71, 1654, 1992.

71. V.Vahedi, M.A.Liebermann ,et al, J.Appl.Phys., 78(3), 1446, 1995.

72. Y.P. Raizer, Gas Discharge Physics (Moscow Springer-Verlag), 1991.

73. D. Bohm, Characteristics Elec., 1949 Chapter 3, 1949.

74. J.E. Allen, P Phys. SOC, B, 4, 187, 1970.

75. J.G. Andrews, Phys. Fluids, 15, 2271, 1972.

76. L.M. Wickens, Phys. Lett. A, 88, 147, 1982.

77. N.St.J.Braithwaite, J.E. Allen, Phys. Fluids, 27(1), 203-205, 1984.

78. MatlabUsers Manual for Windows, Mathworks, Inc, 1994.

79. R. Wait, Finite element analysis and applications, 1985 by J. Wiley.

80. U.Kortshagen, L.D.Tsendin, Applied Physics letters, Vol.65, N0.11,

pp.1355-1357, 1994.

81. L.J. Mahoney, et al, J.Appl.Phy., Vol. 76, No.4, pp.2041-2047, 1994.

82. C.Lai., et al., J.Vac.Sci. & Tech. A, Vol. 13, No.4, pp.2086-2092, 1994

83. Sturrock, " Introduction to plasma physics ", Cambridge University Press, 1994

========== <END> ==========